Alma Mater Studiorum - Università di Bologna

DOTTORATO DI RICERCA IN

NANOSCIENZE PER LA MEDICINA E PER L'AMBIENTE

Ciclo 34

Settore Concorsuale: 03/B1 - FONDAMENTI DELLE SCIENZE CHIMICHE E SISTEMI INORGANICI

Settore Scientifico Disciplinare: CHIM/03 - CHIMICA GENERALE E INORGANICA

BIOMATERIALS FOR OSTEOARTICULAR APPLICATIONS: ROLE OF FUNCTIONALIZATION

Presentata da: Katia Rubini

Coordinatore Dottorato

Dario Braga

Supervisore

Adriana Bigi

Co-supervisore

Elisa Boanini

Dario Braga

Esame finale anno 2022

Summary

This PhD thesis was focused on the development and characterization of functionalized materials with potential applications for the substitution/repair of damaged tissues. The demand of new biomaterials is indeed continuously increasing also because of the increased life expectancy in developed countries and the consequent dramatic rise in the number of age related disorders affecting mainly, but not only, the muscolo-skeletal system. To this aim, the materials utilized as substrates in this thesis were calcium orthophosphates, namely hydroxyapatite, β-tricalcium phosphate, monetite and brushite, and gelatin films. This choice was based on a biomimetic strategy: the inorganic component of the hard tissues of vertebrates is a basic calcium phosphate similar to synthetic hydroxyapatite, and gelatin is a degradation product of the main proteic component of the human body, collagen.

Functionalization of calcium phosphates was performed through ionic substitution, adsorption of metallic nanoparticles, organic molecules, amino and polyamino acids.

The results indicated that the possibility of ionic substitution depends both on the type of calcium phosphate and of the foreign ion. Strontium was found to substitute for calcium in the whole range of composition in the structure of monetite, as previously verified for hydroxyapatite, up to about 80 at% in β-tricalcium phosphate, whereas the replacement is limited to about 38 at% in the case of brushite. The introduction of the big strontium ion cause an enlargement of the unit cell of all the examined phosphates, as well as variations in their morphology. The maximum incorporation of zinc into β-tricalcium phosphate is much less than that of strontium: it amounts just to about 10 at%, and it causes a reduction of the unit cell, in agreement with the reduced dimensions of zinc in comparison to calcium, and a general structural disorder. Moreover, zinc exhibits a clear preference for the octahedrical Ca(5) site, whereas strontium prefers the wider Ca(4) site.

Hydroxyapatite and strontium-substituted hydroxyapatite were utilized as supports for Pt nanoparticles and β-lactams, respectively. It was found thea the amount of adsorbed β-lactam can reach values also greater than 20 wt% and depends both on the type of molecule and on the polarity of the loading solution. Adsorption of Pt nanoparticle was promoted by hydroxyapatite functionalization with PEI and provided materials with

very good anti-oxidant properties. Both Pt nanoparticles and β-lactams displayed a controlled release in solution over time.

The results of the study of the interaction of aspartic acid and polyaspartic acid with brushite revealed that both molecules inhibit the crystallization of the calcium phosphate when present in the synthesis medium. However, the interaction of polyaspartic acid with the (0k0) faces of brushite causes its adsorption up to about 2.3 wt%, whereas aspartic acid is not adsorbed at all. Moreover, both molecules inhibit brushite hydrolysis in physiological solution although the delay of reaction provoked by polyaspartic acid is greater.

Finally the properties of gelatin films were modified through functionalization with two polyphenols, namely quercetin and curcumin, which are known for their good anti-inflammatory, anti-oxidant and anti-cancer activities.

The results obtained on the functionalized materials developed during this PhD thesis indicate that the functionalizing agents maintain their desirable biological properties also when coupled to the calcium phosphates, thus providing new materials with enhanced and widened beneficial characteristics.

Chapter 1
INTRODUCTION

1. Biomaterials

Biomaterials are man-made materials used for human tissues substitution and/or repair, that intend to avoid the problems due to the use of natural materials in practical applications. Natural materials comprise

- Autografts, which involves harvesting a tissue from one location in the patient's body and transplanting it into another part of the same patient. Using autologous grafts, when available, typically produces the best clinical results.
- Allografts, which involves harvesting and processing bone from a cadaver then transplanting it to the patient. Allogenic implants are acellular and are less successful than autografts for reasons attributed to immunogenicity and the absence of viable cells.
- Xenogenic materials, tissues from animals that are available in unlimited quantities but it cannot be implanted without thorough pre-treatment since it would cause strong and detrimental immune reactions.

A first and broad definition of the term *biomaterial* is "*a nonviable material used in a medical device, intended to interact with biological systems*" [Williams, 2009]. The first materials considered as biomaterials and used in the biomedical field were often simple metals and/or alloys, chosen for their peculiar mechanical properties and resistance. Because of the problems linked to corrosion and, in some case, to their toxicity, during the 20th century they were replaced by new materials, endowed with very peculiar and tunable characteristics. Indeed, the last century was characterized by the extraordinary development of the plastic industry and by the increased interest in the ceramic science. The major part of biomaterials and medical devices is composed of materials that can be divided into three main classes: metals, bioceramics and polymers.

Nowadays, biomaterials are utilized in different biomedical fields, which include cardiovascular, orthopaedic, wound healing, tissue engineering and ophthalmology applications [Festas, 2020]. Biocompatibility of all these materials is a compulsory property: the biocompatibility of a long-term implantable medical device refers to the ability of the device to perform its intended function, with the desired degree of

incorporation in the host, without eliciting any undesirable local or systemic effects in that host.

Therefore, the updated definition of a biomaterial has become the following: "*material intended to supply or to replace all or a part of a deficient organ*" [Lam, 2012]. This last definition includes the biological environment (living system, biological fluids, proteins, cell and tissues) as well as the biological constraints and functions. This concept highlights the important contribution of the interactions between the material and the environment, and the capacity of the device to exist in contact with tissues and, in general, with the living system, without causing an adverse host response.

The practice of these materials has increased during the last few years especially due to the aging population and the desire to maintain health and well-being [Jain, 2011]. Their evolution tends towards an improvement of their characteristics, making them more versatile and innovative. The present "third generation" of biomaterials has therefore the aim of proposing better solutions to replace deficient organs and prevent the hostile host responses encountered when materials are implanted for a long term.

Biodegradability could be a highly desired property for most biomedical applications *in vivo*, such as transient implants, drug delivery carriers, and tissue engineering scaffolds. Biodegradable biomaterials, for example, intend to serve as temporary supports for cell attachment, growth and differentiation in order to lead the tissue to its regeneration, replacing a defect of a soft or hard tissue during the progressive degradation of the biomaterial itself [Langer, 2004]. The opposite concept is represented by biotolerant or bioinert materials that are biocompatible materials, as well, but can't induce any interfacial biological bond between implants and host natural tissue and often induce the formation of a thin capsule of connective tissue that do not adhere to the implant surface.

A new frontier is the surface modification of materials used as biomaterials in order to improve their biological properties, for example promoting or not the adsorption of proteins, inspiring cells response or a surrounding tissues integration. This could be achieved through binding a molecule of biological interest to the surface of the polymeric, metallic or ceramic material to induce a better hydrophobic/hydrophilic balance, specificity, or bioactivity [Jain, 2011]. The aim of regenerative medicine is persuading the body to heal itself by providing appropriate signals.

In this thesis the focus is on the development of new materials for both hard and soft tissue repair/substitution, in particular the study has regarded the functionalization of calcium phosphates, as ceramic materials, and of gelatin, as polymeric material.

2. Calcium Phosphates

Apatites and other related calcium phosphates are regarded with interest by biologists and medical doctors as well as by materials chemists. In fact, calcium phosphates form the mineral component of bones and teeth and occur in pathological calcification in human body. In particular, bone is a dynamic, highly vascularized tissue that is formed from a composite of 70% mineral (mostly nanoscale hydroxyapatite crystals) and 30% organics (including collagen, glycoproteins, proteoglycans, and sialoproteins) by dry weight [Salgado, 2004]. The past half century has seen explosive growth in the use of medical implants for bone repair and/or substitution. Orthopaedic, oral and maxillofacial surgeons are only few examples of medical specialists treating millions of patients each year by implanting devices.

In this context, calcium phosphates are the best candidates to develop new materials thanks to their properties of biocompatibility and bioactivity. As bioactive materials, they are able to form a direct chemical bond with the biological tissue and a strong biomaterial/bone interface. Furthermore, calcium phosphates-based materials have been demonstrated to be osteoconductive and osteoinductive [LeGeros, 2008].

Osteoconductivity and osteoinductivity are desirable properties, being respectively the ability of a material to facilitate cell attachment, proliferation, and migration through the scaffold, as well as nutrient-waste exchange and new vessel penetration; and the ability to induce the differentiation of osteoprogenitor cells such as mesenchymal stem cells into osteoblasts, culminating in bone formation.

From the chemical point of view, the interest as biomaterials is focused on the broad family of calcium orthophosphates that are salts of the tribasic phosphoric acid, H_3PO_4, and thus can form compounds that contain $H_2PO_4^-$, HPO_4^{2-}, PO_4^{3-} ions. Those with $H_2PO_4^-$ ions only form under rather acidic conditions, therefore are not normally found in biological systems. However, both HPO_4^{2-} and PO_4^{3-} ions occur in the mineral of bones and teeth and in various pathological calcifications. Some calcium phosphates are hydrated, and those that belong to the basic apatitic calcium phosphate family contain OH^- ions (Table 1.1). Pyrophosphates ($P_2O_7^{4-}$) and polyphosphates [$(PO_3)_{nn}^-$], which

contain P-O-P bonds, are of less biological importance than the orthophosphates, although calcium pyrophosphates occur in some pathological calcifications [Elliott, 1994].

Table 1.1 – Calcium orthophosphates

Abbreviation	*Compound*	*Formula*	*Ca/P*	*- log (K_{sp}) 37°C*
HA	Hydroxyapatite	$Ca_5 (PO_4)_3 (OH)$	1.67	58.60
MCPM	Monocalcium phosphate monohydrate	$Ca (H_2PO_4)_2 \cdot H_2O$	0.5	---
MCPA	Monocalcium phosphate anhydrous	$Ca (H_2PO_4)_2$	0.5	---
OCP	Octacalcium phosphate	$Ca_8 H_2 (PO_4)_6 \cdot 5 H_2O$	1.33	95.90
DCPD	Dicalcium phosphate dihydrate	$CaHPO_4 \cdot 2 H_2O$	1	6.63
DCPA	Dicalcium phosphate anhydrous	$CaHPO_4$	1	7.02
TTCP	Tetracalcium phosphate	$Ca_4(PO_4)_2 O$	2	42.40
α - TCP	α – Tricalcium phosphate	α - $Ca_3(PO_4)_2$	1.5	25.50
β - TCP	β – Tricalcium phosphate	β - $Ca_3(PO_4)_2$	1.5	29.50
ACP	Amorphous calcium phosphate (gives an X-ray diffraction pattern without discernible peaks from lattice periodicities)			

Among orthophosphates, the increase of Ca/P molar ratio is associated with an increase in the basicity of these salts [Brown, 1986]. Hydroxyapatite (HA) is the most thermodynamically stable and less soluble phase and it is preferentially formed under neutral or basic conditions. In more acidic solutions, phases such as brushite (DCPD) and octacalcium phosphate (OCP) are often encountered.

In biological tissues, DCPD and OCP are usually detected only during pathological calcifications, where the pH is often relatively low. In normal in vivo calcifications, these phases have not been found, suggesting the involvement of other precursors or the formation of an initial amorphous calcium phosphate phase (ACP), followed by transformation to apatite [Lijun, 2008]. Indeed, the kinetic factors are fundamental for determining which crystalline phases will be formed, with respect to the others in a supersaturated solution. In fact, HA formation evolves through the formation of intermediate products, which are thermodynamically metastable but kinetically favoured.

The solubility isotherms of different calcium phosphate salts in equilibrium with their saturated solution is shown in Figure 1.1 which represents the logarithm of calcium concentration (log[Ca]) of the saturated solution versus pH.

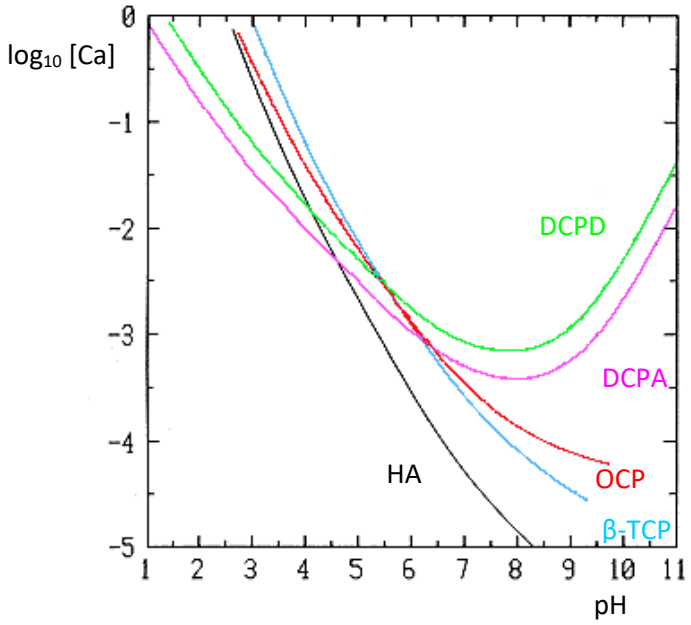

Figure 1.1 - Solubility isotherms of main calcium phosphates phases in the system $H_3PO_4 – Ca(OH)_2 – H_2O$ at 37 °C [Johnsson, 1992].

A common characteristic of the isotherms is that they have a negative slope in the neutral and acid regions of the solubility diagrams. This means that these compounds are more soluble as the pH decreases. Thus, the isotherm slope is somehow a measure of the salt basicity, since the solubility of a basic salt is greater than that of an acid salt for an equal decrease in pH. According to this, DCPD and DCPA are more acid salts than OCP, α-TCP, β-TCP and HA. HA is the least soluble salt for pH values higher than ~ 4.5, while for pH values lower than this DCPA is the least soluble salt.

The influence of pH on the formation of calcium phosphates is linked to the properties of phosphate containing solutions. Due to the triprotic equilibria in these systems, variations in pH alter the relative concentrations of the four protonated forms of phosphoric acid and thus both the chemical composition and the amount of the calcium phosphate that forms by direct precipitation. This complex equilibrium makes the control and prediction of calcium phosphate precipitation very difficult [Lynn, 2005)]. The reactivity and relative stability of different salts are influenced by many factors,

such as temperature, ionic strength, Ca/P molar ratio in solution or the presence of impurities.

In general, the stability or instability of a calcium phosphate in solution may be correlated with its mechanism of formation. Some calcium phosphates can be sinthesized by direct precipitation from a supersaturated solution, or after phase conversion in solution (hydrolysis reaction); while others can be prepared only by solid state reactions at high temperatures.

2.1 Hydroxyapatite

The name of apatite was coined from the Greek απαταω (to deceive) because it was frequently confused with other minerals such as aquamarine, olivine, amethyst, fluorite, etc. Apatites have the formula $Ca_5(PO_4)_3X$, where X can be an OH^- ion (hydroxyapatite), a F^- ion (fluorapatite) or a Cl^- ion (chlorapatite), for example. The apatite structure is very tolerant for ionic substitutions, so Ca^{2+} ions can be partly or completely replaced by Ba^{2+}, Sr^{2+} or Pb^{2+} ions and $PO4^{3-}$ by AsO_4^{3-} ions. Thus, there are lead minerals with apatitic structure such as $Pb_5(PO_4)_3Cl$ (pyromorphite), $Pb_5(VO_4)_3Cl$ (vanadinite) and $Pb_5(AsO_4)_3Cl$ (mimetite). Coupled substitutions frequently occur in apatites, where one ion is replaced by another of the same sign, but different charge, and neutrality is maintained by substitutions of ions with dissimilar charge or vacancies elsewhere [Elliott, 1994].

Carbonate apatites have been the subject of many studies. These include the minerals francolite, dahllite and the rock-phosphates, and the biological apatites. Nonstoichiometry, with vacant lattice sites, occurs in biological apatites and frequently in synthetic ones, which considerably complicates their crystal chemistry.

Pure HA crystallizes in the monoclinic space group $P2_1/b$. However, the presence of impurities stabilizes the hexagonal structure at room temperature. The basic apatite hexagonal structure, space group $P6_3/m$, exhibits approximate lattice parameters a = 9.4 Å and c = 6.9 Å with two formula units per unit cell, which is the reason why a double formula is often used [$Ca_{10}(PO_4)_6X_2$]. These values often depend on the mode of preparation because of the frequent nonstoichiometry.

The $P6_3/m$ space group has three kinds of vertical simmetry elements: (1) six-fold screw axes passing through the corners of the unit cells marked (these simmetry elements are equivalent to a three-fold rotation axis with a superimposed two-fold screw axis); (2)

three-fold rotation axes passing through ⅔, ⅓, 0 and ⅓, ⅔, 0; and (3) two-fold screw axes passing through the mid points of the cell edges and its center. There are also mirror planes perpendicular to the $_c$-axis at z = ¼ and ¾, and numerous centers of simmetry.

The structure can be roughly described as an assembly of tetrahedral phosphate PO_4^{3-}, among which are placed the calcium ions in two independent crystallographic sites, crossed by parallel channels filled by OH^- ions and oriented along the crystallographic *c*-axis (Figure 1.2) [Boanini, 2010].

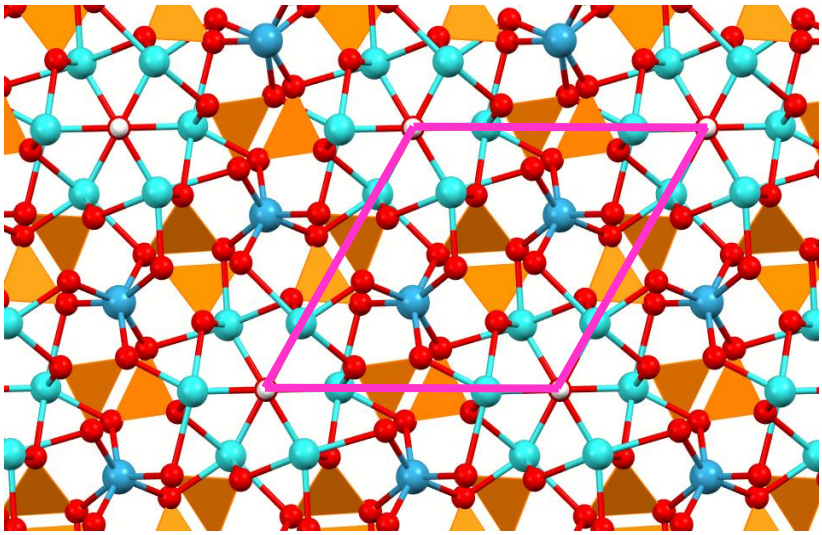

Figure 1.2 - A view of the HA structure along the *c*-axis. Ca(1) atoms are represented in dark blue; Ca(2) atoms are light blue and lye in the staggered triangles at different height with respect to the *c*-axis; phosphate groups are represented with orange tetrahedral. Pink lines draw HA unit cell.

There are columns of Ca^{2+} ions spaced by one-half of the c-axis parameter along the three-fold axes at ⅔, ⅓, 0 and ⅓, ⅔, 0 which account for two-fifths of the Ca^{2+} ions in the structure. These ions are given the designation Ca(1) or Ca (I) or Ca_1. The site they occupy is often called *columnar site* (Figure 1.3). Each of these Ca^{2+} ions is connected to its neighbouring Ca^{2+} ions above and below by three shared oxygen atoms that lie in the mirror plane (Figure 1.3). On one side, there are three O(1) atoms at 2.397(1) Å, and on the other side three O(2) atoms at 2.453 (1) Å . Each Ca(1) ion is also coordinated by three further oxygen atoms, O(3), at a greater distance (2.801 (1) Å) at approximately the same *z* parameter as the Ca^{2+} ion. Thus the columnar Ca^{2+} ions are nine-fold coordinated by oxygen atoms. These columns of Ca^{2+} ions and their

coordinated oxygen atoms are linked together by PO_4 tetrahedra in which three oxygen atoms come from one column, and the fourth from the adjacent column. The result is a three-dimensional network of PO_4 tetrahedra with enmershed columnar Ca^{2+} ions and with channels passing through it.

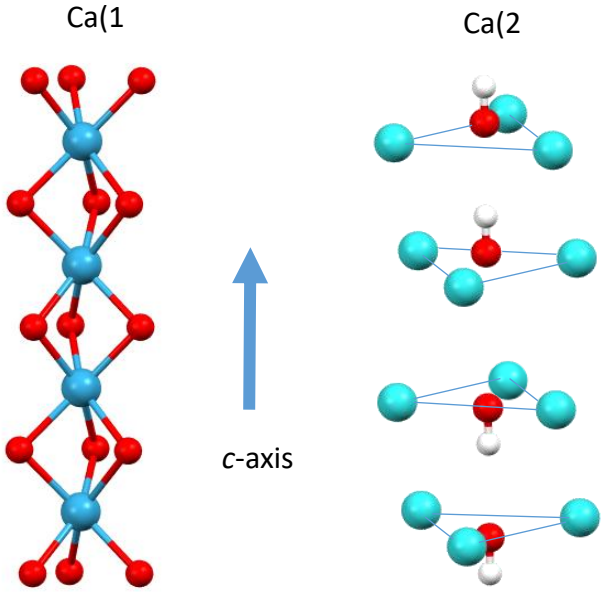

Figure 1.3 – Oxygen coordination of columnar Ca(1) ions in hydroxyapatite structure; and arrangement of the Ca(2) atoms forming the vertical channel around the *c*-axis by staggered triangles that host OH^- groups.

The axes of these channels coincide with the six-fold screw axes and the corners of the unit cells, and one forms the c-axis.

The remaining ions, OH^- and their adjacent Ca(2) ions that are required to complete the structure are located in the channels. These channels have six caves per *c*-axis repeat of the unit cell, centred on the mirror planes at z = ¼ and ¾, into which Ca(2) ions can fit. The Ca(2) ions occupy the so-called *triangular site*, where two triangles of Ca^{2+} ions are rotated by 60° from each other about the *c*-axis (Figure 1.3) and contain an OH^- ion at their centres. Thus the OH^- ions are three-fold coordinated by Ca^{2+} ions, with all four ions lying on a mirror plane.

The literature reports a variety of direct syntheses methods for HA that, although differing in terms of the detailed conditions, essentially follow two procedures. The first one consists in the stoichiometric titration of a calcium hydroxide slurry with

phosphoric acid up to neutrality [McDowell, 1977]. In the second one, the precipitation method, a solution of ammonium or sodium monohydrogen phosphate is added dropwise to a calcium solution (generally calcium nitrate or acetate) or vice versa [Bigi, 2004; Featherstone, 1983]. Both methods yield good crystalline products when carried out at high temperature (about 90°C). Lower temperature provokes an increase in the amount of amorphous material and/or decrease in crystallinity. The titration method is performed in a basic environment, whereas the precipitation method often implies addition of ammonia or sodium hydroxide to maintain a basic pH (>9) during precipitation. A further factor that influences crystallinity and crystal dimensions is the reaction time: short reaction times provide nanocrystals and/or amorphous products, whereas crystal dimensions and crystallinity increase with increasing reaction time [Boanini, 2010].

2.2 Monetite

Dicalcium phosphate anhydrous (DCPA, $CaHPO_4$) is also referred to as calcium hydrogen orthophosphate. Its mineral (monetite) was first described in 1882 in rock-phosphate deposits from the island of Moneta (from which the name derives) and Mona in the West Indies. DCPA doesn't occur in calcifications, both normal or pathological, and has only been reported in fracture callus [Lénart, 1972)].

DCPA might be expected to occur more frequently than DCPD, since DCPA is less soluble in all conditions. However, its slow rate of crystal growth relative to DCPD explains why the latter forms even if it is less stable [Young, 1982]. Once again, this is an example of the importance of kinetic factors in determining which phase is formed. It has been suggested that DCPD precipitates more readily than the less soluble anhydrous salt because the hydrated ions in solution are more readily incorporated into an hydrated crystal. Furthermore an hydrated structure has a lower surface energy at the nucleation stage, so it is favoured over anhydrous crystal nuclei.

At room temperature DCPA crystallizes in the triclinic form, space group P-1 and unit cell a = 6.910(1) Å, b = 6.627(2) Å, c = 6.998(2) Å, $\alpha = 96.34(2)°$, $\beta = 103.82(2)°$ and $\gamma = 88.33(2)°$ [Catti, 1977].

There are four formula units per unit cell. The structure is composed of double chains of …$CaPO_4$ $CaPO_4$ $CaPO_4$… extending along the *a*-axis and linked together in the *b*-axis direction by Ca-O bonds to form distorted sheets of atoms approximately in the

(001) plane (Figure 1.4). The center of simmetry produces another sheet below this in the *c*-axis direction.

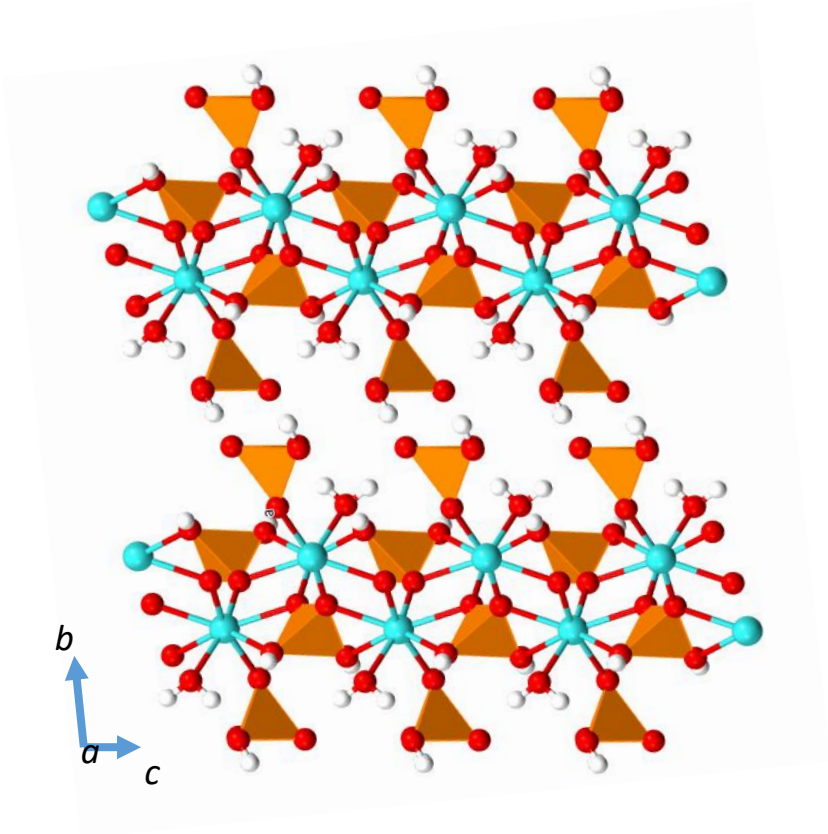

Figure 1.4 - Double chain of Ca^{2+} ions (in blue) and phosphates ions (orange tetrahedral) that characterize the DCPA structure.

2.3 Brushite

Dicalcium phosphate dihydrate (DCPD, $CaHPO_4 \cdot 2\ H_2O$) is also referred to as calcium monohydrogen phosphate dihydrate or dibasic calcium phosphate dihydrate or calcium hydrogen orthophosphate 2-hydrate. Its mineral (brushite) was discovered in 1865 and named after the mineralogist G.J. Brush. Brushite occurs as a component of rock-phosphate deposits and in dental calculus and other pathological calcifications [Elliott, 1994]. DCPD can occur as an intermediate in the apatitic mineralization and dissolution processes. DCPD can be easily crystallized from aqueous solutions and at temperatures above 80 °C it transforms into the anhydrous form DCPA.

DCPD crystallizes in a monoclinic structure, space group Ia and unit cell *a* = 5.812(2) Å, *b* = 15.180(3) Å, *c* = 6.239(2) Å, and β = 116,25(2)°. The asymmetric unit is $CaHPO_4 \cdot 2\ H_2O$ with four formula units per unit cell.

The structure contains columns of alternating Ca^{2+} and HPO_4^{2-} ions, which run parallel to the short diagonal of the (010) face of the unit cell. A striking feature of this structure is that these columns are joint together to form corrugated sheets (Figure 1.5). The sheets, that result to have a composition of $CaHPO_4$ are normal to the *b*-axis and are linked together by water molecules.

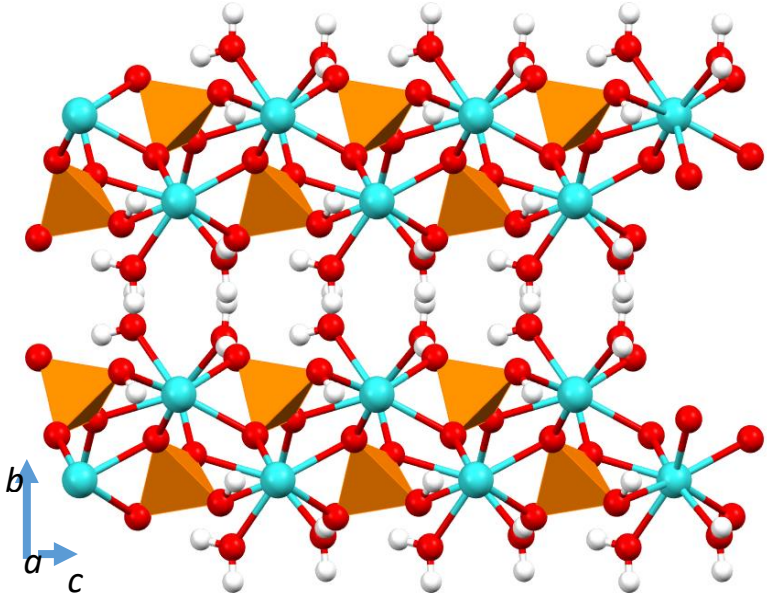

Figure 1.5 – Structure of the corrugated sheets that characterize DCPD.
The a-axis is into the plane. Ca^{2+} ions are in blue and phosphates ions are orange tetrahedra.

2.4 Beta-Tricalcium Phosphate

β-tricalcium phosphate (β-TCP, β-$Ca_3(PO_4)_2$) and its polymorph α-tricalcium phosphate (α-TCP, α-$Ca_3(PO_4)_2$) are also referred to as tricalcium diorthophosphates. The β-TCP to α-TCP transition temperature is 1125 °C. Another high temperature phase called super-α-TCP (ᾱ-TCP,ᾱ-$Ca_3(PO_4)_2$) was discovered in 1959, but it is stable only above 1430 °C and it is unable to survive quenching to room temperature [Elliott, 1994].

β-TCP has been identified during pathological calcifications, such as dental calculi and renal stones, but it has not been observed in enamel, dentin, or bone. The ideal β-TCP structure contains calcium ion vacancies that are too small to accommodate a calcium ion but allow for the inclusion of magnesium ions. Indeed, the most common tricalcium phosphate formed under physiological conditions is whitlockite, which is stabilized by magnesium ions and is not detected physiologically, unless magnesium ions are present.
β-TCP structure is quite complex (Figure 1.6). It crystallizes in the rhombohedral space group R3c, and its unit cell contains 21 [$Ca_3(PO_4)_2$] formula units, 273 atoms in total. Calcium ions in β-TCP occupy five different cation sites: Ca(1), Ca(2) and Ca(3) are on general positions with eight to nine coordinated oxygens, whereas both Ca(4) and Ca(5) are on special positions, with an effective multiplicity of 1/3 of the other cation sites. Ca(5) exhibits an approximately octahedral coordination, Ca(4) site is only half occupied and exhibits a quite distorted nine coordination [Yashima, 2003]. There are three types of crystallographically nonequivalent PO_4^{3-} groups located at general points of the crystal, each type with different intra tetrahedral bond lengths and angles [Dickens, 1974]. β-TCP structure can be described as a regular assembly of two kinds of columns in which Ca atoms and phosphate tetrahedra are stacked. As shown in Figure 1.6, the unit cell view down *c*-axis allows to identify A-type columns filled with Ca(4), Ca(5) and P(1) whereas B-type columns contain Ca(1), Ca(2) Ca(3) and P(2) and P(3). A-type columns are surrounded only by B-type ones.

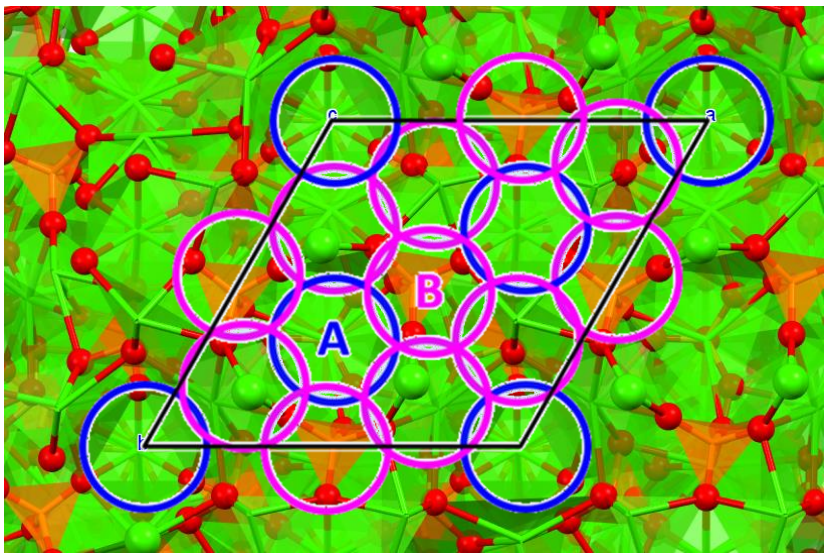

Figure 1.6 – β-TCP structure view down *c*-axis. A- and B-type columns are put into evidence.

3. Gelatin

Several polymers of both natural and synthetic origin have been used for a variety of biomedical applications including pharmaceutical preparations, drug targeting, imaging, drug delivery, prosthetics, and tissue engineering scaffolds.

Due to their reproducible characteristics in terms of their molecular weight, degradation and mechanical properties, synthetic polymers are attractive for a variety of the aforementioned applications. However, synthetic polymers from the biological standpoint often lack much-desired bioactivity and biocompatibility, which may translate into adverse side effects. Natural polymers on the other hand are abundant and resemble the components present in biological extracellular matrices. Thus, natural polymers are readily accepted by the body and possess high bioactivity and biocompatibility.

For some applications including drug delivery and temporary scaffolds, biodegradability is also required, where the biodegradable polymers are able to degrade over a desired period of time. Therefore, both the polymer and its degradation products should not provoke any negative host response.

Natural polymers include also the biopolymers, polymers produced by living organisms or, in other words, polymeric biomolecules.

There are three main classes of biopolymers, classified according to the monomeric units used and the structure of the biopolymer formed [Gorgieva, 2011]:

- polynucleotides (RNA and DNA), which are long polymers composed of 13 or more nucleotide monomers;
- polypeptides, which are polymers of amino acids;
- polysaccharides, which are often linear bonded polymeric carbohydrate structures.

Because of the wide applicability of these polymers, they are used in a lot of different branches of the medicine and with various applications: pharmacological, mechanical support, mechanical barrier, artificial tissue/organs, and carriers for cells, drugs and bioactive molecules.

Generally, for tissue regeneration, biomaterials derived from extracellular matrix protein such as collagen or gelatin (a denatured form of collagen extracted mainly from bovine or porcine skin and bones) are preferred, because they are able to support

cellular growth, undergo cell-mediated enzymatic degradation and can make a better interaction with the natural environment [Alarake, 2017].

The collagen molecules assume a triple helix conformation which is made up of three amino acid chains characterized by the succession of a Gly-X-Y triplet [Malafaya, 2007] where X and Y are, in most cases, Pro and Hyp [Brodsky, 1997]. The triple helix of collagen is particularly stable mainly thanks to the possibility of forming hydrogen bonds between the amino groups of the glycine of one chain and the carboxyl groups present in the Y residues of another chain. The hydrogen bonds that can form between the chain and the water molecules also contribute to the stability of the triple helix [Shanmugam, 2009].

Gelatin can be industrially obtained by different methods, which involve some main stages: pretreatment of the raw material, extraction of the gelatin, purification and drying of gelatin [Malafaya, 2007]. Approximately 80% of the edible gelatin produced in Europe is made from pork skins. Fifteen per cent is made from split. Split is a thin, collagen-containing layer of the cattle hide that lies between the epidermis and subcutaneous layer. The remaining 5 per cent of gelatin comes from porcine and bovine bones and fish skin (https://www.gelatine.org/en/gelatine/manufacturing.html). Depending on the kind of pretreatment, two gelatin types can be distinguished:

- Type A gelatin (isoelectric point at pH 6-9) that is produced from acid-treated collagen;
- Type B gelatin (isoelectric point at pH 5) that is produced from alkali-treated collagen.

Gelatin structure preserves some oriented fragments of pristine collagen, but mostly presents loose chains, which makes this material very versatile. However, the fields and possibilities of use of gelatin are limited by poor mechanical properties and by its high solubility in a physiological environment. These negative aspects can be improved through crosslinking with chemical agents or physical treatments [Amadori, 2015]. Physical methods include hydrothermal treatment, treatment with γ or UV rays, while the main chemical agents include dialdehydes, diisocyanates, genipin, carbodimides, polyepoxy compounds [Amadori, 2015]. In general, protein crosslinking can also be done by reaction with polyphenols [Hosseini, 2018].

4. Functionalization

Biomaterials based on calcium phosphates and/or gelatin have recently registered significant improvement in their performance thanks to innovative approaches based on biomimetic strategies, as well as to their functionalization with biological relevant ions, molecules and macromolecules, growth factors and drugs. Applications of functionalized and multi-functionalized materials may range from coatings to bone cements, scaffolds for regenerative medicine, delivery systems for therapeutic agents [Bigi, 2017]. In this thesis work both the functionalization with different metals - in the form of substituting ions or metallic nanoparticles – and organic molecules – in the form of small molecules, polymers or drugs – have been explored.

4.1 Metals

The use of hydroxyapatites, and more generally of calcium phosphates, in association with metals of a certain biological relevance allows to combine the excellent biocompatibility and bioactivity characteristics of calcium phosphates with the peculiar biological properties of the metal. The metal can be present in the form of a substituting cation in the structure of calcium phosphate or in the form of metallic nanoparticles chemically bound to calcium phosphate crystals surfaces.

4.1.1 Platinum

Platinum is a noble metal and platinum coordination compounds, such as the cis- [$PtCl_2(NH_3)_2$] complex known as cis-platinum, have been used as anticancer agents for a long time. In particular, this thesis work focuses on the role of Platinum nanoparticles (PtNPs).

There are two different methods of synthesis of nanoparticles: the top down method and the bottom up method. The first method consists in reducing the bulk material until a nanometer-sized material is obtained. This process can be operated using thermal or high-energy methods, through the use of mechanical energy or optical lithography. However, the main limitation of top-down methods is the control of the size and shape of the final material. The bottom up method, on the other hand, involves the aggregation of atoms and molecules until the desired dimensions are reached. This method exploits the chemical reduction of metal precursors to obtain nanoparticles. The reduction

processes consist of three phases: nucleation, growth and aggregation. The last phase of aggregation of the nanoparticles must be avoided, normally through the use of stabilizing agents, since it leads to the formation of the massive phase, thermodynamically favored, with consequent loss of the particular properties associated with the nanoparticles [Roucoux, 2002].

Over the last years, interest in the study of metal nanoparticles has increased as they have chemical-physical properties that are very different from the bulk material and for this reason they have many different applications, including as therapeutic or contrast agents in the biomedical field [Bendale, 2017].

In particular, PtNPs have been demonstrated to exert cytotoxic effects on cancer cells, thus resulting in powerful anticancer agents, able to induce cell apoptosis and block the cellular reproduction cycle [Tahir, 2017]. Furthermore, these nanoparticles are known for their ability to remove reactive species (superoxide and peroxide) by acting similarly to two biological enzymes, catalase and superoxide dismutase (SOD) [Yoshihisa, 2011]. The ability to mimic the activity of SOD / catalase favors the prevention of numerous diseases associated with oxidative stress, such as inflammation, arteriosclerosis and neurodegenerative diseases [Hikosaka, 2008].

4.1.2 Strontium

Strontium is naturally present in the mineral phase of bone tissue, especially in areas with a high metabolic turnover [Marie, 2001]. It is shown, from in vitro and in vivo studies, that the presence of Sr^{2+} ions influences the regeneration cycle of bone tissue, increasing the number of osteoblasts and decreasing the number and activity of osteoclasts, and therefore promotes the formation of new bone tissue and slows down tissue resorption. Furthermore, it has been shown that the administration of strontium induces an increase in mass and bone strength, which makes it very useful in the treatment of diseases such as osteoporosis, which manifests itself with an abnormal increase in bone fragility. In particular, it has been shown that treatment with strontium ranelate promotes an increase in the formation of mineralized nodules in osteoblast cultures and preserves the general structure of the bone matrix [Boivin, 2010].

Furthermore, the studies on strontium substitution in calcium phosphates are aimed to clarify the modifications induced by this ion on the chemistry, structure and morphology of these compounds. Strontium can replace calcium in the structure of

hydroxyapatite in the whole range of composition provoking an enlargement of the unit cell, coherently with its bigger ionic radius [Bigi, 2007]. On the other hand, the structures of the α form of tricalcium phosphate, as well as octacalcium phosphate and brushite, can support much smaller amount of strontium substitution for calcium [Saint-Jean, 2005; Boanini, 2010; Boanini, 2021].

At the same time, ion substitution has been studied to verify the possible use of calcium phosphates as delivery systems of strontium [Salamanna, 2019]. In particular, previous studies have made it possible to verify that Strontium is able to influence cellular behavior even when incorporated into the structure of hydroxyapatite, both in normal bone cells and in osteopenic bone cells [Cappuccini, 2009].

4.1.3 Zinc

Zinc is a trace element that is essential for human health, present in the body in greater quantities than any other trace element other than iron. It is related to the normal absorption and action of vitamins, in particular of the B complex. It is a constituent element of over two thousand enzymes responsible for management and metabolism, including carbonic anhydrase, necessary for the relationship of tissues. It is important for tissue repair and for an efficient immune response to infections; it also has an antioxidant activity, since it reduces the formation of free radicals.

Zinc is an important metal in the normal growth and development of the skeletal system, where it has been shown to display an inhibitory effect on osteoclast differentiation and a promotion of osteoblast activity [Moonga, 1995].

Zn ion is one of the most effective metal ions in inhibiting HA crystal growth [Kanzaki, 2000]. Nonetheless, it can be quantitatively incorporated into HA lattice by direct synthesis under mild conditions [Bigi, 1995], through hydrothermal technique at 200 °C [Li, 2008] and by means of a sol–gel process [Kalita, 2007].

The lattice parameters of Zn-substitutes hydroxyapatites are related to the difference in ionic radius between Zn^{2+} (0.074 nm) and Ca^{2+} (0.099 nm). The reported substitution limit of Zn in HA varies between 15% and 25%, due to a significant local structural distortion. Furthermore, both Ca/P and (Ca+Zn)/P ratios decrease on increasing Zn content and, as a consequence, stoichiometry is no longer maintained [Bigi, 1995]. The amount of zinc which can be hosted in the structure of other calcium phosphates is even more limited [Boanini, 2021; Kawabata, 2011].

4.2 Organic molecules

4.2.1 β-Lactams

The enhancement of the efficacy of cell adhesion and differentiation plays a leading role in the improvement of biological tissues regeneration, In this aspect, integrins could represent an important cellular target, since they mediate important cellular events such as adhesion, migration, differentiation, growth, and survival [Barczyk, 2010]. Integrins are transmembrane receptors composed by two protein chains α and β, which upon binding to specific ligands could regulate cell-cell and cell-extracellular matrix interactions. In mammals, 24 different αβ heterodimers have been recognized and some heterodimers are important mediators of bone-cells function [Marie, 2013].

In osteoclasts, for instance, integrin αvβ3 is essential for the attachment to matrix proteins of bone and for cell spreading necessary for the bone-resorbing activity [Duong, 2000]. In addition, also osteoblasts express some integrins able to control their differentiation and fate [Brunner, 2018].

Biomaterials for bone regeneration should exhibit high cell adhesion to retain effectively anchorage-dependent osteo-progenitors, such as human bone marrow-derived mesenchymal stem cells (MSCs). Moreover, it has been demonstrated that an adequate number of osteoprogenitors is a requisite for an efficient bone repair [Samsonraj, 2017].

Previous studies provided a series of new β-lactam-based molecules able to modulate cell adhesion on targeting different integrins [Baiula, 2016]. Some of the molecules acted as agonists, promoting cell adhesion and activation of intracellular signalling, others resulted antagonists inhibiting integrin-dependent processes. Functionalization of hydroxyapatite with β-lactam agonists could produce new functional materials with a cell-targeted specificity because of their integrin selectivity.

4.2.2 Aspartic and poly-aspartic acid

Biomineralization in bone and teeth involves the deposition of calcium phosphates onto an extracellular matrix, constituted of collagen fibrils, and several non collagenous proteins, rich in anionic aminoacids, which can interact with the growing crystals. The non collagenous proteins of bone and teeth contain significant amount of carboxylate groups. Carboxylic acid side chains, and more specifically a high aspartic and glutamic

amino acid residue content is considered to be an important requirement of the matrix proteins involved in the nucleation of calcium phosphates [Hunter, 1994]. This has prompted a number of studies on the preparation of hydroxyapatite nanocrystals in the presence of aspartic acid. Understanding how this amino acid interact with hydroxyapatite structure, and clarifying its role in the control of the properties of the apatitic crystals is of interest both for the development of biomaterials suitable to repair the skeletal system, as well as for a better understanding of the natural processes [Gonzalez-McQuire, 2004; Boanini, Fini, *et al.*, 2006]. It was found that the presence of aspartic acid in the reaction solution does not inhibit nucleation of hydroxyapatite, but reduces the growth of the composite nanocrystals in agreement with the increase of the surface area on increasing amino acid content. The overall reduction of crystals dimensions does not modify the morphology of the composite nanocrystals, suggesting an isotropic interaction. Furthermore, the presence of the acidic amino acid in the composite nanocrystals favours osteoblast proliferation and promotes their metabolism and differentiation [Boanini, Torricelli, *et al.*, 2006].

Due to their relative high charged groups content, acidic macromolecules can easily interact with the charged surfaces of the growing inorganic crystals. The interaction can be specific, with the protein adopting a conformation and exhibiting charge distribution and repeating distances matching some structural motif of the crystal, or even non-specific, due to multiple electrostatic interactions [Berman, 1990]. The possibility of poly-aspartate to assume a β-sheet conformation could imply a better fit with apatitic structure. Indeed, differently from the small aspartic acid molecule, poly-L-aspartate macromolecule has been reported to inhibit hydroxyapatite nucleation and growth, when present in the reaction environment. The polymer is incorporated into the obtained inorganic crystals through a specific interaction due to a molecular recognition process. The greater effect exerted along the direction perpendicular to the *c*-axis is supported by the results of the structural analysis, and confirmed by the variation of crystal morphology [Bigi, 2004].

Moreover, poly-aspartate macromolecule has been shown to act as crystal nucleators when immobilized on a surface [Tsortos, 2002]. This is in agreement with the numerous evidences suggesting that the same macromolecule that acts as an inhibitor when in solution, can promote nucleation and/or growth when adsorbed on a substrate.

4.2.3 Polyphenols

Polyphenols are molecules characterized by the presence of multiple phenolic rings. They are present in plants, in which they serve numerous purposes toward survival and security, including pigmentation, photoprotection and multimodal defence against herbivores, pathogenic invasions and mechanical injuries [He, 2012]. Recently, polyphenols, such as quercetin and curcumin, have been used in the biomedical field for conferring antioxidant activity to biomaterials due to their free-radical scavenging capacities. Not only the antioxidant activity of polyphenols, but also their other features, such as anti-allergenic, anti-inflammatory, antimicrobial and cardioprotective properties, make these compounds very interesting raw materials for medical applications [Forte, 2016].

The production of free radicals such as nitric oxide ($NO^{\cdot}$), nitrogen dioxide (NO_2) and peroxynitrite ($ONOO^-$) and the reactive oxygen species (also known as ROS) is a natural process and also a health problem when the immunological defences are not able to neutralize them. These phenolic compounds, however, can act as free radical-scavenging antioxidants. This function is carried out by the transfer of a hydrogen atom or an electron (followed by proton transfer) from the phenolic compound to the radical, before the latter can attack biologically essential molecules. This transfer produces a stable compound and it is possibly due to the presence of free OH groups on the flavonoid skeleton. The property also depends on the pattern (both number and location) of these free OH groups.

The two reactions are shown in the scheme below [He 2012]:

(1) $R\bullet + ArOH \rightarrow RH + ArO\bullet$

(2) $R\bullet + ArOH \rightarrow R^- + ArOH^+\bullet$

In reaction (1), the antioxidant ArOH transferred a hydrogen atom to the free radical R• yielding less reactive products, RH and ArO•; this antioxidant action depends on the bond dissociation enthalpy of the ArO-H bond; lower is the bond dissociation enthalpy value, and also easier will be the reaction with the free radicals.

In reaction (2), an electron of the antioxidant was donated to the R• and got stable products.

Together with scavenging free radicals, polyphenols may entrap metals and prevent their participation in the reactions generating free radicals; chelating these metals can effectively reduce oxidation [He, 2012]:

(3) $M^{n+} + H_2O_2 \rightarrow OH^- + OH\bullet + M^{(n+1)+}$

Quercetin (3,3',4',5,7–pentahydroxy-flavone) is a flavonoid known for its pharmacological activities. It is a yellow solid, soluble in organic solvents such as ethanol, DMSO, and dimethyl formamide. The solubility of quercetin in these solvents is approximately 2 mg/ml in ethanol and 30 mg/ml in DMSO and DMF. Quercetin is sparingly soluble in aqueous solutions. The biochemical activity of quercetin depends on the structure and the relative orientation of the rings and of the hydroxyl groups inside the molecule (Figure 1.7). The B ring hydroxyl configuration mostly determines the antioxidant effect, while the activity of the other hydroxyl position is not yet clear [Heim, 2003].

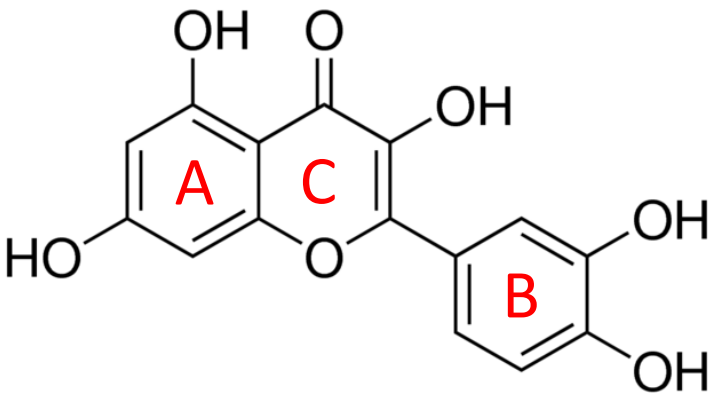

Figure 1.7 - Molecular structure of quercetin with ring lettering convention.

Quercetin molecular dimensions are similar to those between the Ca^{2+} ions on the (110) face of hydroxyapatite. Moreover, quercetin has a negative charge on the molecular plane and so it could be attracted by the calcium ions present in the hydroxyapatite structure. On this basis, it has been suggested that quercetin could act as soft template in the regulation of crystal growth direction of hydroxyapatite [Liu, 2012].

Curcumin ((1E, 6E) -1,7-bis (4-hydroxy-3-methoxyphenyl) -1,6-heptadiene-3,5-dione); chemical formula: C21H20O6; MW: 368.38 gmol-1) has two di-substituted aromatic systems separated by a linker: a β-diketone α, β-unsaturated (Figure 1.8).

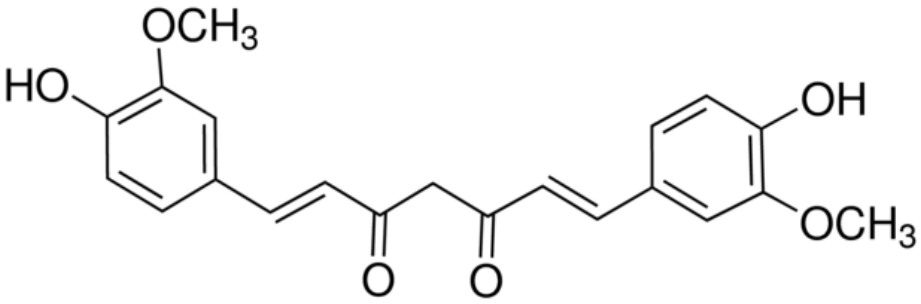

Figure 1.8 - Curcumin molecule

This molecule is able to establish a keto-enol balance influenced by the pH: the keto form prevails for pH values <8.5; whereas once this pH value is exceeded, the prevailing form is the enol form.

Curcumin is a hydrophobic molecule that shows a particular solubility in polar solvents (eg DMSO, methanol, ethanol, acetonitrile, chloroform, ethyl acetate, etc.) and a moderate solubility in hydrocarbon solvents such as hexane and cyclohexane. Although the lipophilic character of curcumin favors the permeation through biological membranes, its poor solubility in water, reduced capacity of oral absorption and poor bioavailability involve a strong limitation of its therapeutic properties. These drawbacks, which are characteristic also of quercetin, have promoted interest towards the research of materials that can be used as delivery systems for the local administration of these polyphenols [Patel, 2012; Chen, 2017; Zhang, 2010; Forte, 2016].

INTRODUCTION – References

- Alarake NZ, Frohberg P, Groth T, Pietzsch M. Mechanical properties and biocompatibility of in situ enzymatically cross-linked gelatin hydrogels. Int. J. Artif. Organs 2017;40(4):159-168
- Amadori S, Torricelli P, Rubini K, Fini M, Panzavolta S, Bigi A. Effect of sterilization and crosslinking on gelatin films. J. Mater. Sci.: Mater. Med. 2015;26:69
- Baiula M, Galletti P, Martelli G, Soldati R, Belvisi L, Civera M, Dattoli SD, Spampinato SM, Giacomini D. New β-lactam derivatives modulate cell adhesion and signaling mediated by RGD-binding and leukocyte integrins. J. Med. Chem. 2016;59: 9721–9742
- Barczyk M, Carracedo S, Gullberg D. Integrins, Cell Tissue Res. 2010;339:269–280
- Bendale Y, Bendale V, Paul S. Evaluation of cytotoxic activity of platinum nanoparticles against normal and cancer cells and its anticancer potential through induction of apoptosis. Integr. Med. Res. 2017;6:141-148
- Berman A, Addadi L, Kvick A, Leiserowitz L, Nelson M, Weiner S. Intercalation of sea urchin proteins in calcite: study of a crystalline composite material. Science 1990;250(4981):664-667
- Bigi A, Boanini E. Functionalized biomimetic calcium phosphates for bone tissue repair. J. Appl. Biomater. Funct. Mater. 2017;15:e313–e325
- Bigi A, Boanini E, Capuccini C, Gazzano M. Strontium-substituted hydroxyapatite nanocrystals. Inorg. Chim. Acta. 2007;360:1009–1016
- Bigi A, Boanini E, Gazzano M, Kojdecki MA, Rubini K. Microstructural investigation of hydroxyapatite-polyelectrolyte composites. J. Mater. Chem. 2004;14:274-279
- Bigi A, Foresti E, Gandolfi M, Gazzano M, Roveri N. Inhibiting effect of zinc on hydroxylapatite crystallization. J. Inorg. Biochem. 1995;58:49-58
- Boanini E, Fini M, Gazzano M, Bigi A. Hydroxyapatite nanocrystals modified with acidic amino acids. Eur. J. Inorg. Chem. 2006;2006:4821-4826
- Boanini E, Gazzano M, Bigi A. Ionic substitutions in calcium phosphates synthesized at low temperature. Acta Biomater. 2010;6:1882-1894
- Boanini E, Silingardi F, Gazzano M, Bigi A. Synthesis and hydrolysis of brushite (DCPD): the role of ionic substitution. Cryst. Growth Des. 2021;21:1689–1697
- Boanini E, Torricelli P, Gazzano M, Giardino R, Bigi A. Nanocomposites of hydroxyapatite with aspartic acid and glutamic acid and their interaction with osteoblast-like cells. Biomaterials 2006;27:4428–4433

- Boivin G, Farlay D, Khebbab MT, Jaurand X, Delmas PD, Meunier PJ. In osteoporotic women treated with strontium ranelate, strontium is located in bone formed during treatment with a maintained degree of mineralization. Osteoporos. Int. 2010;21:667–677
- Brodsky B, Ramshaw JAM. The collagen triple-helix structure. Matrix Biol. 1997;15: 545-554
- Brown WE, Chow LC. ‘‘A new calcium phosphate, water-setting cement, in Cements research progress, (PW Brown ed.), American Ceramic Society: Westerville, Ohio, 1986, pp. 351-379
- Brunner M, Mandier N, Gautier T, Chevalier G, Ribba AS, Guardiola P, Block MR, Bouvard D. β1 integrins mediate the BMP2 dependent transcriptional control of osteoblast differentiation and osteogenesis. PLoS One 2018;13:e0196021
- Capuccini C, Torricelli P, Boanini E, Gazzano M, Giardino R, Bigi A. Interaction of Sr-doped hydroxyapatite nanocrystals with osteoclast and osteoblast-like cells. J. Biomed. Mater. Res. A 2009;89(3):594-600
- Catti M, Ferraris G, Filhol A. Hydrogen bonding in the crystalline state. $CaHPO_4$ (Monetite), P-1 or P1? A novel neutron diffraction study. Acta Cryst. 1977;B33:1223-1229
- Chen M, Liu F, Chiou BS, Sharif HR, Xu J, Zhong F. Characterization of film-forming solutions and films incorporating free and nanoencapsulated tea polyphenol prepared by gelatins with different bloom values. Food Hydrocoll. 2017;72:381–388
- Dickens B, Schroeder LW, Brown WE. Crystallographyc studies of the role of Mg as a stabilizing impurity in β-$Ca_3(PO_4)_2$. J. Solid State Chem. 1974;10:232-248
- Duong LT, Lakkakorpi P, Nakamura I, Rodan GA. Integrins and signaling in osteoclast function. Matrix Biol. 2000;19:97–105
- Elliott JC. Structure and chemistry of the apatites and other calcium orthophosphates. Elsevier: Amsterdam, 1994
- Featherstone JDB, Mayer I, Driessens FCM, Verbeeck RMH, Heijligers M. Synthetic apatites containing Na, Mg, and CO_3 and their comparison with tooth enamel mineral. Calcif. Tissue Int. 1983;35:169–171
- Festas AJ, Ramos A, JP Davim. Medical devices biomaterials – a review. Proc. Inst. Mech. Eng. L: J. Mater.: Des. Appl. 2020;234:218–228
- Forte L, Torricelli P, Boanini E, Gazzano M, Rubini K, Fini M, Bigi A. Antioxidant and bone repair properties of quercetin-functionalized hydroxyapatite: an in vitro osteoblast-osteoclast-endothelial cell co-culture study, Acta Biomater. 2016;32:298-308

- Gonzalez-McQuire R, Chane-Ching JY, Vignaud E, Lebugle A, Mann S. Synthesis and characterization of amino acid-functionalized hydroxyapatite nanorods. J. Mater. Chem. 2004;14:2277–2281
- Gorgieva S, Kokol V. Collagen-vs. gelatin-based biomaterials and their biocompatibility: review and perspectives, in biomaterials applications for nanomedicine (R Pignatello ed.), InTech Europe: Rijeka, Croatia, 2011, pp. 17-51
- He C, Pan Y, Ji X, Wang H. Antioxidants : introduction, in antioxidant polymers : synthesis, properties, and applications (G Cirillo, F Iemma, eds.), John Wiley and Sons, 2012, pp. 1-16
- Heim KE, Tagliaferro AR, Bobilya DJ. Flavonoid antioxidants: chemistry, metabolism and structure-activity relationships. J. Nutr. Biochem. 2003;10:572-584
- Hikosaka K, Kim J, Kajita M, Kanayama A, Miyamoto Y. Platinum nanoparticles have an activity similar to mitochondrial NADH: ubiquinone oxidoreductase. Colloids Surf. B: Biointerfaces, 2008;66:195–200
- Hosseini SF, Gómez-Guillén MC. A state-of-the-art review on the elaboration of fish gelatin as bioactive packaging: special emphasis on nanotechnology-based approaches. Trends Food Sci. Technol. 2018;79:125–135
- https://www.gelatine.org/en/gelatine/manufacturing.html
- Hunter GK, Goldberg HA. Modulation of crystal formation by bone phosphoproteins: role of glutamic acid-rich sequences in the nucleation of hydroxyapatite by bone sialoprotein. Biochem. J. 1994;302:175–179
- Jain JP, Ayen WY, Domb AJ, Kumar N. Biodegradable polymers in drug delivery, in Biodegradable polymers in clinical use and clinical development (AJ Domb and N Kumar eds.), John Wiley and Sons, 2011, pp. 3–58
- Johnsson MS, Nancollas GH. The role of brushite and octacalcium phosphate in apatite formation. Crit. Rev. Oral. Biol. Med. 1992;3(1-2):61-82
- Kalita SJ, Bhatt HA. Nanocrystalline hydroxyapatite doped with magnesium and zinc: synthesis and characterization. Mater. Sci. Eng. C 2007;27:837–848
- Kanzaki N, Onuma K, Treboux G, Tsutsumi S, Ito A. Inhibitory effect of magnesium and zinc on crystallization kinetics of hydroxyapatite (0 0 0 1) face. J. Phys. Chem. B 2000;104:4189–4194
- Kawabata K, Yamamoto T, Kitada A. Substitution mechanism of Zn ions in β-tricalcium phosphate. Phys. Rev. B Condens. Matter 2011;406:890–894
- Lam MT, Wu JC. Biomaterial applications in cardiovascular tissue repair and regeneration. Expert Rev. Cardiovasc. Ther. 2012;10(8):1039-1049
- Langer R, Tirrell DA. Designing materials for biology and medicine. Nature 2004;428: 487–492

- LeGeros RZ. Calcium phosphate-based osteoinductive materials. Chem. Rev. 2008; 108:4742-4753
- Lénart G, Bidló G, Pintér J. Some basic problems in the examination of the calcium hydrogen phosphates of bone. Clin. Orthop. Rel. Res. 1972;83:263-272
- Li M, Xiao X, Liu R, Chen C, Huang L. Structural characterization of zinc-substituted hydroxyapatite prepared by hydrothermal method. J. Mater. Sci.-Mater. Med. 2008;19:797–803
- Lijun W, Nancollas GH. Calcium orthophosphates: crystallization and dissolution. Chem. Rev. 2008;108:4628-4669
- Liu X, Lin K, Qian R, Chen L, Zhuo S, Chang J. Growth of highly oriented hydroxyapatite arrays tuned by quercetin. Chem. Eur. J. 2012;18:5519–5523
- Lynn AK, Bonfield W. A novel method for the simultaneous, titrant-free control of pH and calcium phosphate mass yield. Acc. Chem. Res. 2005;38:202-207
- Malafaya PB, Silva GA, Reis RL. Natural-origin polymers as carriers and scaffolds for biomolecules and cell delivery in tissue engineering applications. Adv. Drug Deliv. Rev. 2007;59:207-233
- Marie PJ. Targeting integrins to promote bone formation and repair. Nat. Rev. Endocrinol. 2013;9:288–295
- Marie PJ, Ammann P, Boivin G, Rey C. Mechanisms of action and therapeutic potential of strontium in bone. Calcif. Tissue Int. 2001;69:121–129
- McDowell H, Gregory TM, Brown WE. Solubility of $Ca_5(PO_4)_3OH$ in the system $Ca(OH)_2$–H_3PO_4–H_2O at 5, 15, 25, and 37°C. J. Res. Natl. Bur. Stand. A Phys. Sci. 1977;81A:273–281
- Moonga BS, Dempster DW. Zinc is a potent inhibitor of osteoclastic bone resorption in vitro. J. Bone Miner. Res. 1995;10:453–457
- Patel AR, Heussen PCM, Hazekamp J, Drost E, Velikov KP. Quercetin loaded biopolymeric colloidal particles prepared by simultaneous precipitation of quercetin with hydrophobic protein in aqueous medium. Food Chem. 2012;133: 423–429
- Roucoux A, Schulz J, Patin H. Reduced transition metal colloids: a novel family of reusable catalysts? Chem. Rev. 2002;102(10):3757-3778
- Saint-Jean SJ, Camirè CL, Nevsten P, Hansen S, Ginebra MP. Study of the reactivity and in vitro bioactivity of Sr-substituted α-TCP cements. J. Mater. Sci. Mater. Med. 2005;16:993–1001
- Salamanna F, Giavaresi G, Contartese D, Bigi A, Boanini E, Parrilli A, Lolli R, Gasbarrini A, Barbanti Brodano G, Fini M. Effect of strontium substituted ß-TCP associated to mesenchymal stem cells from bone marrow and adipose tissue on spinal fusion in healthy and ovariectomized rat. J. Cell. Physiol. 2019;234:20046–20056

- Salgado AJ, Coutinho OP, Reis RL. Bone tissue engineering: state of the art and future trends. Macromol. Biosci. 2004;4:743-765
- Samsonraj RM, Raghunath M, Nurcombe V, Hui JH, van Wijnen AJ, Cool SM. Concise review: multifaceted characterization of human mesenchymal stem cells for use in regenerative medicine. Stem Cells Transl. Med. 2017;6:2173–2185
- Shanmugam G, Polavarapu PL, Structural transition during thermal denaturation of collagen in the solution and film states. Chirality 2009;21:152-159.
- Tahir K, Nazir S, Ahmad A, Li B, Ullah Khan A, Khan ZUH, Ullah Khan F, Ullah Khan Q, Khan A., Ur Rahman A. Facile and green synthesis of phytochemicals capped platinum nanoparticles and in vitro their superior antibacterial activity. J. Photochem. Photobiol. B 2017;166:246–251
- Tsortos A, Nancollas GH The role of polycarboxylic acids in calcium phosphate mineralization J. Colloid Interface Sci. 2002;250:159-167
- Williams DF. On the nature of biomaterials. Biomaterials 2009;30:5897–5909
- Yashima M, Sakai A, Kamiyama T, Hoshikawa A. Crystal structure analysis of β-tricalcium phosphate $Ca_3(PO_4)_2$ by neutron powder diffraction. J. Solid State Chem. 2003;175:272–277
- Yoshihisa Y, Zhao Q, Hassan MA, Wei Z, Furuichi M, Miyamoto Y, Kondo T, Shimizu T. SOD / catalase mimetic platinum nanoparticles inhibit heat-induced apoptosis in human lymphoma U937 and HH cells. Free Radic. Res. 2011;45(3):326-335
- Young RA, Brown WE. Structures of biological minerals, in Biological mineralization and demineralization (GH Nancollas ed.), Springer-Verlag: Berlin, 1982, pp. 101-141
- Zhang X, Do MD, Casey P, Sulistio A, Qiao GG, Lundin L, Lillford P, Kosaraju S. Chemical cross-linking gelatin with natural phenolic compounds as studied by high-resolution NMR spectroscopy. Biomacromolecules 2010;11:1125–1132

Chapter 2

EXPERIMENTAL SECTION – *Preparation of Materials*

1. Hydroxyapatite (HA)

The synthesis of HA ($Ca_{10}(PO_4)_6(OH)_2$) was carried out in N_2 atmosphere using CO_2 free water. 50 ml of a 1.08 M $Ca(NO_3)_2 \cdot 4H_2O$ solution (pH adjusted to 10 with NH_4OH) was heated at 90°C and 50 ml of 0.65 M $(NH_4)_2HPO_4$ solution was added drop-wise under stirring. The precipitate was maintained in contact with the reaction solution for 5 h at 90 °C under stirring, then centrifuged at 10,000 rpm for 10 min and repeatedly washed with CO_2-free distilled water. The product was dried at 37°C overnight [Boanini, 2020].

1.1 Hydroxyapatite – Polyetyhlenimine (HAPEI)

Hydroxyapatite at different poly(ethylenimine) contents was obtained following the same procedure reported in this Chapter, section 1 and adding PEI to the $Ca(NO_3)_2 \cdot 4H_2O$ solution, before adjusting the pH to 10 with NH_4OH. Poly(ethylenimine) solution (Aldrich, MW~2000) was used. Concentrations of PEI were 4 M calculated on the final volume, the obtained samples were labeled as HAPEI [Boanini, 2020].

1.2 Hydroxyapatite - Platinum

Platinum ions and nanoparticles were loaded on HA or HAPEI (previously functionalized with a coating of poly(ethylenimine), as reported in this Chapter, section 1.1).

For the preparation of the samples loaded with Pt(II) (HA-PtNR and HAPEI-PtNR), 0.500 g of freshly sieved apatitic powder was suspended in 12.5 ml of MilliQ water under stirring. After addition of 12.5 ml of 0.01 M K_2PtCl_4 (> 98%, Strem Chemicals Inc.) solution, stirring was maintained for 1 h at RT, afterwards powder was isolated by filtration on a funnel buckner and dried at 37 °C.

The successive reduction of Pt (II) containing samples was carried out on 0.500 g of powder (HA-PtNR and HAPEI-PtNR), that were suspended into 5 ml of MilliQ water. Subsequently 20 ml of a 0.1 M aqueous solution of $NaBH_4$ (99%, Sigma Aldrich) was

added to the suspension under stirring for 30 min at RT. Then the samples (HA-PtR and HAPEI-PtR) were filtered, washed with water, and dried at 37 °C [Boanini, 2020].
HA-PtTT and HAPEI-PtTT were obtained after heat-treatment of HA-PtR and HAPEI-PtR at 700 °C for 4 h. Although heat treatment provoked complete removal of the polyelectrolyte, the label HAPEI-PtTT was maintained to distinguish these samples from those obtained through heat treatment of HA-PtR (HA-PtTT) [Boanini, 2020].

1.3 Strontium Hydroxyapatite (SrHA)

Sr substituted hydroxyapatite (Ca_{10-x} Sr_x $(PO_4)_6(OH)_2$) was synthesized following the procedure reported in par. 3.1, but the cationic solution was prepared by dissolving the appropriate amounts of $Ca(NO_3)_2{\cdot}4H_2O$ and $Sr(NO_3)_2$ in CO_2-free deionized water before adjusting the pH to 10 with NH_4OH. The total cationic concentration was 1.08 M, and the Sr/(Ca + Sr) molar ratio was 0.1 [Cirillo, 2021].

1.4 Strontium Hydroxyapatite – β-Lactams

β-Lactams compounds evaluated in this study are reported in figure 2.1.

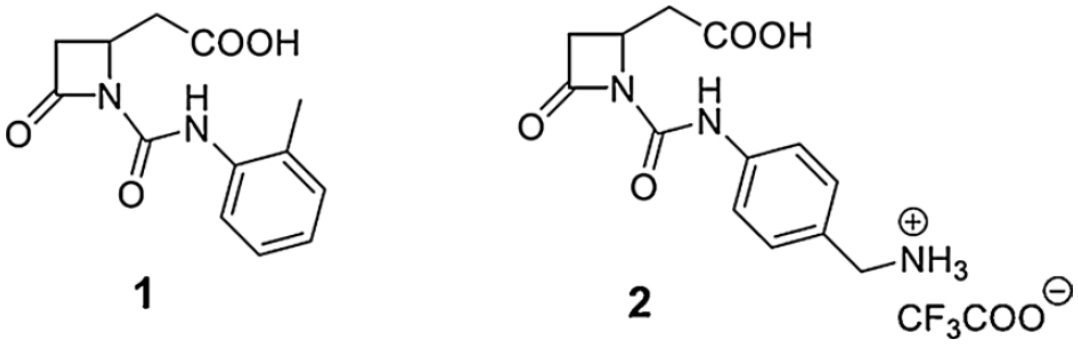

Figure 2.1 – Structure of Compounds 1 and 2 evaluated in this study.

β-Lactams 1 and 2 were loaded on SrHA as follows: the β-lactam (10 mg) was diluted in a 10 mL flask in the appropriate H_2O/MeCN mixture (0.6 mL) (see Table 2.1), then SrHA nanoparticles (60 mg) were added at room temperature (or 70 °C, Table 2.1). After selected time (Table 2.1) the mixture was centrifuged for 5 min. at 1200 rpm. Then, the solid phase was dried at 48 °C for 48 h, and maintained in desiccator ($CaCl_2$) for 24 h before the analyses. The samples are indicated as SrHA**Y**-**X**, where **Y** indicate the two

different β-lactam compounds (1 and 2) and **X** their amount expressed as wt% [Cirillo, 2021].

Table 2.1 – Experimental conditions for loading of β-lactams compounds onto SrHA crystals keeping constant SrHA amount (60 mg), solvent amount (0.6 mL), time (4 h), and temperature (room temperature).

Experiment #	Compound (mg)	Solvent (0.6 mL)
1	1 (10)	CH_3CN
2	1 (10)	H_2O/ CH_3CN 1:3
3	1 (10)	H_2O/ CH_3CN 1:1
4	1 (20)	H_2O/ CH_3CN 1:1
5	1 (6)	H_2O/ CH_3CN 1:1
6	1 (3)	H_2O/ CH_3CN 1:1
7	1 (10)	H_2O/ CH_3CN 3:1
8	1 (10)	H_2O/ CH_3CN 10:1
9	2 (10)	H_2O/ CH_3CN 1:5
10 [a]	2 (10)	H_2O/ CH_3CN 1:5
11	2 (30)	H_2O/ CH_3CN 1:5
12	2 (10)	H_2O/ CH_3CN 1:1
13 [b]	2 (5)	H_2O/ CH_3CN 2:1
14 [b]	2 (10)	H_2O

Notes: [a] Loading at 70 ◦C; [b] Loading overnight.

2. Brushite (DCPD)

Synthesis of brushite ($CaHPO_4 \cdot 2H_2O$) was carried out using 150 mL of a phosphate solution containing 5 mmol of $Na_2HPO_4 \cdot 12H_2O$ and 5 mmol of $NaH_2PO_4 \cdot H_2O$, pH 4.90 adjusted with glacial CH_3COOH. The solution was heated at 37 °C and 50 mL of 0.2 M $Ca(CH_3COO)_2 \cdot H_2O$ was added dropwise over a period of 15 min, under continuous stirring. Afterwards the precipitate was stored in contact with the mother solution for 10 min, filtered, repeatedly washed with bi-distilled water and dried at 37 °C [Rubini, 2019; Boanini, 2021].

2.1 Brushite - polyaspartate (DCPD-PASP)

Syntheses in the presence of the Sodium Polyaspartate (PASP, MW 11,000) were carried out by following the same procedure reported in paragraph 2 and inserting the additive in the phosphate solution before pH correction. PASP concentrations calculated on the final volume were 0.2, 0.5, 0.8, and 1 mM (in monomer), thereby samples were labelled PASP02, PASP05, PASP08, and PASP1, respectively [Rubini, 2019].

2.2 Brushite –aspartic acid (DCPD-ASP)

Syntheses in the presence of Aspartic Acid (ASP) were carried out by following the same procedure reported in this Chapter, section 2 and inserting the additive in the phosphate solution before pH correction. ASP concentrations calculated on final volume were 1, 2, 5, and 10 mM, and samples were labelled ASP1, ASP2, ASP5, and ASP10, respectively [Rubini, 2019].

2.3 Hydrolysis of DCPD – role of ASP and PASP

Hydrolysis of DCPD was carried out in physiological solution (NaCl 0.9%) or in physiological solution containing PASP 0.8 mM in monomer (inPASP08) or ASP 10 mM (inASP10). In addition, brushitic samples synthesized in the presence of PASP and ASP (PASP08 and ASP10) were submitted to incubation in a physiological solution. The reactions of hydrolysis were performed on 100 mg of powder sample incubated into 25 mL solution at 37 °C or 60 °C, up to 72 h. The final solid products were centrifuged at 10,000 rpm for 15 min, then dried at 37 °C.

2.4 Strontium Brushite (SrDCPD)

Sr-substituted DCPD ($Ca_{1-x}Sr_xHPO_4 \cdot 2H_2O$) samples were obtained following the same procedure reported in paragraph 2, but partially replacing $Ca(CH_3COO)_2 \cdot H_2O$ with $Sr(CH_3COO)_2 \cdot ½H_2O$, to prepare solutions with different $[Sr^{2+}/(Ca^{2+} + Sr^{2+})] \cdot 100$ ratios, and a total cation concentration of 0.2 M: compounds were prepared from solutions containing 0, 10, 20, 40, and 60 Sr atom%. Samples were labelled DCPD- 0, DCPD-10, DCPD-20, DCPD-40, and DCPD-60, respectively [Boanini, 2021].

3. Monetite (DCPA)

The synthesis of monetite ($CaHPO_4$) was carried out following two different procedures: (a) direct synthesis and (b) phase transition from DCPD ($CaHPO_4 \cdot 2H_2O$) [Boanini, 2021].

(a) For the direct synthesis of monetite, 50 mL of a 0.65 M $(NH_4)_2HPO_4$ aqueous solution was added dropwise to 50 mL of a 1.08 M $Ca(NO_3)_2 \cdot 4H_2O$ solution maintained at 90°C. The pH of both solutions was not modified, keeping the spontaneous value (about 5). The precipitate was maintained in contact with the reaction solution for 1 h at 90 °C under stirring, then centrifuged at 10,000 rpm for 10 min, washed twice with distilled water and dried at 37 °C.

(b) Thermal treatment of DCPD was performed at 300 ◦C for 30 min.

3.1 Strontium Monetite (SrDCPA)

The synthesis of strontium monetite ($Ca_{1-x}Sr_xHPO_4$) was carried out following two different procedures: (a) direct synthesis and (b) phase transition from SrDCPD ($Ca_{1-x}Sr_xHPO_4 \cdot 2H_2O$) [Boanini, 2021].

(a) Sr substituted monetite was obtained by direct synthesis following the experimental procedure reported in paragraph 3, but including Sr ion in the cationic solution, which was prepared by dissolving the appropriate amounts of $Ca(NO_3)_2 \cdot 4H_2O$ and $Sr(NO_3)_2$ in deionized water. Different samples were prepared from solutions containing 0, 10, 20, 40, 60, 80 and 100 Sr atom%, calculated as $[Sr^{2+}/(Ca^{2+} + Sr^{2+})] \cdot 100$. Total cation concentrations were kept 1.08 M. Samples were labelled DS-0, DS-10, DS-20, DS-40, DS-60, DS-80 and DS-100, respectively.

(b) Thermal treatment of DCPD-0, DCPD-10, DCPD-20, DCPD-40, and DCPD-60 was performed at 300 ◦C for 30 min; afterwards samples were labelled TT-0, TT-10, TT-20, TT-40, and TT-60, respectively.

3.2 β-$SrHPO_4$

For the synthesis of β-$SrHPO_4$, a flask containing 50 ml of 1.08 M $Sr(NO_3)_2$ was placed in an ice bath and the solution was allowed to cool to 5 ◦C, under stirring. Afterwards, dropwise addition of 50 ml of 0.65 M $(NH_4)_2HPO_4$ over a period of 20 min provoked the formation of a precipitate that was maintained in contact with the reaction solution for 1 h at low temperature under stirring, then centrifuged at 10,000 rpm for 10 min, washed twice with distilled water and dried at 37 ◦C.

Partial substitution of Sr with Ca was obtained following the same procedure, but preparing the nitrate solution using the appropriate amounts of $Ca(NO_3)_2{\cdot}4H_2O$ and $Sr(NO_3)_2$: different compounds were prepared from solutions containing 0, 60, 80 and 100 Sr atom%, calculated as [Sr2+/ (Ca2+ + Sr2+)] ·100. Total cation concentrations were kept 1.08 M. Samples were labelled β-0, β-60, β-80 and β-100, respectively [Boanini, 2021].

4. β-TriCalcium Phosphate (β-TCP)

β-TCP (β-$Ca_3(PO_4)_2$) was obtained by solid-state reaction of a mixture of $CaCO_3$ and $CaHPO_4 \cdot 2H_2O$ (DCPD) in the molar ratio of 1:2 at 1000°C for 12 hours. The solid product was ground into a mortar.

4.1 Strontium β-TCP

The first step for the preparation of Sr-substituted β-TCP is the synthesis of α-$Sr_3(PO_4)_2$. α-$Sr_3(PO_4)_2$ was prepared by solid-state reaction at 1200 °C of $SrCO_3$ and $(NH_4)_2HPO_4$ in the molar ratio of 3:2 for 12 h. Sr-substituted β-TCP samples with a Sr content of 10, 20, 40, 60 and 80 atom%, calculated as $[Sr^{2+}/(Ca^{2+} + Sr^{2+})] \cdot 100$, were prepared by heat treatment of appropriate stoichiometric mixture of β-TCP and α-$Sr_3(PO_4)_2$ at 1000 °C for 12 h. Samples were labeled 10SrTCP, 20SrTCP, 40SrTCP, 60SrTCP and 80SrTCP, respectively [Boanini, 2019].

4.2 Zinc β-TCP

The first step for the preparation of Zn-substituted β-TCP is the synthesis of α-$Zn_3(PO_4)_2$. α-$Zn_3(PO_4)_2$ was prepared by solid-state reaction at 800 °C of $(ZnCO_3)2[Zn(OH)_2]_3$ and $(NH_4)H_2PO_4$ in the molar ratio of 3:10 for 12 h. Zn-substituted β-TCP samples with a Zn content of 5, 10 and 15 atom% calculated as $[Zn^{2+}/(Ca^{2+} + Zn^{2+})] \cdot 100$, were prepared by heat treatment of appropriate stoichiometric mixture of β-TCP and α-$Zn_3(PO_4)_2$ at 1000 °C for 8 h. Samples were labeled 5ZnTCP, 10ZnTCP and 15ZnTCP, respectively [Boanini, 2019].

5. Gelatin films

Gelatin from pig skin (280 Bloom, Italgelatine SpA) was used: 5 g of gelatin were dissolved in 100 mL of solvent at 40 °C for about 30 min. Solvent could be:

- deionized water
- a mixture of water/ethanol (50/ 50)
- pure dimethyl sulfoxide (DMSO).

Films were obtained on the bottom of Petri dishes (diameter = 6 cm) from 7.4 mL of gelatin solution after solvent evaporation: water and water/ ethanol at room temperature, DMSO at 45 °C. Complete drying was attained under laminar flow hood.

5.1 Gelatin-quercetin films

Gelatin-quercetin films were obtained following the procedure reported in paragraph 5, and adding quercetin powder to gelatin before solvent addition. Different amounts of quercetin were used: 0.5, 1, 1.5 and 2 g/L. Samples prepared in water/ethanol and in DMSO were respectively labeled as W 05, W 1, W 15, W 2 and DMSO 05, DMSO 1, DMSO 15, DMSO 2. Similarly, reference samples with no quercetin were labeled W 0 and DMSO 0 [Rubini, 2020].

Since direct synthesis in water/ethanol (50/50) provoked precipitation of quercetin in solution, water/ethanol was used as a solvent following an adsorption procedure. In this case, films were obtained in water following the procedure reported in paragraph 5. Before complete drying, 7.4 mL of a solution of quercetin in water/ethanol (50/ 50) was placed into each Petri dish for 24 h. Afterwards films were washed with distilled water and completely dried under laminar flow hood. Different amounts of quercetin were used: 0.5, 1, 1.5 and 2 g/L. Therefore samples prepared by adsorption of quercetin were

respectively labeled as EtOH 05, EtOH 1, EtOH 15, EtOH 2, whereas reference sample with no quercetin was labeled EtOH 0.

5.2 Gelatin-curcumin films

Before complete drying of the gelatin films prepared as reported in paragraph 5 using water as a solvent, 7.4 mL of a solution of curcumin in water/ethanol (50/50) was placed into each Petri dish that was then sealed for 24 h. Afterwards, curcumin solution was removed, and films were washed with distilled water and completely dried under laminar flow hood. Different amounts of curcumin were used: 0.2, 0.5 and 1 g/L; and obtained films were respectively labeled as G-02, G-05, and G-1. Films without curcumin were prepared as control samples and labeled G-0 [Rubini, 2021].

Crosslinked films were prepared following the above procedure until the curcumin solution was removed. After washing each film with water, 7.4 mL of a phosphate buffer solution 0.1 M at pH 7.4 (PBS) containing glutaraldehyde (GTA) 0.15%wt was placed into each Petri dish. The reaction of glutaraldehyde with gelatin chains is reported here:

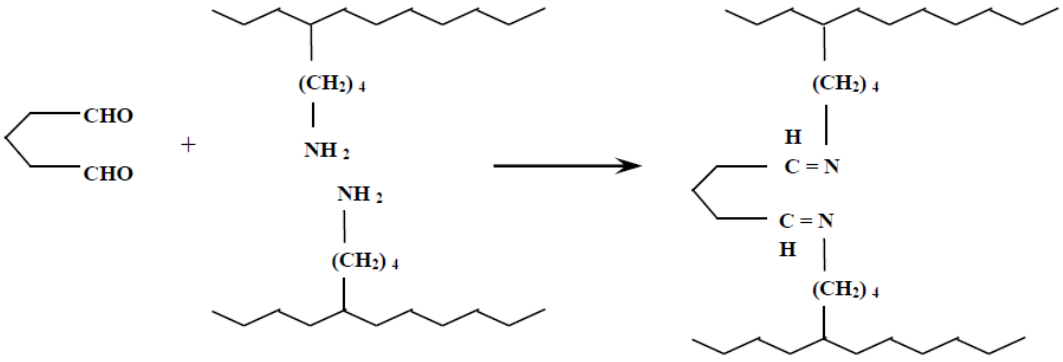

After 24 h the solution was removed and films in the dishes were repeatedly washed with glycine solution 1M. Complete drying was attained under laminar flow hood and obtained films were labeled as GTA-02, GTA-05 and GTA-1, as a function of the respective curcumin solution. Crosslinked films without curcumin were prepared as control samples and labeled GTA-0 [Rubini, 2021].

EXPERIMENTAL SECTION- *Preparation of Materials* -References.

- Boanini E, Gazzano M, Nervi C, Chierotti MR, Rubini K, Gobetto R, Bigi A. Strontium and zinc substitution in β-tricalcium phosphate: an X-ray diffraction, solid state NMR and ATR-FTIR study. J. Funct. Biomater. 2019;10:20
- Boanini E, Gazzano M, Rubini K, Mazzeo PP, Bigi A. Structural interplay between strontium and calcium in α-CaHPO4 and β-SrHPO4. Ceram. Int. 2021;47:24412–24420
- Boanini E, Torricelli P, Cassani MC, Rubini K, Fini M, Pagani S, Bigi A. Platinum nanoparticles supported on functionalized hydroxyapatite: anti-oxidant properties and bone cells response. Ceram. Int. 2020;46:19574–19582
- Cirillo M, Martelli G, Boanini E, Rubini K, Di Filippo M, Torricelli P, Pagani S, Fini M, Bigi A, Giacomini D. Strontium substituted hydroxyapatite with β-lactam integrin agonists to enhance mesenchymal cells adhesion and to promote bone regeneration. Colloids Surf. B: Biointerfaces 2021;200:111580
- Rubini K, Boanini E, Bigi A. Role of aspartic and polyaspartic acid on the synthesis and hydrolysis of brushite. J. Funct. Biomater. 2019;10:11
- Rubini K, Boanini E, Menichetti A, Bonvicini F, Gentilomi GA, Montalti M, Bigi A. Quercetin loaded gelatin films with modulated release and tailored anti-oxidant, mechanical and swelling properties. Food Hydrocoll. 2020;109: 106089
- Rubini K, Boanini E, Parmeggiani S, Bigi A. Curcumin-functionalized gelatin films: antioxidant materials with modulated physico-chemical properties. Polymers 2021;13:1824

Chapter 3

EXPERIMENTAL SECTION – *Characterization of Materials*

1. Powder X-ray diffraction

Powder X-ray diffraction analysis was carried out by means of a PANalytical X'Pert PRO powder diffractometer equipped with a fast X'Celerator detector (λ = 0.154 nm, 40 mA, 40 kV). For phase identification, the 2θ range was investigated from 5 to 60 2θ degrees with a step size of 0.1 and time/step of 100 s.

A further data collection between 10 and 120◦ was carried out to apply profile fitting procedure (step 0.033◦/100s). For monetite samples, HighScore Plus package version 4.9 by PANalytical was used for identification and Rietveld refinements. Coherent lengths of crystalline domains were measured by Scherrer equation. For β-TCP samples, MAUD program (Material Analysis Using Diffraction) [Lutterotti, 2010] was used for structural refinements employing scattering factors for Ca^{2+}, Sr^{2+}, Zn^{2+} ions, as well as for phosphorus atom.

Data collection for structure solution from a powder sample of β-$SrHPO_4$ was performed in Bragg-Brentano geometry with CuKα radiation on a Rigaku SmartLab XE diffractometer equipped with a Hypix3000 2D Solid-State detector. Vertical variable slits program coupled with 2.5◦ soller slits were used to minimize peak asymmetry and intensity aberration at low angles. XRPD data were postprocessed and CuKα2 contribution was stripped using the proprietary Rigaku SmartLab Studio II software.

1.1 Rietveld refinement

In the Rietveld refimement the experimental pattern is calculated through a mathematical function, since the relation between the atom position and the intensity at each point of the powder profile are known [Young, 1993]. The pattern is reproduced by assuming it to be a sum of a number of well shaped Bragg reflections centered in their respective Bragg angle positions. A structural model is necessary in order to calculate the corresponding intensity at each $y_{i\ calc}$ step of the pattern, according to the equation (1):

$$y_{\,i\,calc}(k) = s \sum_{k} m_{\,k} L_{\,k} [F_{\,k}]^{\,2} G\,(2\theta_i - 2\theta_k) P_{\,k} A_{\,k} + y_{\,ib} \qquad (1)$$

where s is the scale factor, m is multiplicity factor, L is the Lorenz-polarization factor for the k reflection, F is the structure factor, G the reflection profile function, 2θ is the calculated position of the Bragg peak, P is the preferred orientation factor, A is the adsorption factor, y_{ib} is the background value at point i.

The purpose of this procedure is to find the best possible agreement between the observed pattern and a calculated profile. In order to get this goal the residual S:

$$S = \sum_i w_i [(y_{i\,obs} - y_{i\,calc})]^2 \qquad (2)$$

where $w_i = 1/y_{iobs}$, y_{iobs} is the observed intensity at the i-th step and $y_{i\ calc}$ is the calculated intensity at i-th step, must reach a minimum value.

During this procedure two sets of parameters are varied:

- *non structural parameters*, generally refined at the beginning of the procedure (scale factor, zero shift, background parameters, profile shape, asymmetry).
- *structural parameters*, refined in the last steps of the procedure (unit cell parameters, atom position, occupation factor)

This order could however change according to the observed results on the calculated pattern after each step.

In this thesis, substituting atoms (Sr or Zn) were placed in the same position as calcium in the calcium phosphate structure of interest with the constraint that the total occupancy factors of Ca and substituting atoms at the same site must be equal to unit.

1.2 Scherrer analysis

For monetite samples, the line broadening of the 001, 0-11 and 1-20 reflections was used to evaluate the length of the coherent domains (hkl).

$\tau_{h\,k\,l}$ values were calculated from the widths at half maximum intensity ($\beta_{1/2}$) using the Scherrer equation

$$\tau_{hkl} = \frac{k * \lambda}{\beta_{\frac{1}{2}} * cos\theta}$$

where λ is the wavelength, θ the diffraction angle and K a constant depending on crystal habit. The silicon standard peak 111 was used to evaluate the instrumental broadening.

1.3 Structure solution

In this thesis work, the structure of β-$SrHPO_4$ has been solved. Data were postprocessed and CuKα2 contribution was stripped using the proprietary Rigaku SmartLab Studio II software. Powder pattern was indexed with EXPO2014 [Altomare, 2013] while the crystal structure of β-SrHPO4 was solved from Powder Diffraction Data using TOPAS v6 [Coelho, 2018]. Asymmetric Unit was refined with a rigid body constrain. Interatomic distances and angles limits were restrained according to the statistical analysis performed on the CSD database. Rietveld Refinement was performed over the whole powder pattern.

2. Fourier Transform Infra-Red Spectroscopy

For FT-IR adsorption analysis, about 1 mg of the powdered samples was carefully mixed with KBr (200 mg, infrared grade) and pelletized under a pressure of 10 tons for 2 min. The pellets were analyzed using a Bruker ALPHA FT-IR spectrophotometer to collect 32 scans in the range 4000–400 cm^{-1} at a resolution of 4 cm^{-1}.

FTIR spectra in Attenuated Total Reflection mode were collected with Alpha FT IR Bruker spectrometer with ATR diamond module at single reflection, with a resolution of 4 cm^{-1} and 32 scans in the scan range 4000–450 cm^{-1}. The background spectrum was collected before the acquisition of each sample spectrum. Data analysis was operated with OPUS software.

3. Solid state Nuclear Magnetic Resonance

Solid-state NMR spectra of β-TCP samples were acquired with a Jeol ECZR 600 instrument, operating at 242.95 MHz for the ^{31}P nucleus. Powder samples were packed into cylindrical zirconia rotors with a 3.2 mm o.d. and a 60 μL volume and spun at 20 kHz. A certain amount of sample was collected and used without further preparations from all samples to fill the rotor. ^{31}P MAS spectra were acquired at room temperature for all samples. The spectra were collected using a direct excitation pulse sequence with a 90° ^{31}P pulse of 1.3 μs, an optimized recycle delay of 1800 s and a number of scans between 4–8, depending on the sample. The ^{31}P chemical shift scale was calibrated through a 85% H_3PO_4 solution as external standard.

4. Elemental Analyses

4.1 Atomic absorption spectroscopy (AAS)

The amount of platinum present on the different apatitic samples was determined by flame atomic absorption spectroscopy (AAS, THERMO iCE 3000 Series) in air-acetylene flame with a wavelength of 266.0 nm. For this analysis ca. 5 mg of sample were dissolved in 25 ml of a 0.5 M HNO_3 (NORMATOM®) aqueous solution adding, when necessary, small amounts of aqua regia until complete dissolution. The calibration line was made with 5 calibration standards (2, 4, 6, 8, 10 ppm) prepared by dilution with 0.5 M HNO_3 of a platinum standard for AAS (TraceCERT®, Merck, 1000 ± 4 ppm Pt in 5% HCl). Results from this analysis represent the mean value of three different determinations.

4.2 Ion cromatography

Ca and Sr contents in Sr-substituted phosphates were monitored by ion cromatography (Dionex ICS-90). The calibration line was made with 5 calibration standards (1, 5, 10, 30, 50 ppm) prepared using multi-standard solutions containing Ca and Sr standard for AAS. Results from this analysis represent the mean value of three different determinations.

Powders were previously dissolved in 0.1 M HCl prepared with MilliQ water.

4.3 Analysis of light elements

Elemental analysis of light elements was performed on a Thermo Flash 2000 CHNS/O Analyzer (Thermo Fisher). Each sample was weighed in tin capsules, then dropped into an oxidation/reduction reactor kept at a temperature of 900–1000 °C. Produced gases were separated in a chromatographic column and detected by a highly sensitive Thermo Fisher thermal conductivity detector.

5. Thermal Analyses

5.1 Thermogravimetric Analysis

Thermogravimetric analysis was carried out using a Perkin- Elmer TGA-7. Heating was performed in a platinum crucible in air flow (20 cm^3/min) at a rate of 10 °C/min up to 900 °C. The samples weights were in the range 5–10 mg. Results from this analysis

represent the mean value of determinations for three different samples of each composition.

5.2 Differentaial Scanning Calorimetry

Calorimetric measurements (DSC) were performed using a Perkin Elmer Pyris Diamond differential scanning calorimeter equipped with a model ULSP 90 intra-cooler Heating was carried out in aluminum open pan at 5 ◦C min^{-1} in the temperature range from 50 °C to 215 °C.

6. Electron Microscopy

6.1 Scanning electron microscopy

Morphological investigation was performed by scanning electron microscopy (SEM) using a Philips XL20 instrument operating at 15 kV. The samples were sputter-coated with Au before analyses. Monetite samples obtained after thermal treatment (TT-series samples) were observed using a Zeiss Leo-1530 high-resolution scanning electron microscope operating at 1 kV (InLens detector) and no sample coating was performed.

6.2 Transmission electron microscopy

For TEM investigations, a drop of sonicated powder suspension in ethanol was transferred onto holey carbon foils supported on conventional copper microgrids. A Philips CM100 transmission electron microscope, operating at 80 kV was used.

6.3 *Fluorescence microscopy*

Transmission and fluorescence images of gelatin films were obtained by a fluorescence microscope (Olympus IX71) with a 10x objective. In order to collect the fluorescence images, excitation was performed at 378–400 nm and the fluorescence was observed at 510–542 nm.

7. Surface Area Analysis

Specific surface area was measured by gas adsorption following the Brunauer-Emmett-Teller (BET) method. A Carlo Erba Sorpty 1750 BET analyzer was used working with a constant volume N_2 absorption with desorption at 80 °C.

8. Zeta Potential Measurement

Zeta potential was measured using a Malvern Instruments Zetasizer Nano. 5 mg of powder sample was suspended in 50 mL of MilliQ water after sonication for 2 minutes. Each analysis was performed in triplicate.

9. Uv-Vis Spectroscopy

9.1 Release of β-Lactams

The in vitro release profiles of β-lactams **1** and **2** from the corresponding SrHA samples were evaluated at 37 ◦C in triplicate by HPLC-UV analysis, using linear calibration curves obtained at λ=254 nm. Data were reported as mean values ± standard deviations. Release studies were performed on samples with a compound loading of 12.9 and 6.2 wt % for SrHA**1**, and of 8.4 and 4.2 wt% for SrHA**2**. Two aqueous solutions were analysed: a saline solution and a phosphate buffered solution at pH = 7.4 as models for physiological conditions. Measurement were performed at selected times on the supernatant, which was separated and substituted with fresh solution (refresh).

9.2 Quercetin content and release

Quercetin content was determined on samples dissolved in H2O/ EtOH 1:1 solution at a concentration of 20 mg/mL and maintained at 40 °C for one day. Absorption spectra of each series of films were collected on 1:50 diluted film solutions (0.4 mg/mL). Quercetin release was determined on samples (1cm x1cm) placed at the bottom of a vial and added with 5 mL of PBS 0.1M (pH 7.4). The release was monitored for 10 h at room temperature, collecting absorption spectra on supernatant diluted 1:1 with Ethanol. The spectra were recorded at selected times and the PBS solution was refreshed after each absorbance measurement. Absorption spectra were collected with a PerkinElmer UV/Vis spectrometer Lambda 45. Quercetin content of the films, as well as quercetin release, was obtained by means of Lambert-Beer law:

$$Abs = \varepsilon\, b\, c$$

where *Abs* is the Absorbance, ε [$M^{-1}cm^{-1}$] is the extinction molar coefficient, *b* [cm] is the optical path (1 cm) and *c* [M] is the concentration of quercetin. For the evaluation of quercetin content, the molar extinction coefficient (15360 $M^{-1}cm^{-1}$) was calculated by

collecting absorption spectra of known quantities of quercetin dissolved in a water/ethanol 1:1 mixture containing gelatin (0.4 mg/mL). For the evaluation of quercetin release, the molar extinction coefficient (14234 $M^{-1}cm^{-1}$) was calculated by collecting absorption spectra of known quantities of quercetin dissolved in a PBS 0.1M/ethanol 1:1 mixture.

9.3 Curcumin content and release

Absorption spectra were collected with a Varian Cary50Bio instrument (λ = 430 nm). Each analysis was performed in triplicate.

For determination of curcumin content, about 100 mg of film was dissolved in 100 mL H_2O/EtOH 1:1. Curcumin release was determined on weighted G or GTA samples (1 cm x1 cm) placed at the bottom of a vial and added with 5 mL of PBS 0.1M (pH 7.4) or physiological solution (NaCl 0.9%) or H_2O/EtOH 1:1. Each experiment was performed in triplicate. The release was monitored up to 48 h at room temperature, collecting absorption spectra on supernatant. The spectra were recorded at selected times and the solution was refreshed after each absorbance measurement.

10. Swelling tests

For swelling experiments, gelatin films were cut into portion 1 cm x 1 cm and were weighted in air-dried conditions. Then they were immersed in phosphate-buffered saline (PBS, 0.1 M) solution for different periods of time. Wet samples were wiped with filter paper to remove excess liquid and weighed. The amount of absorbed water was calculated as

$$W(\%) = [(Ww-Wd)/Wd]\cdot 100$$

where *Ww* and *Wd* are the weights of the wet and the air-dried samples.

11. Water solubility

Water solubility of gelatin films was determined in triplicate [Gimenez, 2009]. Portions of the films (2 x 2 cm) were placed into glass containers with 15 mL of distilled water and subjected to gentle shaking at 65 rpm for 15 h at 22 °C. Filtration on filter paper was used to recover the remainder of the undissolved film, which was desiccated at 105 °C for 24 h. The film solubility was calculated as

$$FS\ (\%) = [(W0-Wf)/W0]\cdot 100$$

where *W0* is the initial weight of the film expressed as dry matter and *Wf* is the weight of the desiccated undissolved rest of the film.

12. Static contact angle

Static contact angle measurements were performed on gelatin films using a KSV CAM-101 instrument under ambient conditions The side profiles of deionized water drops were recorded for image analysis in a time range of 0–10 s, by collecting an image every 0.5 s. At least three drops were observed for each sample.

13. Mechanical tests

For mechanical tests, wet gelatin films were cut into stripes (3 mm X 30 mm). Film stripes containing quercetin and prepared by direct synthesis in DMSO or by adsorption from water/ethanol were immersed into a mixture of water/ethanol (in the ratio 2:3) for 1 min or 72 h respectively; whereas film stripes containing curcumin were immersed into PBS 0.1 M pH 7.4 for 1 min. Afterwards, the stripes thickness was carefully measured for each stripe (values around 0.12 mm) using a Leitz SMLUX- POL microscope.

Stress–strain curves of strip-shaped films were recorded using an INSTRON Testing Machine 4465 with a crosshead speed of 5 mm min^{-1} and the Series IX software package. The Young's modulus E, the stress at break σ_b and the strain at break ε_b of the strips were measured. Statistical analysis was performed with the Student *t*-test considering a *p* value of less than 0.05 to be significantly different.

14. Assays for scavenging activities

14.1 Radical scavenging activity

Antioxidant activity was determined on the basis of quercetin and curcumin ability to act as radical scavengers toward the 2,2-diphenyl-1-picrylhydrazyl free radical, (DPPH·) [Gülçin, 2006; Berlier, 2013; Ak, 2008]. Solutions of gelatin films containing quercetin or curcumin were prepared by dissolving the solid samples in MilliQ water/EtOH and thereafter they were diluted, based on their known quercetin or curcumin contents, in order to get 10 µM, 30 µM and 50 µM of quercetin or curcumin concentrations.

Dilutions of pure quercetin or curcumin, 10 μM, 30 μM and μM, were prepared and used as reference samples.

For the assay of quercetin activity, 50 μL of each solution (samples and references) were added to 3 mL of DPPH· saturated ethanol/water (20/80 V/V) solution, previously clarified by centrifugation (10000 rpm for 10 min). For the assay of curcumin activity, 6 mL of each solution (samples and references) were added to 0.2 mL of 1mM DPPH· solution in ethanol, previously clarified by centrifugation (10000 rpm for 10 min).

After an incubation for 30 min at room temperature in darkness, absorbance values (A) were spectrophotometrically measured at 517 nm.

The radical scavenging activity (RSA) was determined through the following equation:

$$\% \text{ RSA} = (A0 - Ax)/A0 \times 100$$

where A0 is the absorbance of the control (containing DPPH• solution without quercetin or curcumin), and Ax is the absorbance in the presence of quercetin or curcumin (as reference) or of quercetin-containing or curcumin-containing samples.

Statistical evaluation of data was performed using GraphPad Prism version 5.00 for Windows (GraphPad Software). One-way analysis of variance (ANOVA) followed by Dunnett's Multiple comparison test was used to determine significance of differences ($p < 0.05$) among experimental groups and reference samples.

14.2 Hydrogen peroxide scavenging activity

The hydrogen peroxide scavenging activity of HAPEI-PtR, HAPEI PtTT and HAPEI for comparison was determined with the Pierce™ Quantitative Peroxide Assay Kit (Thermo Scientific). Peroxide standards were obtained after serially diluting a 30% (8.8 M) hydrogen peroxide stock solution to achieve 8 standards in the concentration range of 7.8–1000 μM. Tests were performed on disk-shaped samples (Ø = 6.0 mm), prepared by pressing 40 mg of powder into cylindrical moulds by using a standard evacuable pellet die (Specac) at 10 tons. Each disk was immersed in 125 μM H_2O_2 at 37 °C. The pH value was kept constant at 7.4 with 0.15 M phosphate buffered saline (PBS). A 20 μL aliquot was taken from the reaction solution after 30 min, 1, 2, 3, 4, 5, 6 and 7 h and its residual H2O2 was determined with the addition of 200 μL Assay Kit working reagent in microplate wells. Absorbance was measured at 550 nm using a plate reader.

References.

- Ak T, Gülçin I. Antioxidant and radical scavenging properties of curcumin. Chem. Biol. Interact. 2008;174:27–37
- Altomare A, Cuocci C, Giacovazzo C, Moliterni A, Rizzi R, Corriero N, Falcicchio A. EXPO2013: A kit of tools for phasing crystal structures from powder data. J. Appl. Crystallogr. 2013;46:1231–1235
- Berlier G, Gastaldi L, Ugazio E, Miletto I, Iliade P, Sapino S. Stabilization ofquercetin flavonoid in MCM-41 mesoporous silica: positive effect of surface functionalization. J. Colloid Interface Sci. 2013;393:109–118
- Coelho AA. TOPAS and TOPAS-Academic: an optimization program integrating computer algebra and crystallographic objects written in C++. J. Appl. Crystallogr. 2018;51:210–218
- Giménez B, Gómez-Estaca J, Alemán A, Gómez-Guillén MC, Montero MP. Physico-chemical and film forming properties of giant squid (Dosidicus gigas) gelatin. Food Hydrocoll. 2009;23:585-592
- Gülçin I. Antioxidant and antiradical activities of l-carnitine. Life Sci. 2006;78:803–811
- Lutterotti L. Total pattern fitting for the combined size-strain-stress-texture determination in thin film diffraction. Nucl. Instrum. Meth. B 2010;268:334–340
- Young RA. The Rietveld Method; Oxford University Press: Oxford, UK, 1993

Chapter 4
RESULTS AND DISCUSSION

1. Functionalization of calcium phosphates.

Due to the complexity of the events involved in bone formation, which include hierarchical structuring, adaptive growth and constant remodeling, the reproduction of the whole biomineral assembly mechanism by non-biological methods is not an affordable goal. A more realistic approach is to devolp bioinspired processes for obtaining tailored functions using simple starting materials [Bigi, 2017]. In this light, the bioactivity of calcium phosphates can be improved through functionalization with biologically active ions, molecules and metallic nanoparticles, in the meanwhile preserving the biocompatibility of the supporting material as well as its similarity with biological apatites.

1.1 Hydroxyapatite crystals enriched with platinum nanoparticles.

Platinum compounds, such as cisplatin and related platinum-based drugs are a well-known chemotherapeutic agents. They have been used for treatment of numerous human cancers including carcinomas, germcell tumors, lymphomas, and sarcomas [Dasari, 2014]. Moreover, platinum nanoparticles (PtNPs) have been reported to be useful in a variety of pathologies, including pulmonary inflammation, cancer and vascular diseases [Mohammadi, 2013; Puja, 2019]. They can also quench hydrogen peroxide and superoxide, exhibiting a behavior similar to that ofcatalase and superoxide dismutase enzymes, and reduce cellular oxidative stress [Zhang, 2010; Hosaka, 2014].
In this thesis work, HA and HAPEI crystals have been used as supporting materials. The synthesis of hydroxyapatite in the presence of 4 M PEI produces a single crystalline phase (HAPEI) which exhibits a powder XRD pattern close to that of pure HA (PDF n. 9–432), showing that the presence of polyelectrolyte does not induce any significant modification in the crystalline structure (Figure 4.1).

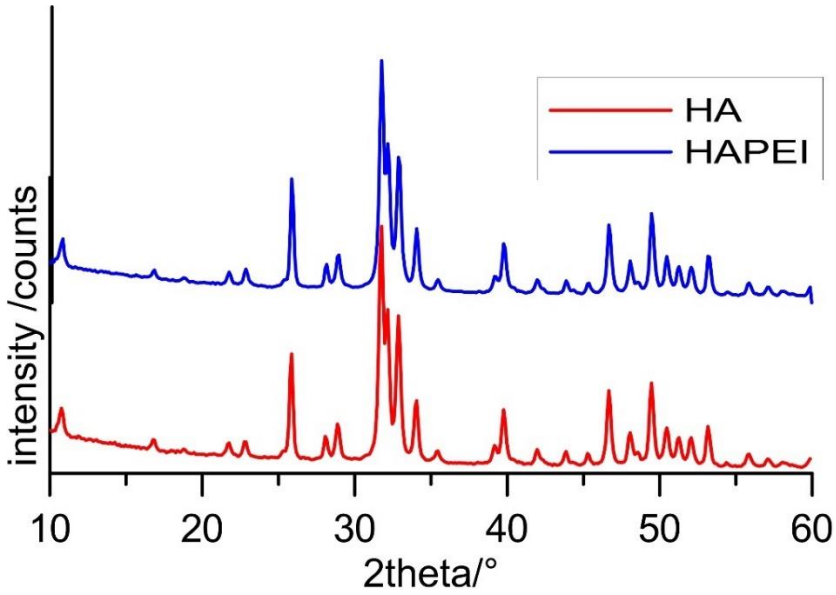

Figure 4.1 – XRD patterns of HA and HAPEI

Polyelectrolyte content in HAPEI can be determined by comparing its thermogravimetric (TG) plot with that of pure HA: the different weight losses of the two compounds up to about 600 °C (Figure 4.2) can be ascribed to the presence of PEI, which amounts to about 5.2 wt%.

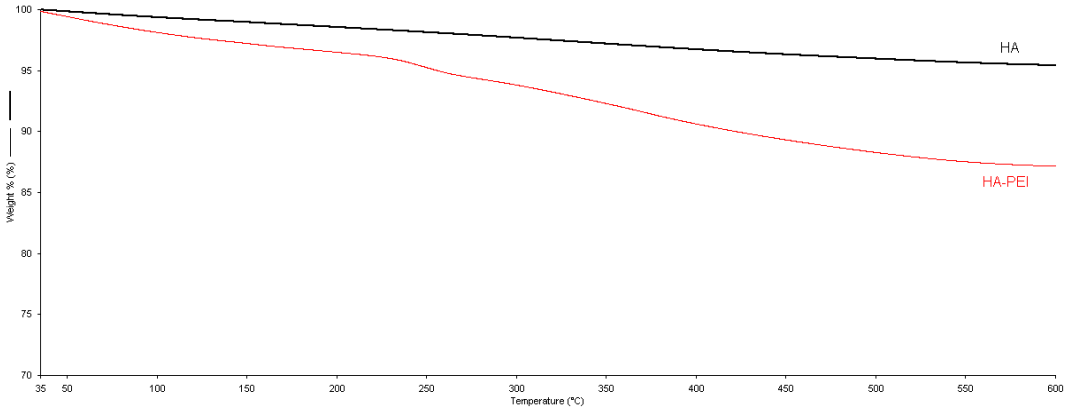

Figure 4.2 – TGA plots of HA and HAPEI

For the functionalization of HA and HAPEI crystals, a step-by-step process has been developed: the initial loading of Pt(II) ions can be followed by a reduction reaction that gives rise to the formation of supported PtNPs, as described in Chapter 2 - Experimental Section – Preparation of Materials – par. 1.2, and schematized in Figure 4.3.

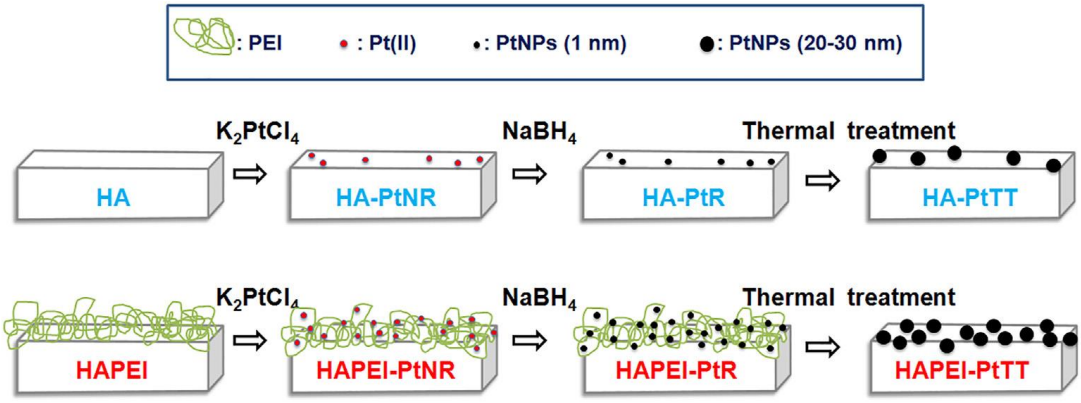

Figure 4.3 - Scheme of synthetic procedure for the loading of Pt(II) ions and subsequent formation of supported PtNPs [*reproduced from Boanini, et al., 2020*]

The results of AAS elemental analyses indicate that the amount of Pt adsorbed onto HA and HAPEI are 0.7 wt% and 2.2 wt%, respectively, with no significant differences before and after reduction. HA and HAPEI display similar specific surface areas: 23 and 26 m^2/g respectively. Therefore the greater amount of Pt(II) or PtNPs loaded on HAPEI in comparison to HA, must be attributed to the presence of the polyelectrolyte, which promotes interactions with the metallic ion [Rivas, 2005].

The presence of PtNPs on the two different supports can be also appreciated in the TEM images recorded after platinum reduction. The images show that the number of PtNPs on HA-PtR is much less than those on HAPEI-PtR, confirming the results of chemical analysis (Figure 4.4). In both cases, PtNPs display nanometric dimensions, around 1 nm.

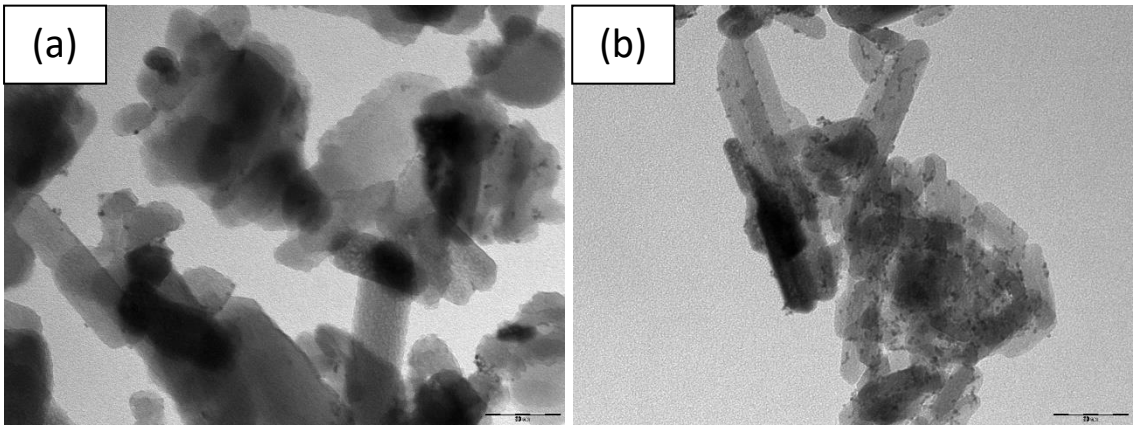

Figure 4.4 – TEM images of (a) HA-PtR and (b) HAPEI-PtR.

As expected, the XRD patterns of HA-PtNR and HAPEI-PtNR display no differences in comparison to the patterns recorded before platinum loading (Figure 4.5a). Differently, in XRD patterns of HA-PtR and even more of HAPEI-PtR, it is possible to appreciate a diffuse halo centered around 40°/2θ, that indicates the presence of PtNPs bearing extremely small dimensions (Figure 4.5b).

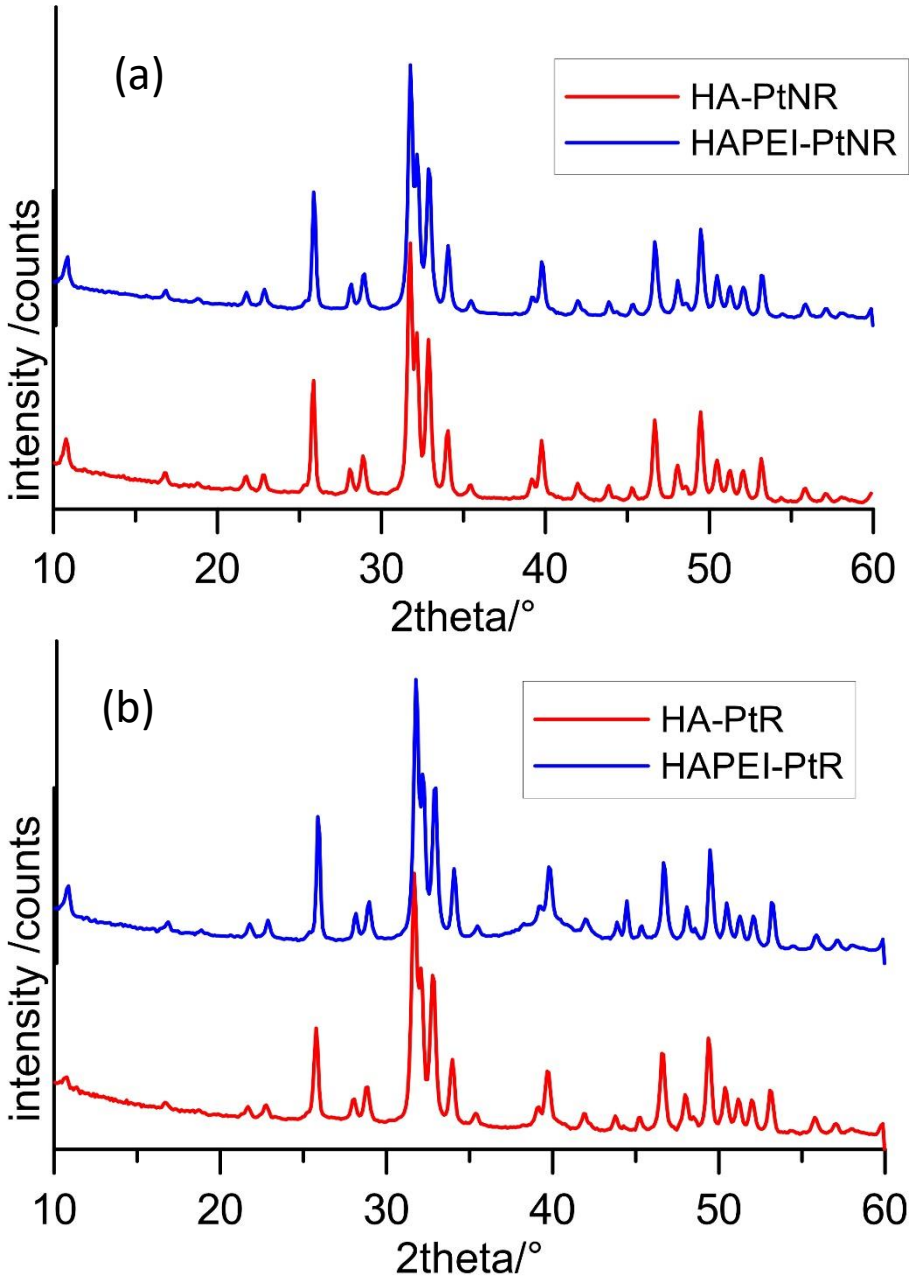

Figure 4.5 – XRD patterns of (a) HA-PtNR and HAPEI-PtNR; and (b) HA-PtR and HAPEI-PtR

A comparison and magnification of the XRD patterns in the relevant range of 2θ allows enhancing these differences (Figure 4.6).

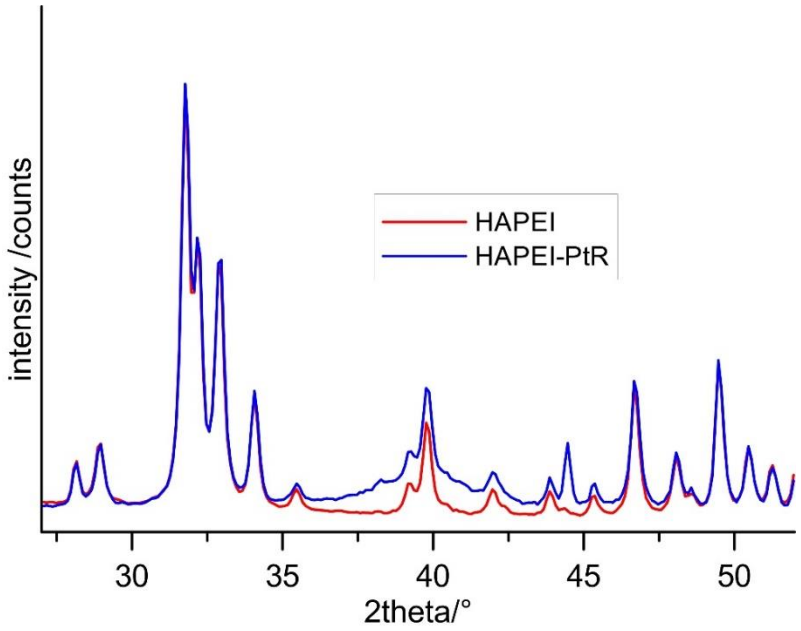

Figure 4.6 - Magnification of the XRD patterns of HAPEI and HAPEI-PtR

Heat treatment of HA-PtR and HAPEI-PtR samples at 700 °C induces complete removal of PEI and aggregation of PtNPs into significantly bigger particles, with dimensions, up to about 20–30 nm (Figure 4.7a). These dimensions increase the sharpness of the relevant XRD peaks due to metallic platinum, allowing its presence identification: indeed, the XRD pattern of HAPEI-PtTT (Figure 4.7b) displays the typical reflections of HA (PDF n. 9–432) together with a peak at about 40°/2θ and a shoulder at about 46°/2θ, characteristic of Pt (PDF n. 01-087-0646).

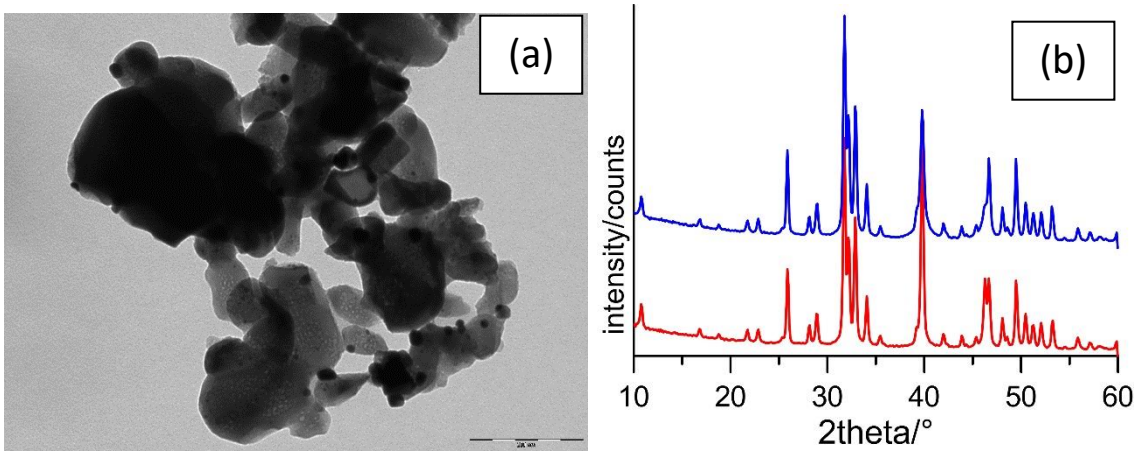

Figure 4.7 – (a) TEM and (b) XRD results of samples after heat treatment

PtNPs are known to display anti-oxidant properties [Zhang, 2010]. The results of the quenching activity against hydrogen peroxide of the materials prepared in this work indicate that the nanoparticles maintain their anti oxidant power when supported on apatitic crystals (Figure 4.8a). At variance with HAPEI, which causes elimination of only about 10% of hydrogen peroxide after 7 h (Figure 4.8b), both HAPEI-PtR and HAPEI-PtTT can eliminate about 20% of H_2O_2 in just 30 min, and approximately 100% of H_2O_2 in 7 hours, indicating that both materials possess a high activity for scavenging hydrogen peroxide.

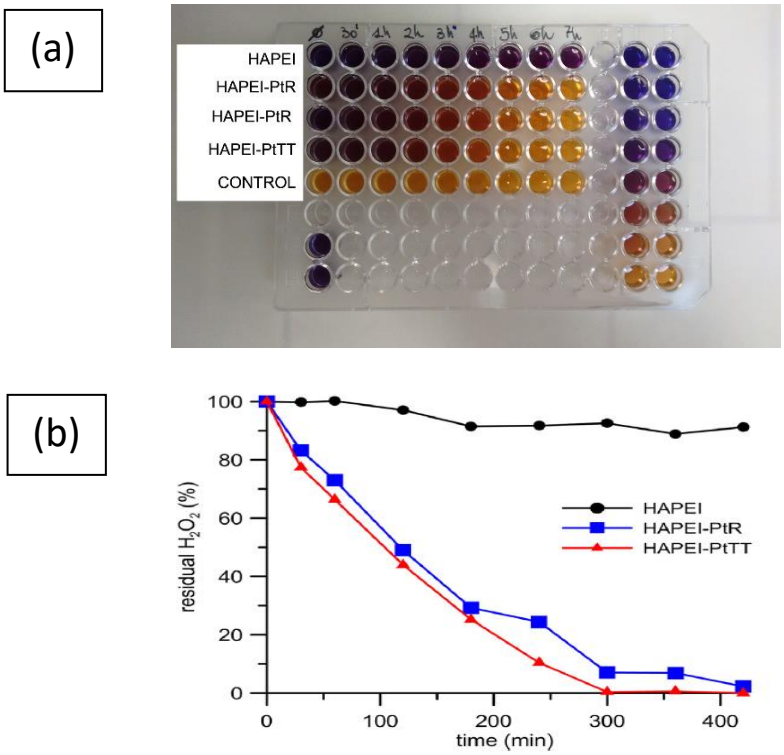

Figure 4.8 - The hydrogen peroxide scavenging activity of HAPEI, HAPEI-PtR, and HAPEI-PtTT (a) Absorbance measures at 550 nm using a plate reader. Peroxide standards (for calibration curve) are on the right of the plate; (b) Activities of HAPEI, HAPEI-PtR and HAPEI-PtTT for the H_2O_2 decomposition in time [*reproduced from Boanini, et al., 2020*].

In conclusion, in this work platinum nanoparticles have been successfully supported on apatitic crystals. In particular, functionalization of hydroxyapatite nanocrystals with PEI has been shown to enhance PtNPs loading thanks to the polyelectrolyte interaction with the metallic ion, Pt(II). Chemical reduction results in the formation of nanometric PtNPs, whose dimensions on the apatitic supports significantly increase from ca. 1 nm to 20–30 nm after heat treatment. However, the good anti-oxidant properties of these

composite materials are independent from metallic nanoparticles size, as shown by the similar values of H_2O_2 decomposing activity [Boanini, 2020].

1.2 Strontium substituted hydroxyapatite functionalized with β-lactams.

To improve bone regeneration, the efficacy of cell adhesion and differentiation should be enhanced, and in this aspect, integrins could represent an important cellular target [Wei, 2015]. Previous studies provided a series of new β-lactam-based molecules able to modulate cell adhesion on targeting different integrins, mainly leukocyte- and RGD-binding integrins [Galletti, 2014]. Some of the molecules acted as agonists, promoting cell adhesion and activation of intracellular signalling, others resulted antagonists inhibiting integrin-dependent processes.

Functionalization of hydroxyapatite with β-lactam agonists could produce new functional materials with a cell-targeted specificity because of their integrin selectivity. In this work, strontium substituted hydroxyapatite (SrHA) was loaded with two monocyclic β-lactams **1** and **2** (Figure 2.1) selected on the basis of their activities in cell adhesion tests [Martelli, 2020], with the aim to get multifunctionalized materials able to couple the promotion of cell adhesion and activation of intracellular signalling by β-lactam integrin agonists with the beneficial influence of strontium ion on osteointegration and bone regeneration. Indeed strontium is provoking an increasing interest because of its beneficial effect on bone formation, and prevention of bone resorption.

The XRD pattern of the synthesized SrHA showed the characteristic peaks of hydroxyapatite shifted towards smaller angles (Figure 4.9a). In agreement, the values of the calculated lattice parameters (a = 9.453(3) Å, c = 6.903(4) Å) are enlarged in comparison to those characteristic of pure HA (PDF: 9–432) coherently with a partial substitution of the bigger Sr ion to Ca ion into the hydroxyapatite structure. The elemental analysis of SrHA nanocrystals resulted in about 7.5 ± 0.2 at% of strontium content calculated with respect to total cations. Morphological analysis showed the typical platelet-like shape of apatitic crystals with mean dimensions of about 150 nm x 30 nm (Figure 4.9b).

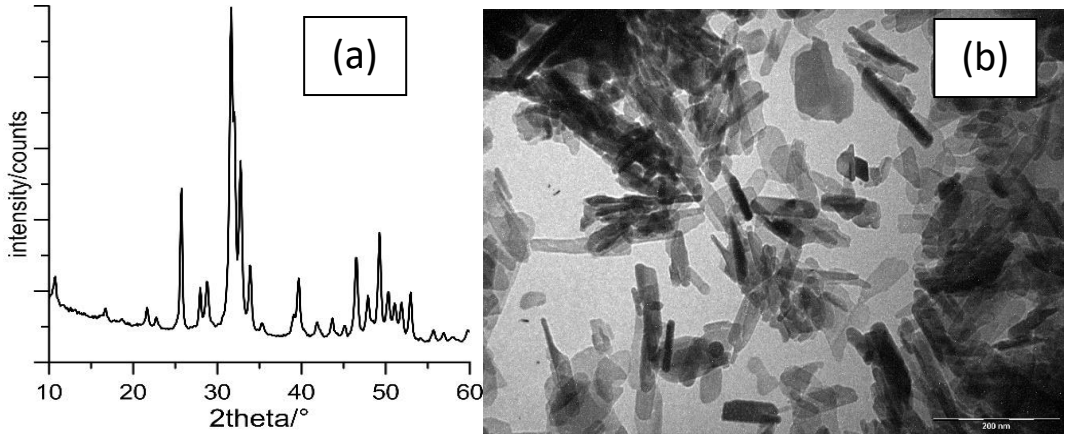

Figure 4.9 – XRD pattern (a) and TEM image (b) of SrHA crystals.

The loading of β-lactams **1** and **2** on SrHA nanocrystals was screened in H_2O or H_2O/acetonitrile mixtures to evaluate the medium effect on the loading (Table 2.1). The influence of the compound concentration and on the polar character of the loading solution [Snyder, 1974] was also explored (Table 4.1).

Table 4.1 – Polarity index of solvents mixtures calculated from the Snyder polarity indexes of H_2O and acetonitrile and the loaded amount of compounds evaluated by TGA analysis.

Experiment #	***1***	***2***	***3***	***4***	***5***	***6***	***7***	***8***	***9***	***10***	***11***	***12***	***13***	***14***
Polarity index	5.8	6.9	8	8	8	8	9.1	9.8	6.5	6.5	6.5	8	8.7	10.2
Loading (wt%)	9.0	5.3	9.6	24.0	6.2	3.5	12.9	14.4	8.4	4.4	8.1	4.5	3.2	4.2

When the loading was carried out in acetonitrile, a good uptake from the solution was observed (9 wt%, Table 4.1 entry 1); on the contrary the loading in water was hindered by the insolubility of **1**. The polarity of the medium was varied through variation of the composition of the H_2O/acetonitrile mixtures at constant concentration (0.063 M). The loading amount of compound **1** increased as the polarity raised (Table 4.1 entries 2, 3, 7 and 8), from 5.3 wt% in H_2O/CH_3CN = 1:3 (PI = 6.9) to 14.4 wt% in H_2O/ CH_3CN = 10:1 (PI = 9.8). This behaviour could be explained considering that the molecule **1** is quite apolar with high affinity to acetonitrile, so that the adsorption of compound **1** on SrHA was more favoured from a water enriched solution. Compound **1** is hydrophobic and its solvation in acetonitrile is destabilized by an increase of water amount in the loading solution, which promotes its adsorption on SrHA. Moreover, in H_2O/CH_3CN 1:1 mixture the loaded wt% of **1** is proportional to the β-lactam concentration, resulting

higher on increasing the amount of the compound in the starting solution (Table 4.1 entries 3–6). In particular, charging 20 mg of **1** per 0.6 mL of the 1:1 solvent mixture gave the highest loading amount, 24 wt% (Table 4.1 entry 4). Conversely, SrHA**2** composites settled around a medium-low loading (3.2–8.4 %) that decreased on increasing the solvent polarity (Table 4.1 entries 9, 12, and 13). To notice, the lowest value of loaded β-lactam (3.2 wt% Table 4.1 entry 13) arose from a half content of β-lactam **2** in an enriched water solution, balanced by a prolonged loading time (overnight). Compound **2** is more polar and hydrophilic than **1**, and hence it tends to be better distributed in solutions at higher water content than to be adsorbed on SrHA. Neither tripling concentration (Table 4.1, entry 11), nor increasing of the loading temperature (70 °C, Table 4.1, entry 10) enhanced loading. The absorption in H_2O alone gave a loading of 4.2 % (Table 4.1, entry 14), even if conducted overnight, whereas the experiment in acetonitrile alone was not feasible due to the insolubility of **2** in this solvent.

The absorption on SrHA of the two β-lactam was dictated by their partition between the solid phase and the loading solution: SrHA competes with the solvent for the recruitment of β-lactam compounds, which in turn depends on the polarity of the compound and of the loading solution [Cirillo, 2021].

The amount of β-lactams loaded on SrHA was evaluated through TGA analysis, by measuring the different weigth loss of loaded samples in comparison with pure SrHA (Figure 4.10 and Table 4.1).

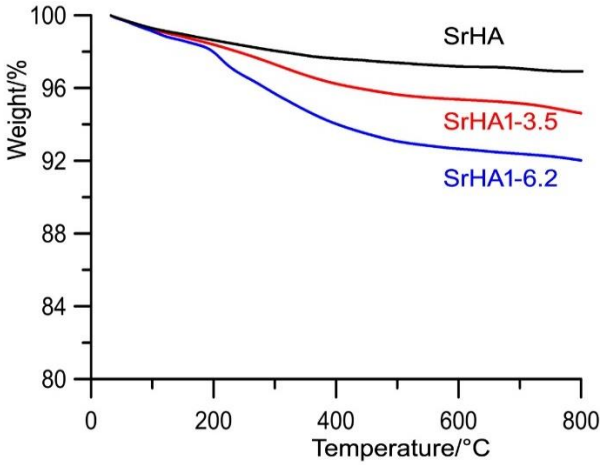

Figure 4.10 - TGA plots of SrHA and some functionalized samples, which allow to determine the amount (wt%) of β-lactam loaded on SrHA [*reproduced from Cirillo, et al., 2021*].

FTIR-ATR was used to explore the chemical interactions between β-lactams **1**-**2** and hydroxyapatite. Spectra of the composites display the O–H stretching and bending modes of hydroxyapatite at 3572 and 630 cm^{-1} respectively, the strong bands due to phosphate absorption at 550–630 and 900-1100 cm^{-1}, as well as the bands of the β-lactam compounds (Figure 4.11).

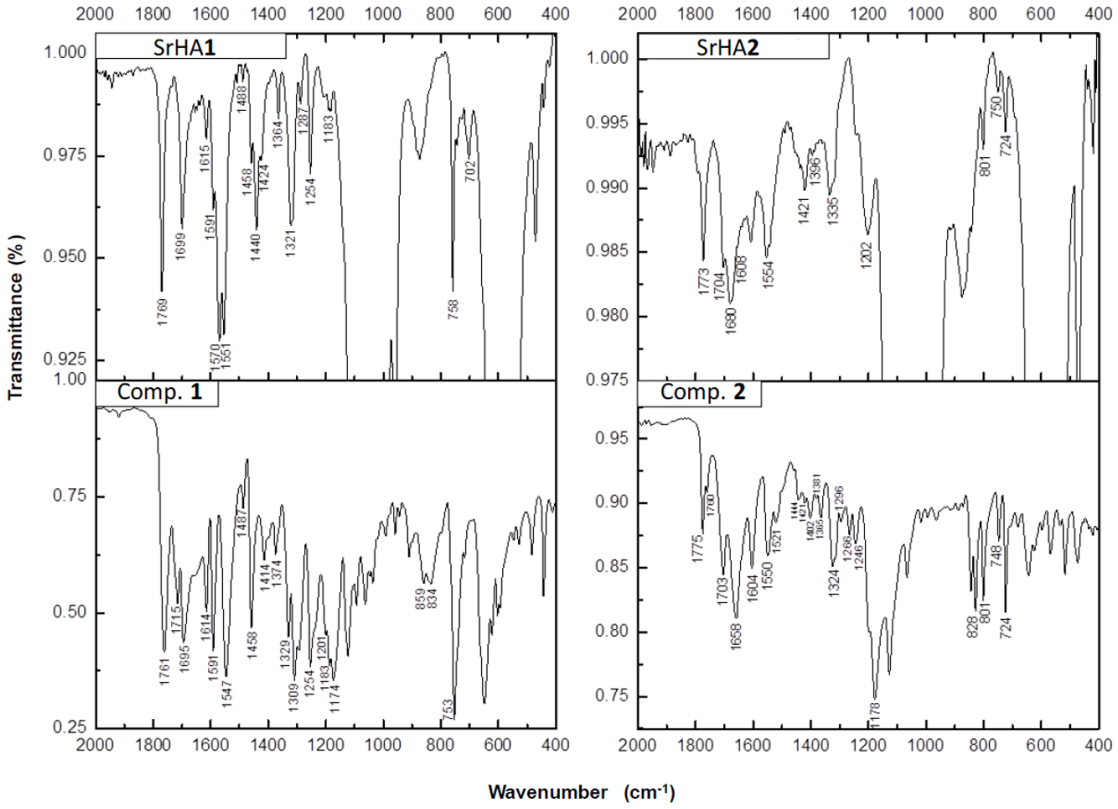

Figure 4.11 - ATR-FTIR spectra in the selected range 2000-400 cm^{-1}: SrHA**1**-12.9 comparison with compound **1** alone, and SrHA**2**-8.4 in comparison with compound **2** alone [*reproduced from Cirillo, et al., 2021*].

Compound **1** showed three C = O stretching bands at 1761 (β-lactam), 1715 (COOH), and 1695 cm^{-1} (urea). The spectrum of SrHA**1** does not show the band corresponding to the C = O stretching of the COOH and the band at 1309 cm^{-1} relative to the CO stretching of the carboxylic acid dimer. Conversely, it shows two new intense bands, one at 1570 cm^{-1} (near the ureidic amide band II at 1551 cm^{-1}), and another at 1440 cm^{-1} that could be both attributed to the asymmetric and symmetric stretching of a carboxylate anion. This analysis supported the hypothesis that β-lactam **1** could have been absorbed onto the SrHA as a carboxylate anion through ionic interactions with Sr^{2+}

or Ca^{2+}. Moreover, since we detected a gap between the two bands of the carboxylate anion minor than 200 cm^{-1}, in our case $\Delta\nu$ = 130, it could be formulated a hypothesis of a monodentate coordination of the carboxylate on the apatite [Deacon, 1980]. In compound **2** the C = O bands were observed at 1773 (β-lactam), 1703 (COOH), and 1658 cm^{-1} (urea), respectively, whereas in the composite SrHA**2** only the C = O of the urea slightly moves to 1680 cm^{-1}. This could account for a less tendency of **2** to form a carboxylate anion upon the adsorption on SrHA if compared to compound **1**, maybe because **2** could establish interactions between the ammonium cation residue and the negatively charged phosphate groups on SrHA surface. The consistency of the β-lactam C = O stretching in pure compounds with those in Sr-HA composites provides strong evidence of the integrity of β-lactam compounds upon adsorption on SrHA.

The in vitro release of β-lactams **1** and **2** from the SrHA composites at different wt% loading was determined through HPLC-UV analysis on supernatant solutions after each refresh. At first, it was observed that a new release occurred just after refreshing the aqueous solution, thus the release was determined as cumulative amount over the refresh number (Figure 4.12).

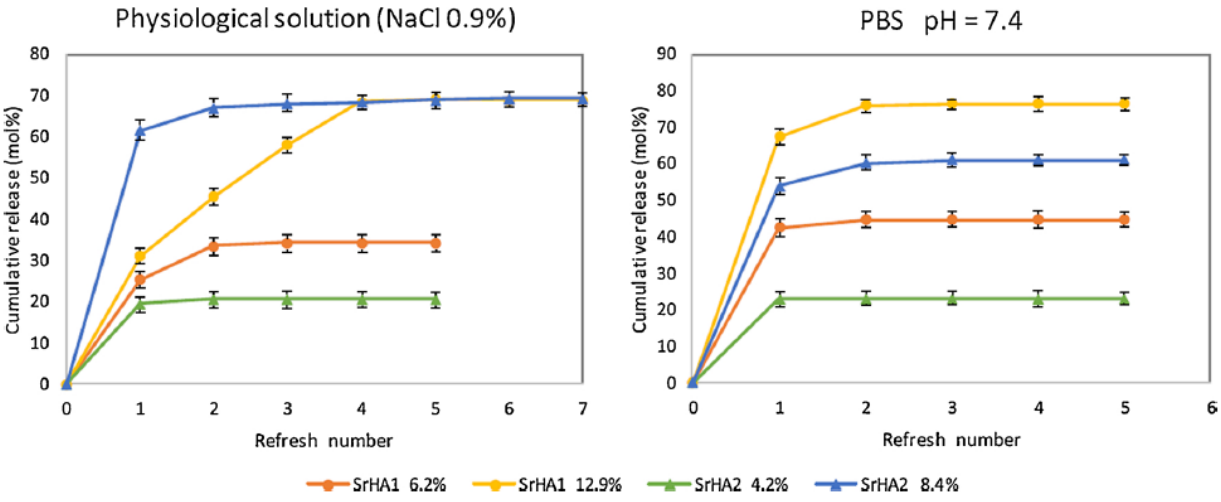

Figure 4.12 - Release of β-lactams compound 1 (●) from SrHA1 and compound 2 (▲) from SrHA2 samples [*reproduced from Cirillo, et al., 2021*].

The release of both compounds in the aqueous media showed an initial burst followed by a steady concentration-dependent profile. Higher concentrations in the SrHA-β-lactam composite released higher amounts of compounds, except for SrHA**1**-12.9 that

has a cumulative release similar to SrHA**2**-8.4 in physiological solution. A further peculiarity of SrHA**1**-12.9 in saline solution regards its more gradual release over time than the other composites; a steady concentration-dependent profile is indeed gained at the fourth refresh, compared to the second in the other SrHA-β-lactams. Generally, for compound **1** the saline solution allowed slightly slower release from SrHA**1** compared to the phosphate buffer. For compound **2** instead, the release rates are comparable in both aqueous solutions. Release over time is shown in Figure 4.13 and 4.14.

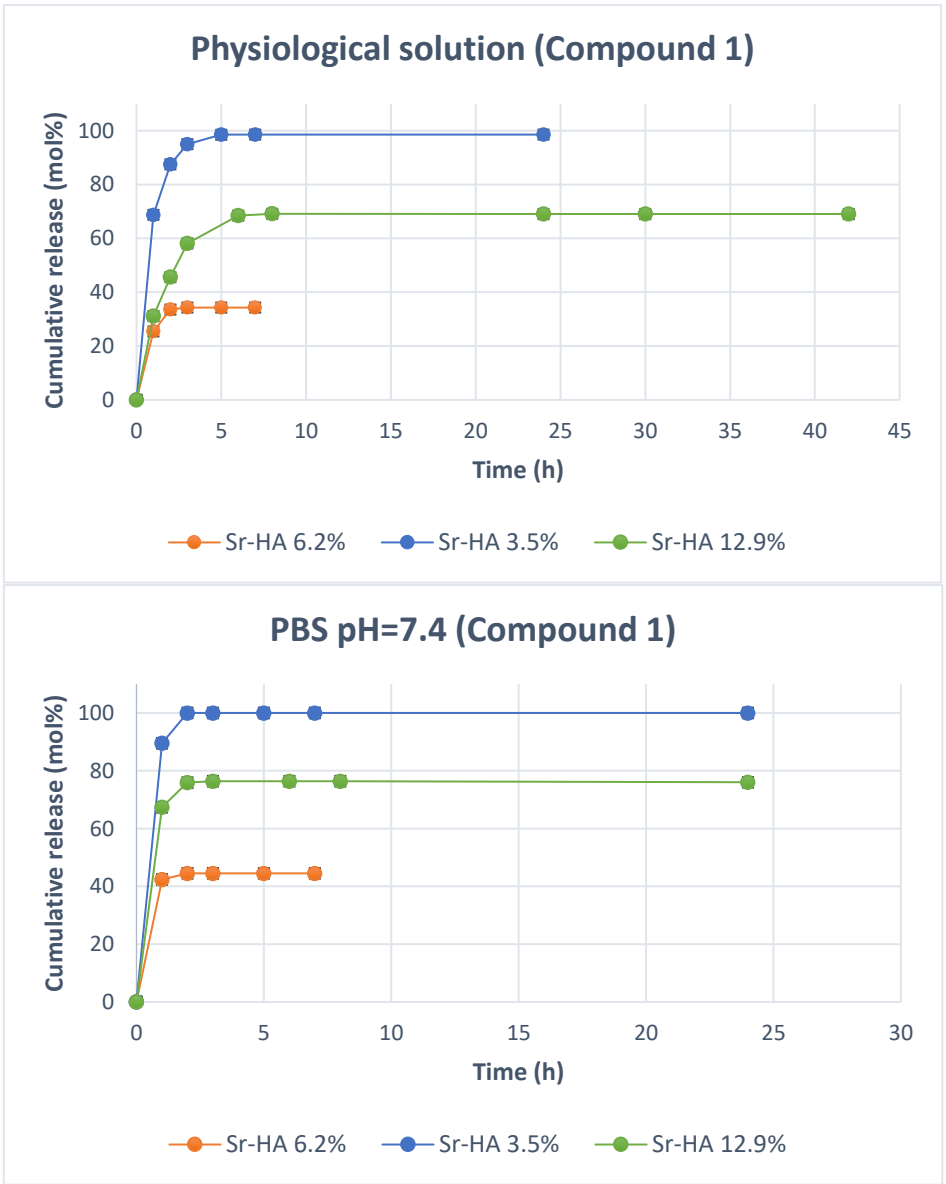

Figure 4.13 - Time-dependent release of compound **1** from SrHA**1** composites [*reproduced from Cirillo, et al., 2021*].

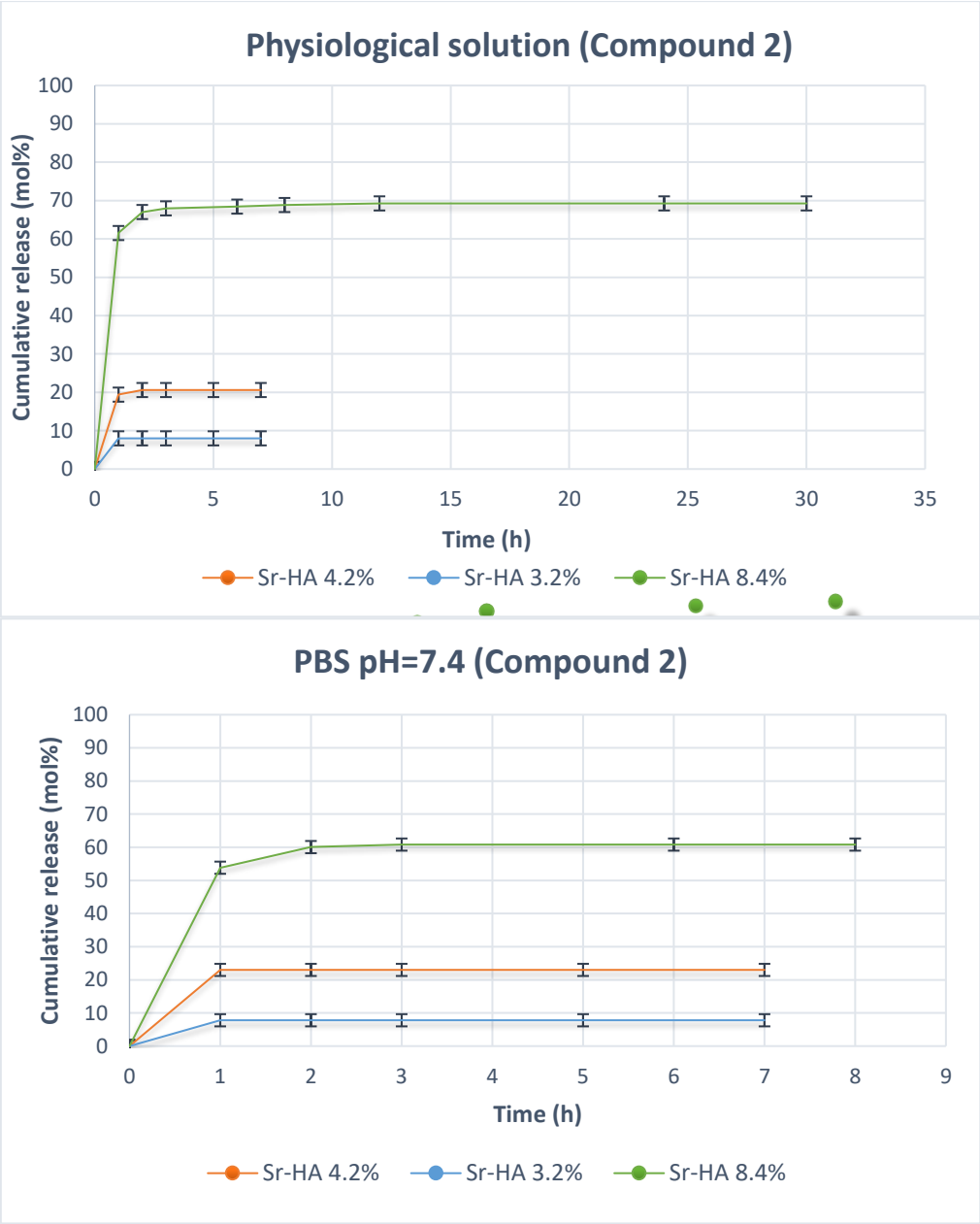

Figure 4.14 -Time-dependent release of compound **2** from SrHA**2** composites

Just SrHA**1**-3.5, the lowest loaded concentration of compound **1**, released all the adsorbed compounds. At variance, the results obtained for the other composites indicate that significant amounts of the β-lactams remained adsorbed on SrHA allowing a persistent bioactivity over time.

No structural and morphological modifications of the samples were observed after β-lactams release (Figure 4.15). Furthermore, the results of chemical analysis showed no significant variation of strontium content.

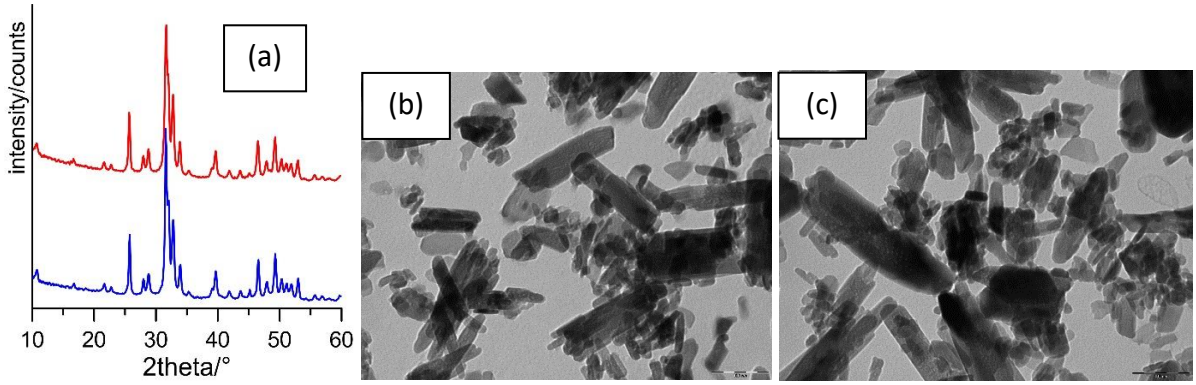

Figure 4.15 - XRD and TEM images of typical samples after β-lactams release. (a) XRD patterns of SrHA**1**-3.5 (bottom) and SrHA**2**-3.2 (top); (b) TEM images of SrHA**1**-3.5; (c) SrHA**2**-3.2.

In conclusion, in this work multifunctionalized materials were obtained by loading β-lactam integrin agonists on strontium substituted hydroxyapatite. The amount of β-lactam compounds onto Sr-hydroxyapatite could be modulated through variation in the polarity of the loading solution. After an initial burst, the release of both β-lactams in aqueous solution reached a steady state, maintaining a significant local concentration over time [Cirillo, 2021].

1.3 Functionalization of brushite with aspartic and poly-aspartic acids.

The study of the synthesis and hydrolysis of brushite (DCPD, $CaHPO_4 \cdot 2H_2O$) has been carried out in the presence of aspartic acid (ASP) and poly-aspartic acid (PASP), as models of acidic macromolecules of biomineralized tissues. Indeed, the biological environment of the deposition and possible transformation of the inorganic phase of the hard tissue of vertebrates is rich in proteins containing significant amounts of acidic amino acids, such as aspartic and glutamic acids. [Dorozhkin, 2016]. Even if the inorganic phase is a basic calcium phosphate, structurally similar to the synthetic hydroxyapatite, the focus here is on brushite, which occurs as a precursor phase and is often found in pathological calcifications [Zhang, 2014].

1.3.1 Synthesis of DCPD-ASP

Syntheses in the presence of aspartic acid (ASP) were carried out by inserting the additive in the phosphate solution during the direct synthesis of DCPD crystals. ASP concentrations calculated on final volume were 1, 2, 5, and 10 mM, and samples were labelled ASP1, ASP2, ASP5, and ASP10, respectively.

The results of the characterization carried out on the products synthesized in the presence of ASP indicate that the presence of amino-acid in solution does not cause any structural or morphological modification.

Indeed, the XRD patterns of all the samples show the presence of DCPD as a unique crystalline phase (Figure 4.16a) without any significant variation both in the relative intensity and in the width of the peaks. Furthermore, SEM images show the characteristic plate-like morphology of the DCPD crystals (Figure 4.16b).

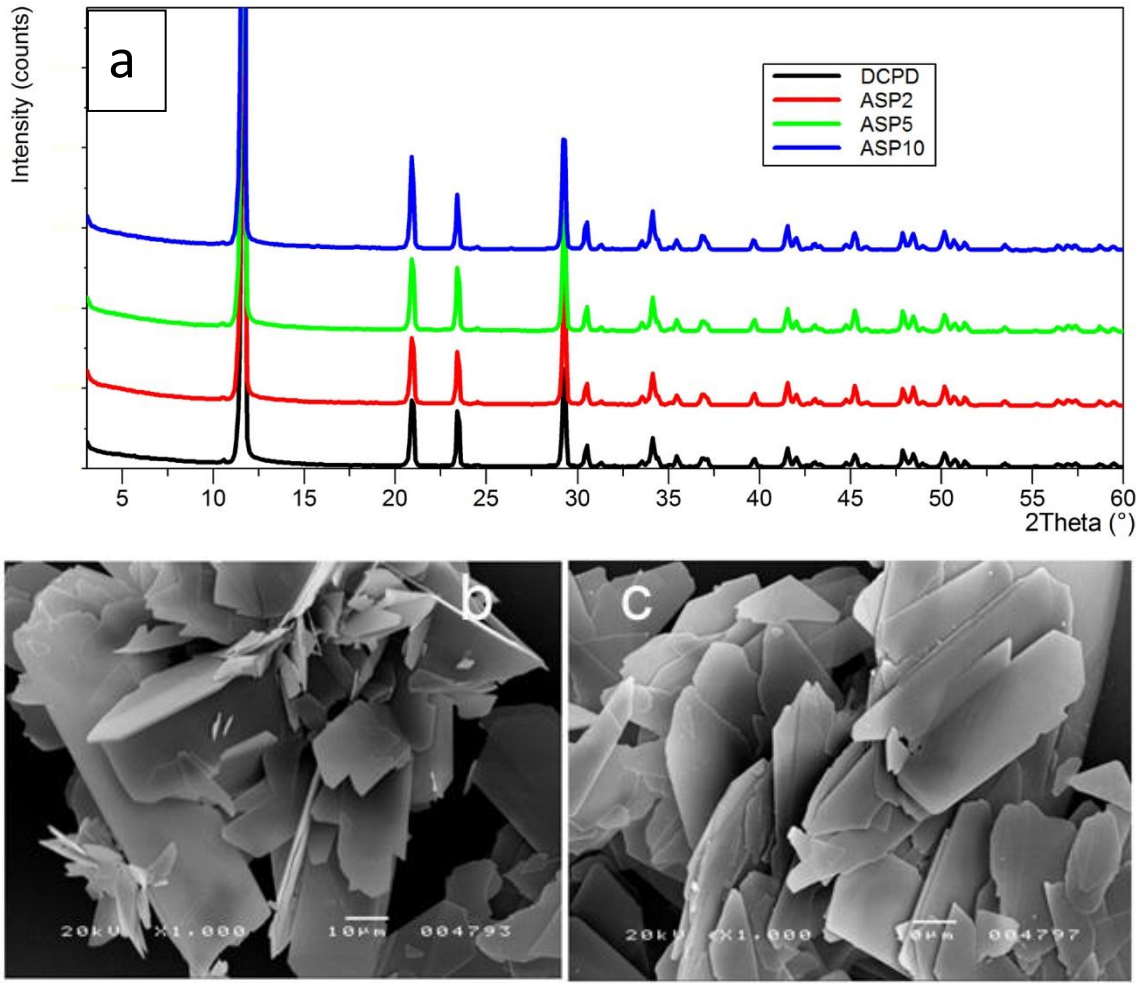

Figure 4.16 – XRD patterns (a) and SEM images of (b) DCPD crystals and (c) synthesized in the presence of ASP 10 mM.

Actually, the elemental analysis of light elements has revaled that aspartic acid is not detectable in the precipitates and the final obtained materials are not composites. The data of zeta potential further support the absence of aminoacid in the samples (Table 4.2).

Table 4.2 - Values of masses, ΔH of the endothermic transition from DCPD to DCPA, zeta potential of the samples synthesized in the presence of ASP.

Sample	Mass (g)	ΔH (J/g)	Zeta potential (mV)
DCPD	1.146	400	- 12.0
ASP5	1.151	406	- 11.6
ASP10	1.134	400	- 12.5

In agreement, the DSC plots of the different samples do not vary (Figure 4.17) and the values of ΔH associated to the phase transformation from DCPD to DCPA are always very close to those of pure DCPD (Table 4.2).

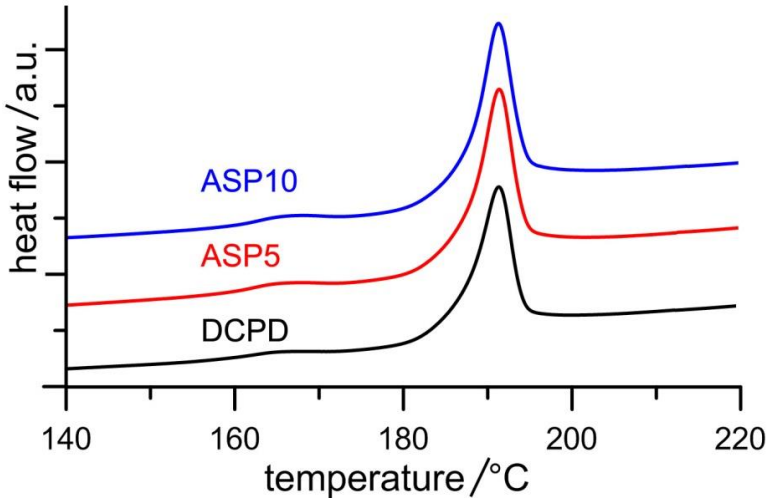

Figure 4.17 - DSC plots showing the thermal behavior of the products obtained from the synthesis of DCPD in the presence of increasing concentrations of ASP [*reproduced from Rubini, et al., 2019*].

Again, the morphology of the crystals and the relative intensity distributions of the XRD peaks recorded from all samples after heat treatment at 300 °C are not significantly different from those of heat-treated pure DCPD (Figure 4.18). The presence of a quantity of small particles on the surface of the crystals is most likely due to a partial crumbling of the crystal during dehydration caused by heat treatment.

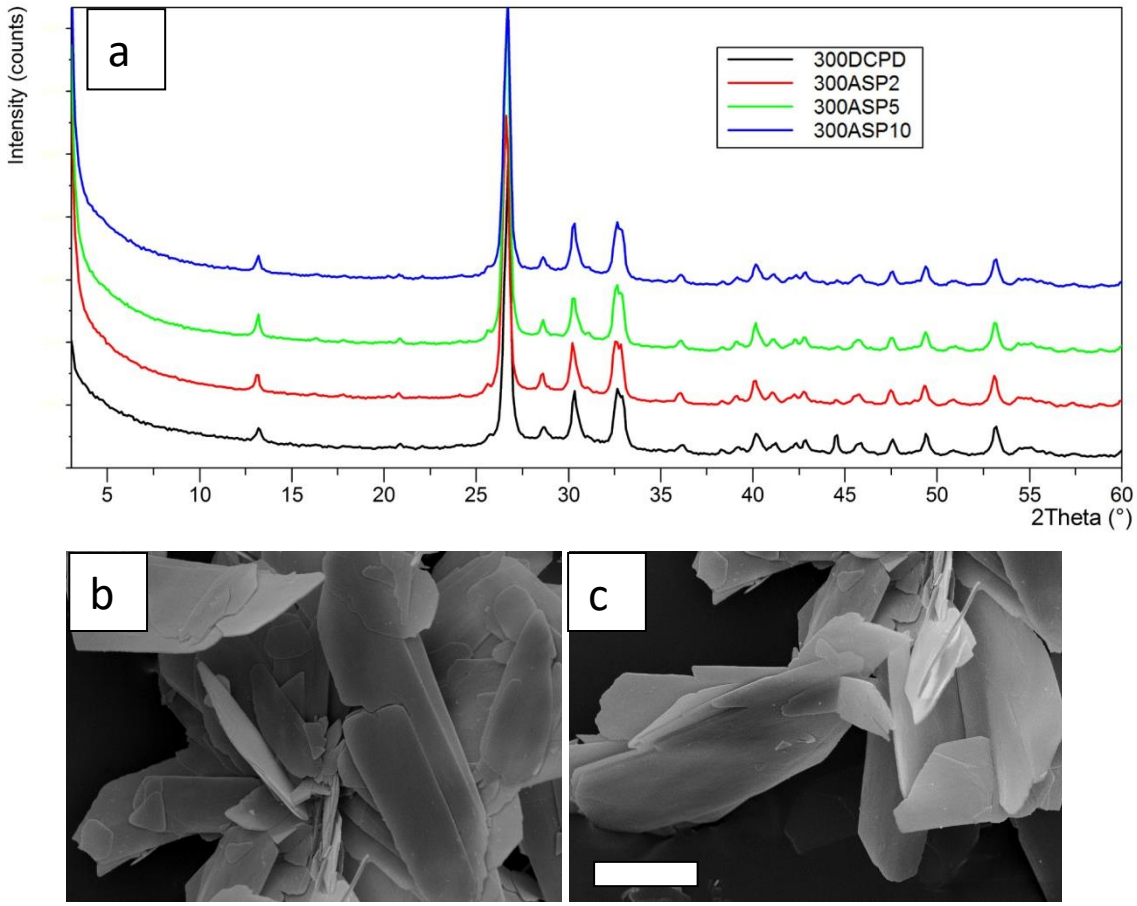

Figure 4.18 – Heat-treated samples: (a) XRD patterns and SEM images of (b) 300DCPD and (c) 300ASP10 (scale-bar= 20 μm).

1.3.2 Synthesis of DCPD-PASP

Syntheses in the presence of the sodium polyaspartate (MW 11,000) were carried out by inserting the additive in the phosphate solution during the direct synthesis of DCPD crystals. PASP concentrations calculated on the final volume were 0.2, 0.5, 0.8, and 1 mM (in monomer), thereby samples were labelled PASP02, PASP05, PASP08, and PASP1, respectively.

Differently with what was found for the influence of ASP on the synthesis of DCPD, all the results obtained on the products of synthesis in the presence of PASP indicate that the poly-aminoacid exerts a significant effect. First of all, the significant decrease of reaction yield on increasing PASP concentration (Table 4.3) indicates an inhibitory role of the poly-amino acid on the crystallization of DCPD. Secondly, the results of elemental analysis indicate a significant content of carbon, which increases with PASP concentration in solution and allows us to calculate that the samples contain up to about

2.3 wt% of the poly-aminoacid (Table 4.3). As a direct consequence, the values of zeta potential are more negative for the products synthesized in the presence of PASP than that measured for pure DCPD (Table 4.3).

Table 4.3 - Values of masses, ΔH of the endothermic transition from DCPD to DCPA, zeta potential of the samples synthesized in the presence of PASP.

Sample	Mass (g)	ΔH (J/g)	Zeta potential (mV)	PASP content (wt%)
DCPD	1.146	400	- 12.0	---
PASP0.2	0.691	326	- 23.0	0.4
PASP0.5	0.481	302	- 21.1	1.0
PASP0.8	0.220	216	- 23..3	2.3

The XRD patterns show that all the samples contain DCPD as unique crystalline phase up to PASP concentration in solution of 0.8 mM (Figure 4.19). PASP concentration of 1 mM provokes the appearance of a broad halo superimposed to the reflections of DCPD, which becomes the only appreaciable feature for further increase of PASP up to 1.5 and 2 mM indicating the precipitation of amorphous material only.

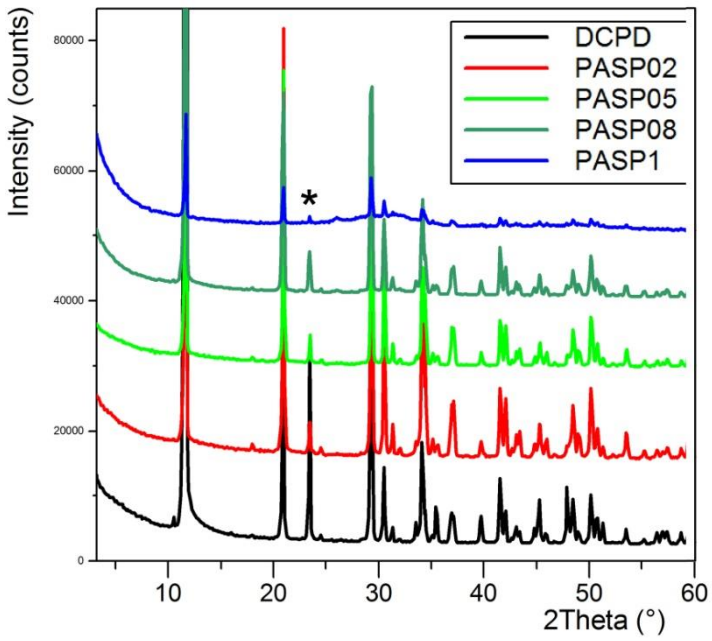

Figure 4.19 - XRD patterns of DCPD crystals synthesized at different concentrations of PASP. The symbol * indicates 040 peak.

The patterns of PASP02, PASP05, and PASP08 display a slightly modified distribution of the relative intensity of the diffraction peaks when compared to pure DCPD. In particular, the decrease of the relative intensity of the 040 reflection ($2\theta = 23.4°$) can be explained by the orientation effect and morphology variation [Landin, 1994]. The plate-like DCPD crystals tend to lie flat on the sample holder of the diffractometer, with consequent enhancement of the relative intensity of the 0k0 peaks. Crystal aggregation of the products synthesized in the presence of PASP reduces this phenomenon and, therefore, the relative intensity of the relevant XRD peaks.

PASP has indeed a great effect on the morphology of the precipitates. SEM images reported in Figure 4.20 show that the crystals synthesized in the presence of PASP up to PASP08 get smaller and smaller and exhibit indented edges and a strong tendency to aggregate into spherulites. The material precipitated in the presence of 1 mM PASP contain a significant amount of amorphous phase and the presence of crystals is barely appreciable.

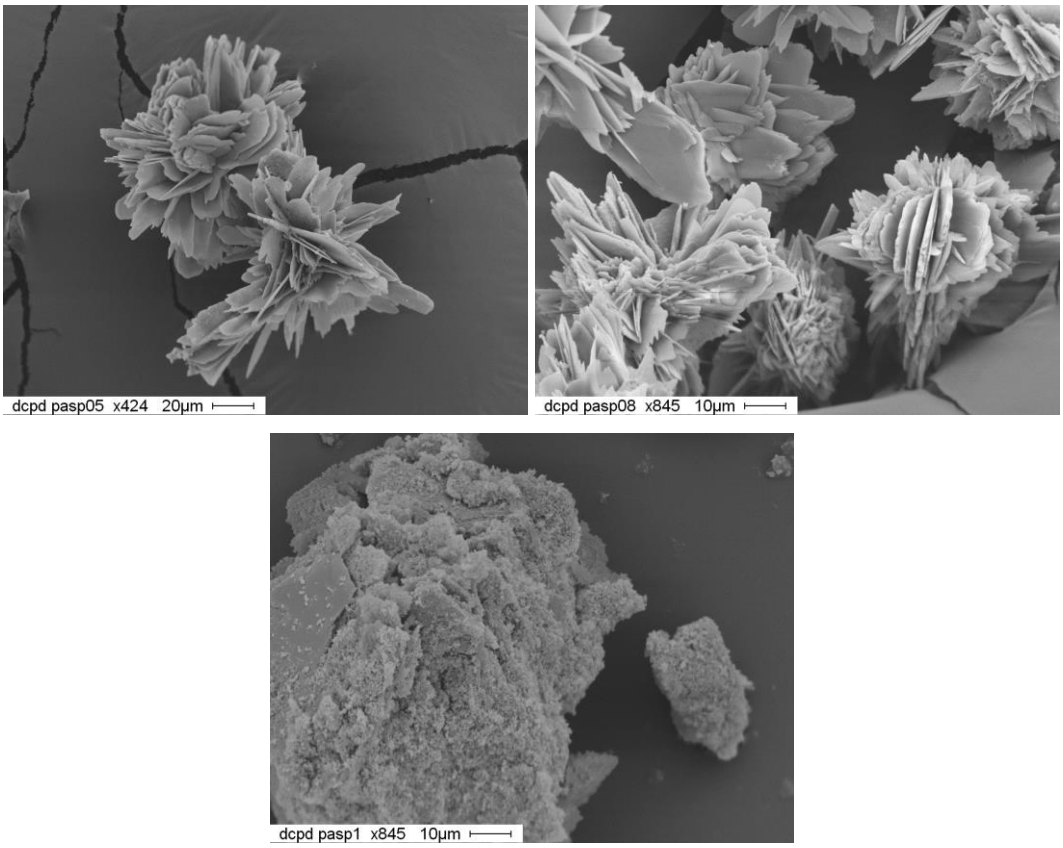

Figure 4.20 - SEM images of the products obtained from the synthesis of DCPD in the presence of PASP.

Good structural fit between PASP and the (0k0) faces of DCPD crystals can favor their interaction. Indeed, the distances between neighboring calcium ions on the (0k0) faces along the crystallographic *a* direction (6.23 Å) are very close to those between carboxylic groups in the polyaspartic β-sheet (6.90 Å). Since PASP in solution has not a rigid structure, the carboxylic groups along the orthogonal direction to the crystal flat plane ((0k0) plane) can interact with the calcium ions exposed on the large crystal face. This interaction model (Figure 4.21) is much more convincing than that previously advanced on the basis of the distances between neighboring calcium ions from two adjacent layers within one Ca-HPO4 bilayer (parallel to the (0k0) plane), which were erroneously reported as 6.95 Å [Sikiric, 2000].

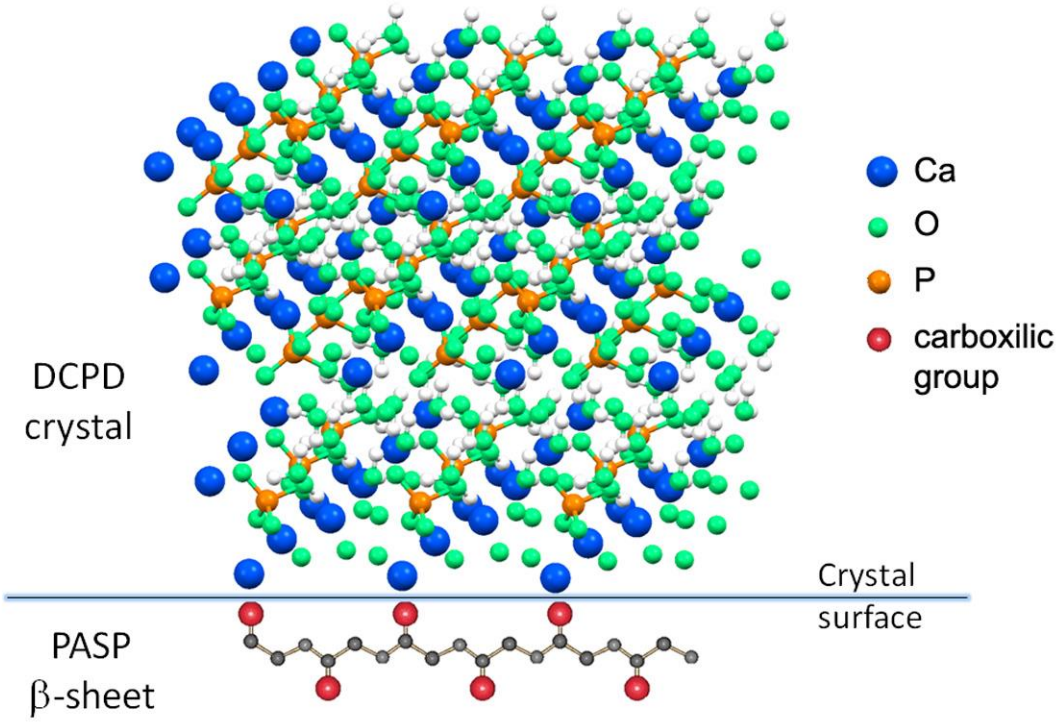

Figure 4.21 - Possible interaction between carboxylic groups in the polyaspartic β-sheet and the calcium ions exposed on the large DCPD crystal face ((0k0) plane).

The results of the Differential Scanning Calorimetry analysis put into evidence the influence of the polyelectrolyte on the stability of DCPD. In fact, although the endothermic peak corresponding to the transformation of the DCPD into DCPA occurs at about 190 °C for all the samples (Figure 4.22), the values of ΔH associated to this process decreases significantly as a function of PASP concentration in solution, as

shown in Table 4.3. The decrease of the energy required to transform DCPD into its anhydrous form on increasing the presence of PASP in the reaction medium suggests that the poly-aminoacid destabilizes DCPD structure.

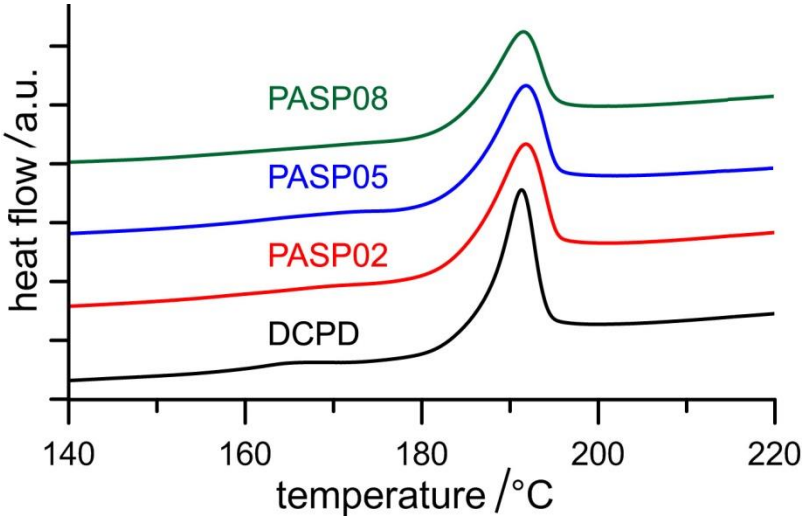

Figure 4.22 - DSC plots showing the thermal behavior of the products obtained from the synthesis of DCPD in the presence of increasing concentrations of PASP [*adapted from Rubini, et al., 2019*].

The FT-IR spectrum of DCPD shows the presence of a number of absorption bands due to H_2O stretching (3000–3500 cm^{-1}) and bending (1651 cm^{-1}), PO stretching (900–1300 cm^{-1}) and bending (500–700 cm^{-1}) modes, as well as to P-O(H) stretching at about 876 cm^{-1} (Figure 4.23) [Tas, 2004; Xu, 1999]. The FT-IR spectrum of PASP08 displays, other than the characteristic bands of DCPD, a shoulder at about 1580 cm^{-1} and an absorption band at about 1410 cm^{-1} in agreement with the presence of the polyelectrolyte, as it can be inferred by comparing the spectrum with that of PASP (Figure 4.23).

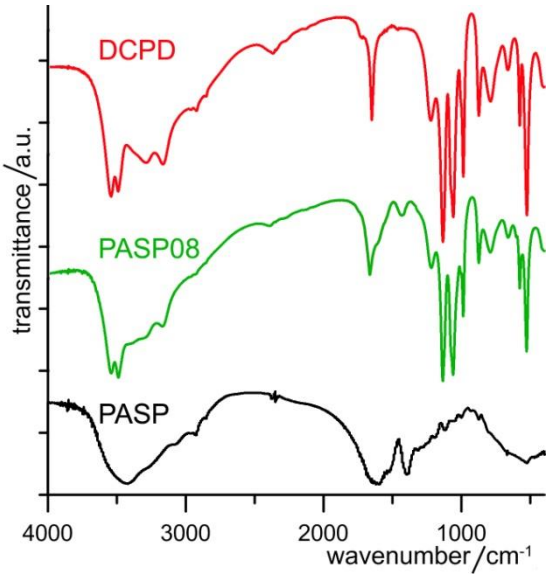

Figure 4.23 - FT-IR spectra of the DCPD and PASP08 synthesized samples, compared with that of PASP powder [*adapted from Rubini, et al., 2019*].

After heat treatment at 300 °C, the PASP containing powders display a pale-yellow color, which becomes darker on passing from PASP02 to PASP08 (Figure 4.24), due to the partial combustion of organic material and residual C remains. On the contrary, the samples prepared in the presene of ASP were absolutely white, confirming the absence of amino acid.

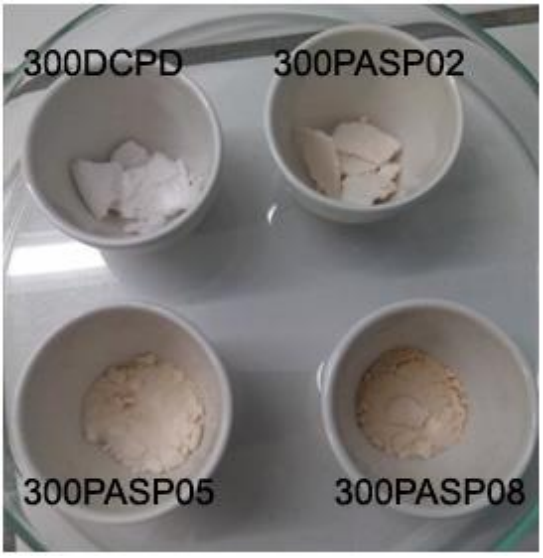

Figure 4.24 - Photograph of the samples obtained from the synthesis of DCPD in the presence of increasing concentrations of PASP after heat treatment at 300 °C. Powders display a pale yellow color, which becomes darker on passing from 300PASP02 to 300PASP08, due to the partial combustion of organic material and residual C remains.

After heat treatment, all the samples exhibit XRD patterns consistent with the presence of DCPA as unique crystalline phase (Figure 4.25). In addition, similarly to samples before treatment, even after heat treatment the patterns of the PASP functionalized samples present a slightly different distribution of the relative intensity of the reflections in comparison with that of the sample obtained by heat treatment of pure DCPD.

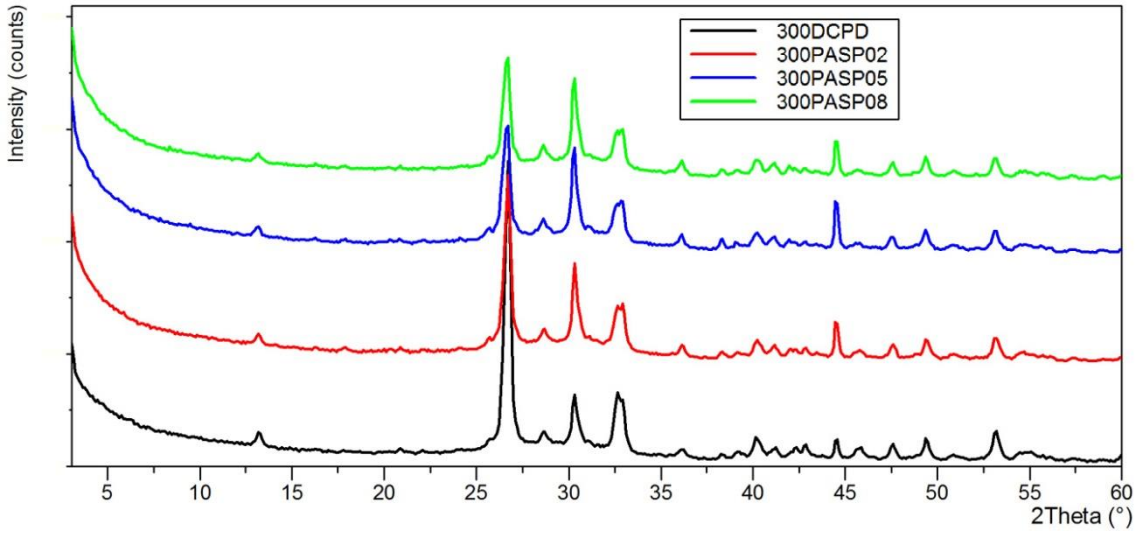

Figure 4.25 - Powder X-ray diffraction patterns of the products obtained from the synthesis of DCPD in the presence of increasing concentrations of PASP after heat treatment at 300 °C.

The differences can be ascribed to the different morphology of the samples: plate-like for 300DCPD (Figure 4.18b), which can result in crystal orientation, and spherulitic for 300PASP samples (Figure 4.26).

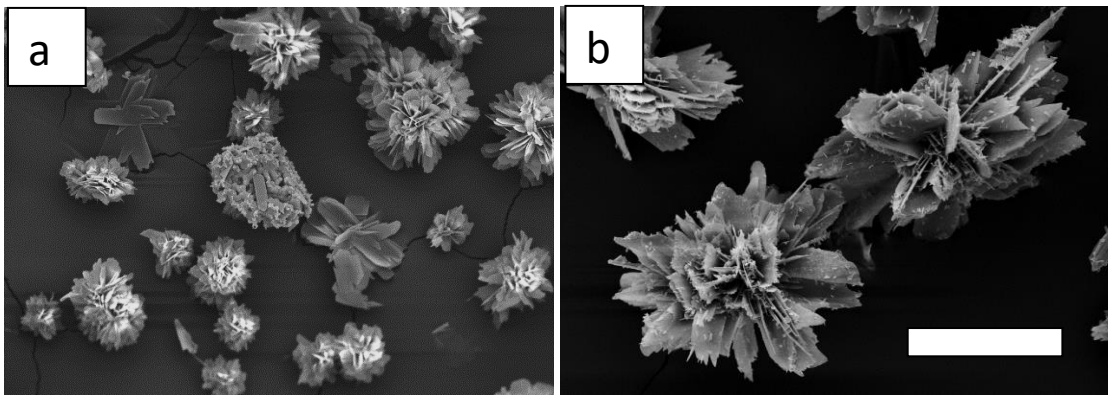

Figure 4.26 - SEM images of DCPD crystals synthesized at different concentrations of PASP after heat treatment at 300°C: (a) 300PASP02 and (b) 300PASP08.

The results of this work highlight the different influences of PASP and ASP on the synthesis of DCPD. PASP inhibits the crystallization of DCPD, which is completely hindered when the concentration of the polyelectrolyte exceeds 1 mM in monomeric units. At lower concentrations, PASP reduces the yield of the reaction and provokes aggregation of the DCPD crystals, most likely through interaction with the (0k0) faces. Functionalization with PASP up to about 2.3 wt% reduces the stability of the DCPD structure, thus that the energy required for its thermal transition into DCPA decreases as PASP content increases. On the contrary, the presence in solution of ASP, up to 10 mM does not affect the structure, as well the morphology and stability, of the products of synthesis of DCPD [Rubini, 2019].

1.3.3 Hydrolisis

It is well known that DCPD crystals stored in aqueous solution undergo phase conversion into octacalcium phosphate or hydroxyapatite in time, depending on solution composition, pH and temperature [Elliott, 1994; Shamrai, 2015]. On comparing the results obtained when the hydrolysis is carried out at 37 °C with those at 60 °C, it is evident that increasing the temperature accelerates the transformation of DCPD into thermodynamically more stable phases (Tables 4.4 and 4.5). In particular, at 37 °C pure DCPD is partially transformed into OCP after just 3 h (the conversion into OCP is complete after 2 days) and at 3 days HA appears as a secondary phase; whereas at 60 °C, HA is present very early, and it is the only crystalline phase after just 2 days.

The role played by ASP and PASP on the hydrolysis reaction of DCPD has been evaluated following two different routes, which consisted in following the reactions of: (a) brushitic samples synthesized in the presence of PASP and ASP (PASP08 and ASP10); (b) DCPD incubated in physiological solution containing PASP 0.8 mM in monomer (inPASP08) or ASP 10 mM (inASP10) [Rubini, 2019].

Table 4.4 - Crystalline phases of the products obtained after different periods of samples storage in solution at 37°C.

Sample	**3h**	**6h**	**9h**	**15h**	**24h**	**48h**	**72h**
DCPD	D+O	D+O	D+O	D+O	D+O	O	O+H
PASP08	D+O	D+O	D+O	D+O	D+O	D+O	D+O
inPASP08	D	D	D	D	D	D	D+O
ASP10	D+O	D+O	D+O	D+O	D+O	O	O+H
inASP10	D	D	D	D	D	D	D+O

D = DCPD; O = OCP; H = HA.

Table 4.5 - Crystalline phases of the products obtained after different periods of samples storage in solution at 60°C.

Sample	3h	6h	9h	15h	24h	48h	72h
DCPD	O+D+ H	O+H	O+H	O+H	H+O	H	H
PASP08	D+O+ H	D+O+ H	D+O+H	H+O+ D	H+O+ D	H+O+D	H+O
inPASP08	D+OCP	D+O	D+O	D+O	O+D	O+D	O+D
ASP10	O+D+ H	O+H	O+H	O+H	H+O	H	H
inASP10	D+O	O+D	O	O+D	O	O	O

D = DCPD; O = OCP; H = HA.

The data obtained for PASP08 confirm the presence of the poly-amino acid in the sample. In fact, the phase conversion is delayed when compared to that observed for pure DCPD: after 3 days at 37 °C just a part of DCPD is converted into OCP, whereas at 60 °C the phases obtained after 3 days are OCP and HA. On the contrary, the hydrolysis of ASP10 proceeds with the same trend as that of pure DCPD, in agreement with the absence of aspartic acid in the sample.

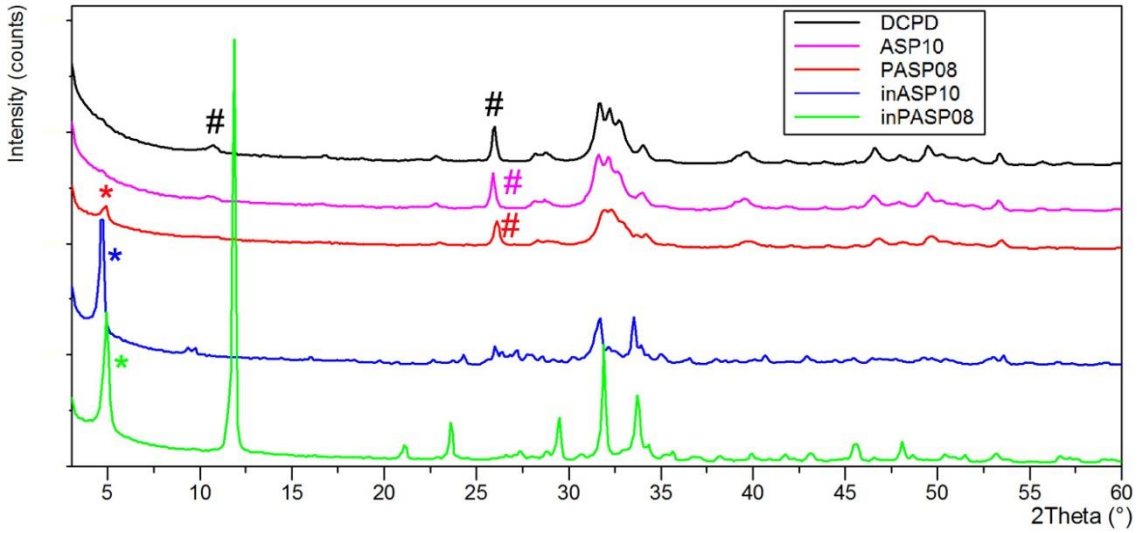

Figure 4.27 – XRD patterns of the products obtained from the hydrolysis of DCPD, PASP08, and ASP10 in physiological solution and of DCPD in the presence of PASP (inPASP08) or ASP (inASP10) after 3 days at 60 °C. The symbols (*) and (#) indicate peaks diagnostic of OCP, and HA, respectively

Furthermore, the presence of PASP or ASP in solution results in a strong inhibition of the conversion of DCPD, as shown by the data reported in Tables 4.4 and 4.5 and by comparing the XRD patterns recorded from the different samples after three days at 60 °C (Figure 4.27). The inhibition is greater for PASP, so that the pattern of inASP08 still shows the presence of DCPD even after 3 days at 60 °C.

The presence of the different phases can be appreciated also by comparing the FT-IR spectra of the samples after 3 days of hydrolysis at 60 °C (Figure 4.28). In particular, the absence of the bands at 3572 and 630 cm^{-1}, due to OH stretching and bending modes respectively, in the spectra of DCPD and ASP10 confirms the poor crystallinity of the apatitic phases obtained from their hydrolysis. The spectrum of inASP after hydrolysis shows the characteristic bands of OCP [Fowler, 1993], whereas that of inPASP exhibits a greater number of bands due to the co-presence of OCP and DCPD (Figure 4.28). Moreover, the band at about 1410 cm^{-1} in the spectra of PASP08 and inPASP after hydrolysis indicates the presence of the polyelectrolyte in these samples.

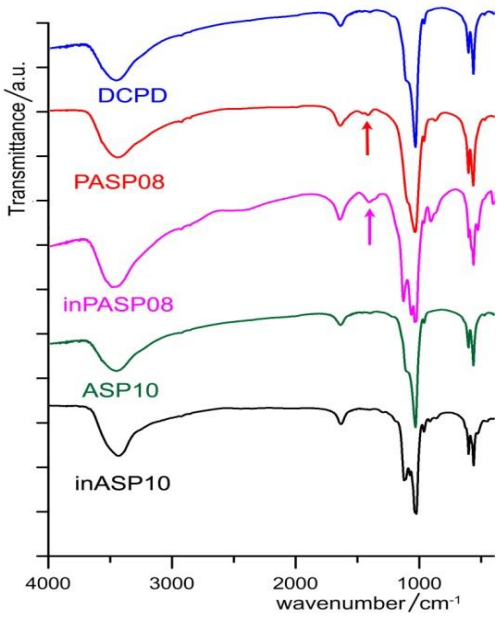

Figure 4.28 – FTIR spectra of samples obtained after 3 days of hydrolisis at 60 °C. Arrows indicate the presence of PASP [*adapted from Rubini, et al., 2019*].

Further evidences of the different products of hydrolysis come from SEM images (Figure 4.29): the image of inPASP08 still shows big crystals of DCPD, whereas platelets and/or needles are evident in the images of the samples constituted of OCP and/or HA.

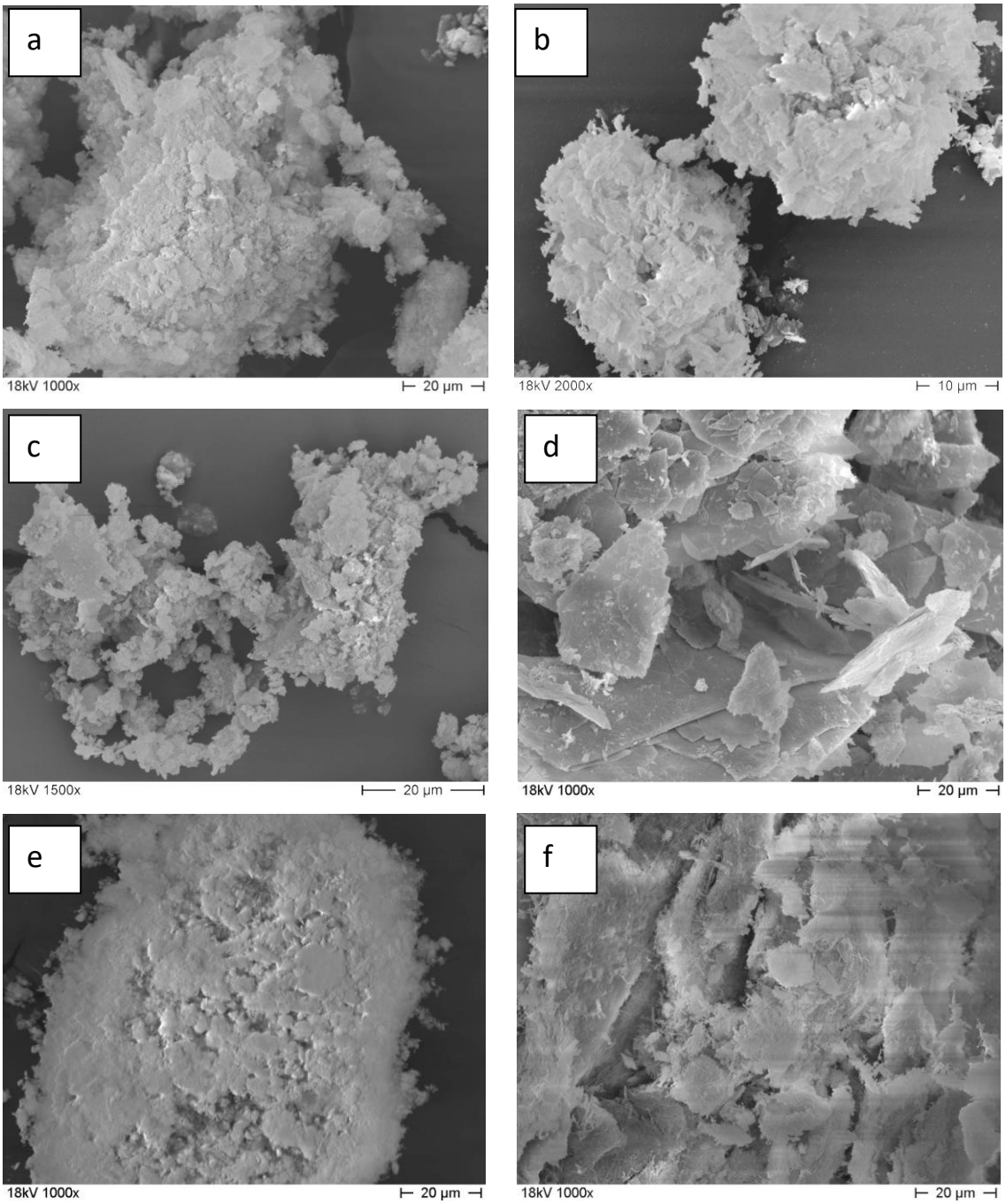

Figure 4.29 - SEM images of the products obtained from the hydrolysis reaction of (a) DCPD at 60 °C; (b) DCPD at 37 °C; (c) PASP08 and (d) inPASP08 at 60 °C; (e) ASP10 and inASP10 at 60 °C.

The stronger inhibition exerted by the poly-amino acid is not surprising and can be ascribed to the cooperative action of the carboxylate groups and to its good structural fit with DCPD, which promotes PASP adsorption on the surface of the (0k0) faces [Sikiric,

2000]. A similar mechanism was previously reported for the inhibition effect of PASP on OCP hydrolysis, where adsorption of the polyelectrolyte on the hydrated layer of the OCP (100) faces prevents OCP transformation into HA [Bigi, 2003].

In conclusion, the results obtained on the synthesis of the DCPD are supported by those recorded on the hydrolysis reaction. In fact, in physiological solution, the products synthesized in the presence of ASP exhibit the same extent of conversion into the more stable phases, OCP and/or HA, as that observed for pure DCPD. At variance, the samples containing PASP are characterized by a delayed conversion in solution. ASP and PASP also maintain a different behavior when dissolved in the hydrolysis solution: both delay the phase transition, but PASP exerts a stronger inhibition than ASP [Rubini, 2019].

1.4 Ionic substitution of strontium in the structure of monetite.

The studies on strontium substitution in CaPs are aimed to clarify the modifications induced by this ion on the chemistry, structure and morphology of these compounds and, at the same time, to verify their possible use as delivery systems of Sr [Salamanna, 2019; Roy, 2013].

Monetite, α-$CaHPO_4$, which was already known to be isomorphous with α-$SrHPO_4$ [Boudjada, 1978], is largely used in the composition of biomaterials for hard tissue substitution/repair. Herein, DCPA has been synthesized in the presence of increasing amounts of Sr^{2+}, with the aim to investigate the chemical, structural and morphological modifications induced by strontium substitution to calcium in the structure of DCPA. To this purpose, two different procedures have been followed, as reported in Chapter 2 - Experimental Section – Preparation of Materials – par. 1.3: (i) direct synthesis in aqueous solution in the presence of increasing strontium concentrations; (ii) dehydration of strontium-substituted DCPD [Boanini, Gazzano, *et al.*, 2021].

1.4.1 Direct synthesis

Direct synthesis in the presence of increasing strontium concentration in solution allows getting products constituted by a single crystalline phase in the whole range of composition (Figure 4.30).

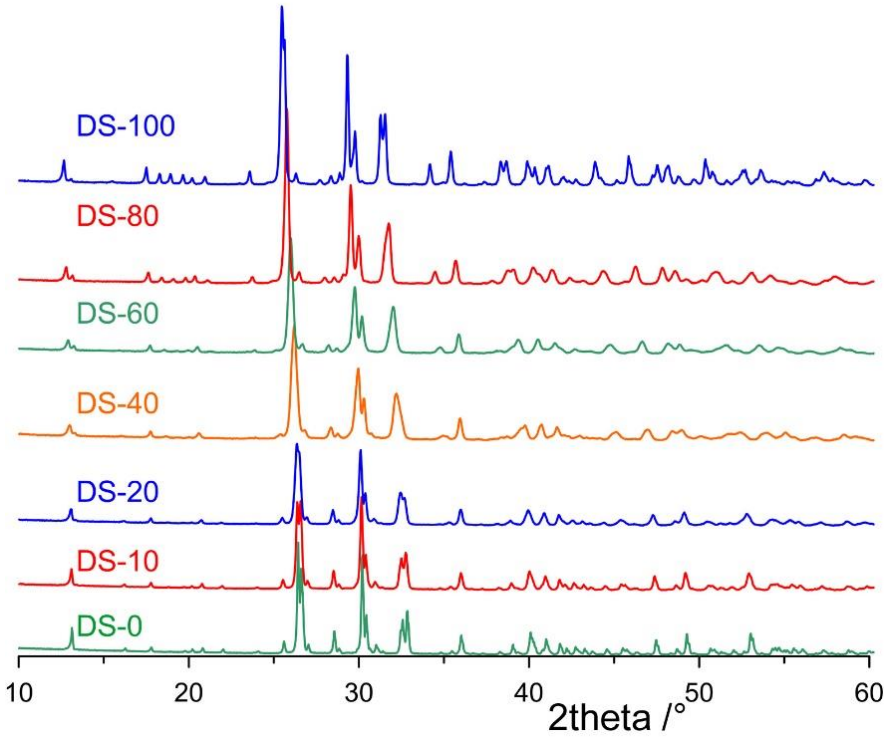

Figure 4.30 – XRD apatterns of samples obtained by direct synthesis on changing Sr concentration [*reproduced from Boanini, Gazzano, et al., 2021*].

A shift of the main diffraction peaks towards smaller angles can be observed on increasing strontium concentration in solution: the increasing values of the interplanar distances suggests strontium incorporation into monetite structure. Replacement of calcium with strontium, which has a greater scattering power, causes important variations in the diffraction intensities of several peaks. The X-ray pattern of DS-100 is that characteristic of α-$SrHPO_4$, which is isomorphous with α-$CaHPO_4$ [Boudjada, 1978].

In agreement with XRD results, chemical analysis of Sr content reported in Table 4.6 indicates a quantitative Sr incorporation into the solid phase.

The results of the refinements, which were performed with the Rietveld method, reached convergence and good agreement indexes, as shown by the final plots reported in Fig. 4.31, and confirmed that all the samples are constituted of DCPA as the only crystalline phase.

Table 4.6 – Analytical and structural results for samples obtained through direct syntheses [*reproduced from Boanini, Gazzano, et al., 2021*].

	Cell parameters*						
Sample	a (Å)	b (Å)	c (Å)	alfa(°)	beta(°)	gamma(°)	V (Å^3)
DS-0	6.902	6.635	6.990	96.2	104.0	88.4	308.8
DS-10	6.919	6.643	7.004	96.1	104.1	88.5	310.5
DS-20	6.939	6.649	7.018	96.0	104.1	88.5	312.3
DS-40	7.030	6.695	7.099	95.2	104.8	88.8	321.8
DS-60	7.077	6.712	7.129	95.0	104.8	88.8	326.2
DS-80	7.138	6.752	7.186	94.7	104.9	88.9	333.5
DS-100	7.190	6.797	7.263	94.6	105.0	88.8	341.8
	Sr occupation factor*		Sr content (at%)		τ_{hkl} (nm)**		
Sample	site 1	site 2	Rietveld	Chemical	τ_{001}	$\tau_{0\text{-}11}$	$\tau_{1\text{-}20}$
DS-0	0.00	0.00	0	0	66	92	104
DS-10	0.05	0.03	4	6	58	62	63
DS-20	0.12	0.12	12	13	45	54	54
DS-40	0.30	0.46	38	35	34	45	23
DS-60	0.40	0.73	57	56	34	43	31
DS-80	0.72	0.84	78	79	39	40	48
DS-100	1.00	1.00	100	100	45	44	62

Notes: * estimated errors: a, b, c ± 0.002 Å, alfa, beta, gamma ±0.1°, V ± 0.1 Å^3, OF ±0.02. ** for $\tau_{1\text{-}20}$ relative to the couple 1 -2 0 / -1 -2 0 reflections. τ_{hkl} is the mean coherent length of the perfect crystalline domains along the orthogonal direction to the hkl plane

The values of cell parameters (Table 4.6) increase on increasing Sr content, in agreement with the substitution of Ca ion (ionic radius: 0.112 nm) with the bigger Sr ion (ionic radius: 0.126 nm). In particular, the values of *a*, *b* and *c* increase linearly with the increase of Sr content from DCPA-0 to DCPA-100. Sr content evaluated through structural refinements is in very good agreement with the analytical content (Table 4.6).

Furthermore, measurement of FWHM (full width at half maximum) of some selected peaks was used to calculate the mean dimensions of the coherent length of the perfect crystalline domains (τhkl). The results (Table 4.6) indicate that these dimensions decrease up to a Sr content of about 50 at%, and then increase as Sr amount further increases up to 100 at%.

The values of the occupancy factors (Table 4.6) for samples at Sr contents less than 50 at% do not show a clear preference of Sr ion for one of the two crystallographycally independent metal sites, in agreement with their similar Ca–O mean distances [Catti, 1977]. However, samples at high Sr content exhibit a preferential occupancy for the metal site (2).

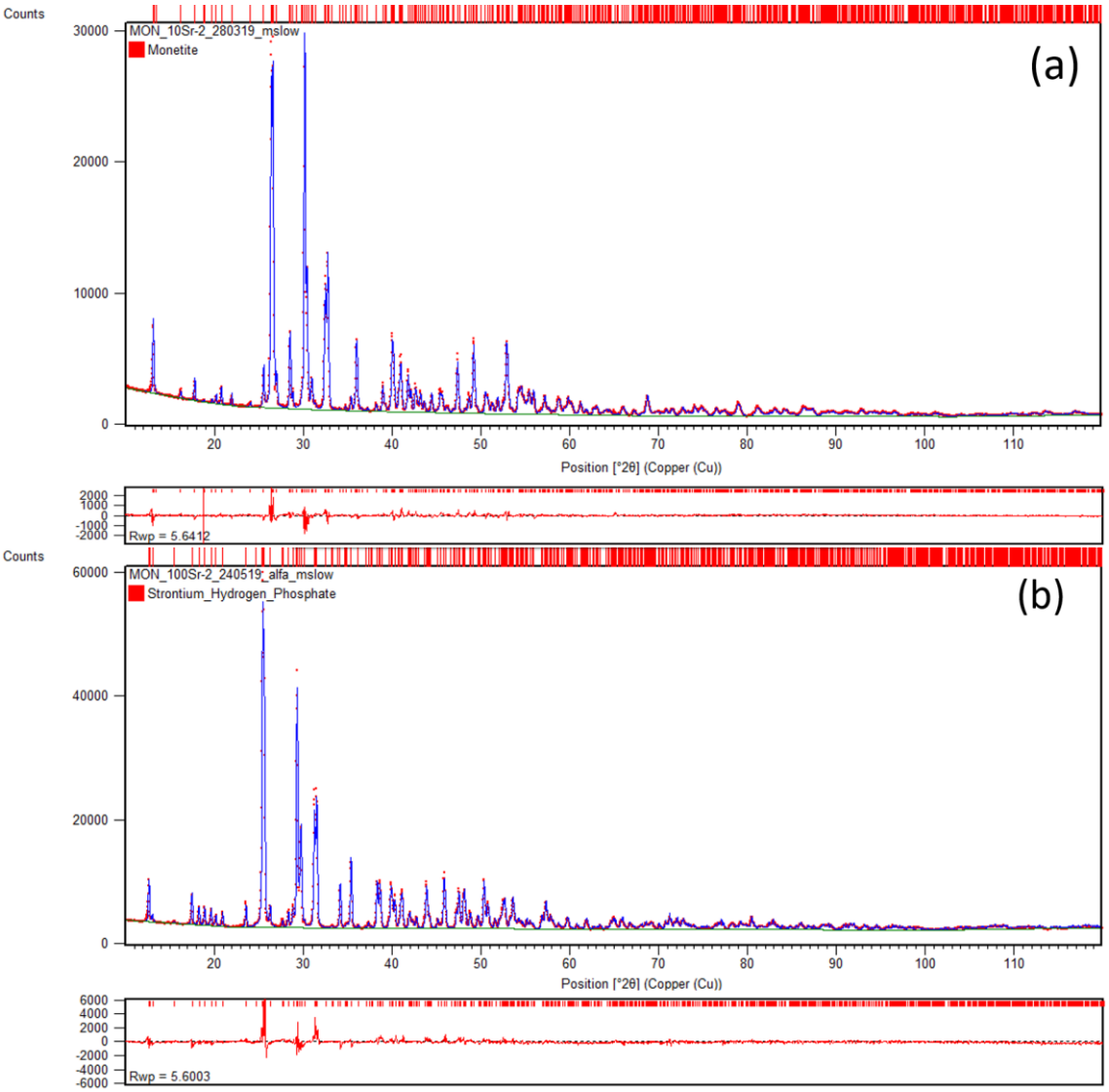

Figure 4.31 - Rietveld plot of (a) DS-10 and (b) DS-100 sample: refinement fit (blue line), experimental data (red dots). Difference plot Io-Ic is displayed at the bottom. Red vertical sticks represent the angular positions of the expected *hkl* reflections [*reproduced from Boanini, Gazzano, et al., 2021*].

The FTIR-ATR spectrum of DS-0 displays intense absorption bands at 1127, 1059 and 991, due to P–O stretching, and at 886 cm^{-1} related to P–O(H) stretching (Figure 4.32). Furthermore, P–O–H in plane bending gives the broad band between 1300 and 1450 cm^{-1}, whereas the absorption bands at about 559 and 523 cm^{-1} have been ascribed to O–P–O(H) bending mode [Tortet, 1997].

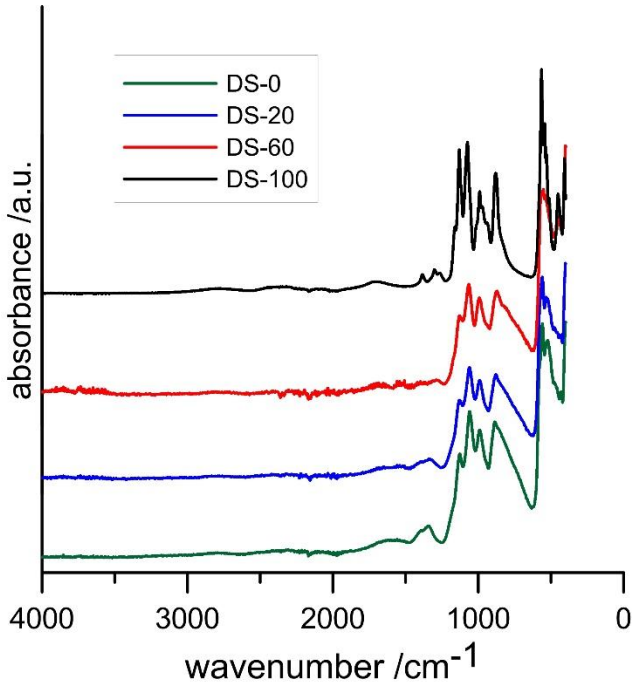

Figure 4.32 – FTIR-ATR spectra of samples obtained by direct synthesis.

At increasing Sr content, most absorption bands fall at increasing wavenumbers (Table 4.7). Moreover, the great relative intensity and the significantly greater sharpness of the absorption bands in the spectrum of DS-100 in comparison to the other samples, is in agreement with the high crystallinity of α- $SrHPO_4$.

Table 4.7 – Position of the main FTIR-ATR absorption bands in samples obtained by direct synthesis (cm^{-1}).

Sample	$P\text{-}O_{str}$			$P\text{-}O(H)_{str}$	$O\text{-}P\text{-}O(H)_{bend}$	
DS-0	1127	1059	991	886	559	523
DS-20	1129	1061	991	879	559	532
DS-40	1129	1061	991	873	556	535
DS-60	1129	1064	992	872	---	---
DS-100	1130	1074	992	---	565	543

SEM observations showed that monetite crystals are quite big and exhibit a layered morphology (Figure 4.33). The width of the crystals is about 5–10 μm and the thickness of the layers, which exhibit a smooth surface, is of 0.5–1 μm. The presence of strontium

seems to promote the trend of the crystals to exfoliate: the layers become more numerous and thin on increasing Sr content. Simultaneously, crystals fragmentation increases and some rod-like crystals detach from the layers up to DS-100, which displays only rod-like crystals with mean dimension of 5x0.5 μm (Figure 4.33).

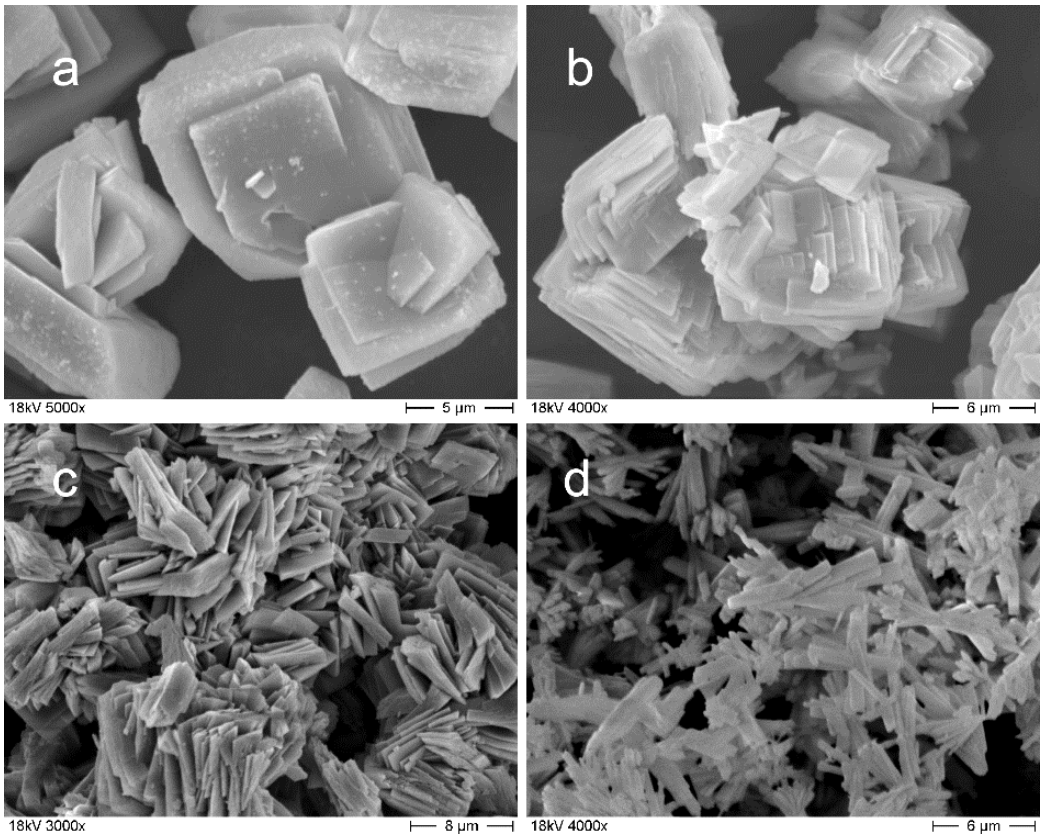

Figure 4.33 – SEM images of samples prepared by direct synthesis:
a) DS-0; b) DS-40; c) DS-60; d) DS-100.

In conclusion, the results of the direct synthesis of α-CaHPO4 samples indicate that strontium can replace calcium in the structure of DCPA in the whole range of composition up to the isomorph α-SrHPO4. The substitution, which is roughly quantitative, provokes a linear expansion of the cell parameters in agreement with the larger ionic radius of strontium than calcium, and a shift of the phosphate infrared absorption bands. Solid solutions of intermediate composition exhibit a reduction of the sharpness of the infrared absorption bands in comparison to those of the two end members. Moreover, strontium incorporation into DCPA structure implies a significant modification of the crystal morphology, from layered big crystals to much smaller rod-like crystals [Boanini, Gazzano, *et al.*, 2021].

1.4.2 Heat treatment

Differently for what happens for DCPA, strontium can't substitute for calcium into the structure of DCPD in the whole range of composition [Boanini, Silingardi, *et al*., 2021]. In fact, the synthesis of brushite in the presence of increasing Sr concentration in solution yields a unique crystalline phase up to a strontium concentration in solution of 60 at%, and corresponds to a Sr content of about 38 at% in the solid phase. Therefore, following this way of preparation of DCPA, complete substitution can't be reached.

DCPD loses its structural water molecules and converts into its anhydrous form, DCPA, by heat treatment at temperature higher than 180 ◦C [Rubini, 2019]. The comparison of the DSC curves of the DCPD samples synthesized at increasing Sr content clearly shows that the endothermic peak corresponding to the thermal conversion of DCPD into DCPA shift towards lower temperature on icreasing Sr content (Figure 4.34).

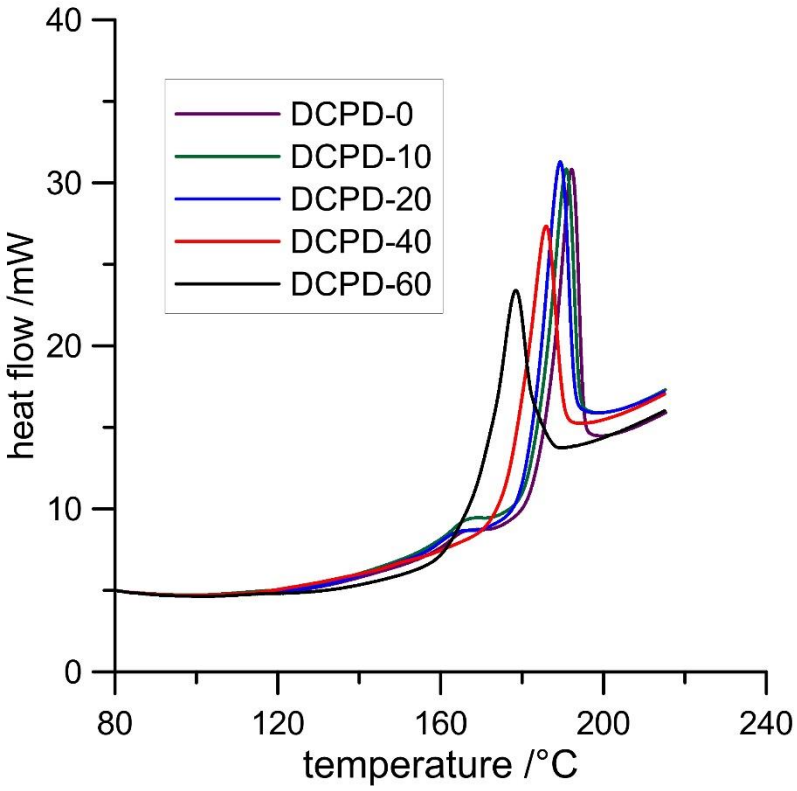

Figure 4.34 - DSC curves of the DCPD samples synthesized at increasing Sr content

The decrease of the associated enthalpy variation (ΔH) is due to the increase of molecular weight due to Sr substitution for calcium (Table 4.8).

Table 4.8 - Microcalorimetric data: DSC enthalpy variation and temperature of the endothermic transition from DCPD to DCPA; and TGA temperature of maximum weight loss corresponding to the removal of the water molecules from the structure of DCPD.

	DSC		TGA
Sample	ΔH (J/g)	T (°C)	T (°C)
DCPD-0	412	192	217
DCPD-10	410	191	216
DCPD-20	405	189	215
DCPD-40	400	186	213
DCPD-60	378	178	207

The decrease of DCPD thermal stability on increasing Sr content is confirmed by the results of thermogravimetric analysis. The weight loss corresponding to the removal of the two structural water molecules from pure DCPD occurs between 100 and 300 °C (Figure 4.35). The temperature of maximum weight loss speed gradually decreases from 217 ◦C to 207 °C (Table 4.8) on passing from DCPD-0 to DCPD-60.

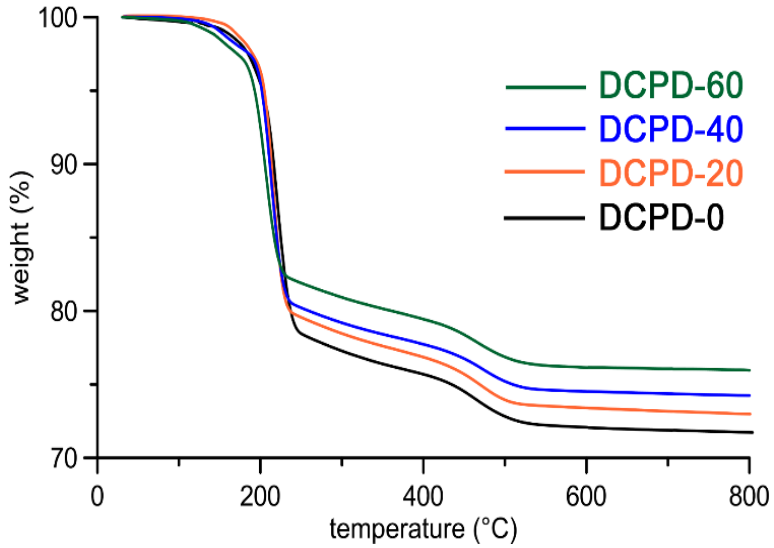

Figure 4.35 – TGA plots of the DCPD samples synthesized at increasing Sr content [*reproduced from Boanini, Gazzano, et al., 2021*]

The powder X-ray diffraction patterns of the products obtained through thermal treatment of the samples DCPD-0 to DCPD-60 show that DCPA is the unique crystalline phase (Figure 4.36).

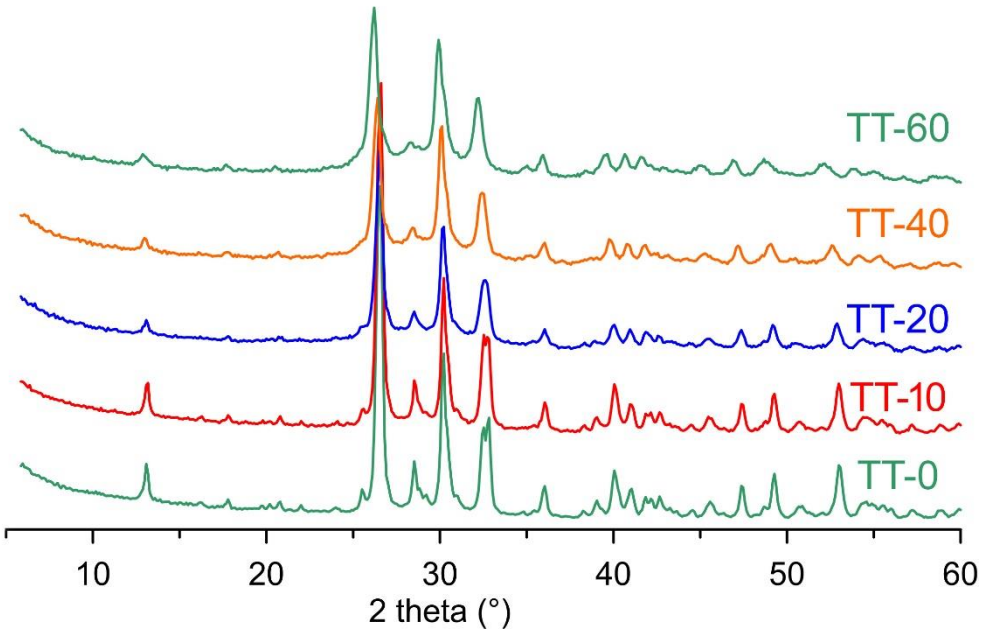

Figure 4.36 – XRD patterns of the DCPA samples synthesized by heat treatment.

The diffraction peaks present in the XRD patterns are definitely less sharp (Table 4.9) than those of the corresponding samples obtained by direct synthesis. Furthermore, the broadening of the peaks increases on increasing Sr content, suggesting a reduction of the dimensions of the coherent length of the perfect crystalline domains that is accompanied by a growing presence of amorphous material up to a value of about 30% in TT-60. Furthermore, the presence of Sr provokes a shift of the main diffraction peaks of monetite towards lower angles, in agreement with a partial substitution of Sr for Ca into DCPA structure. The results of the structural refinements show indeed an increase of the cell parameters on increasing Sr content (Table 4.9), with a similar trend to that observed for the samples obtained by direct synthesis.

Table 4.9 – Analytical and structural results for samples obtained after heat treatment of Sr-substituted DCPD [*reproduced from Boanini, Gazzano, et al., 2021*].

	Cell parameters*						
Sample	a (Å)	b (Å)	c (Å)	alfa(°)	beta(°)	gamma(°)	V (Å^3)
TT-0	6.914	6.644	7.000	96.2	104.0	88.4	310.25
TT-10	6.923	6.653	7.009	96.1	104.0	88.4	311.37
TT-20	6.932	6.653	7.022	96.0	104.1	88.4	312.40
TT-40	6.962	6.660	7.051	95.7	104.1	88.5	315.43
TT-60	7.020	6.688	7.096	95.4	104.6	88.6	321.03
	Occupation factor*		Sr content (at%)		X_c	τ_{hkl} (nm)**	
Sample	site 1	site 2	Rietveld	Chemical		τ_{001}	τ_{1-20}
TT-0	0.00	0.00	0	0	96	30	311
TT-10	0.06	0.04	5	4	90	27	304
TT-20	0.04	0.10	7	7	83	27	27
TT-40	0.09	0.20	15	18	73	24	26
TT-60	0.34	0.38	36	34	71	17	21

Notes: * estimated errors: a, b, c ± 0.002 Å, alfa, beta, gamma ±0.1°, V ± 0.1 Å^3, OF ±0.02.
** for τ_{1-20} relative to the couple 1 -2 0 / -1 -2 0 reflections.
X_c: crystallinity evaluated by the ratio $A_{cry}*100/(A_{cry} + A_{amo})$ where A_{cry} and A_{amo} are the crystalline and amorphous portion of the X-ray integrated intensity

The ATR-IR spectrum of DCPA obtained by thermal treatment of DCPD (TT-0) is very similar to that of the sample obtained by direct synthesis (Figure 4.37). Moreover, the samples at increasing Sr content show similar shifts of the absorption bands as those observed for the products of the direct synthesis.

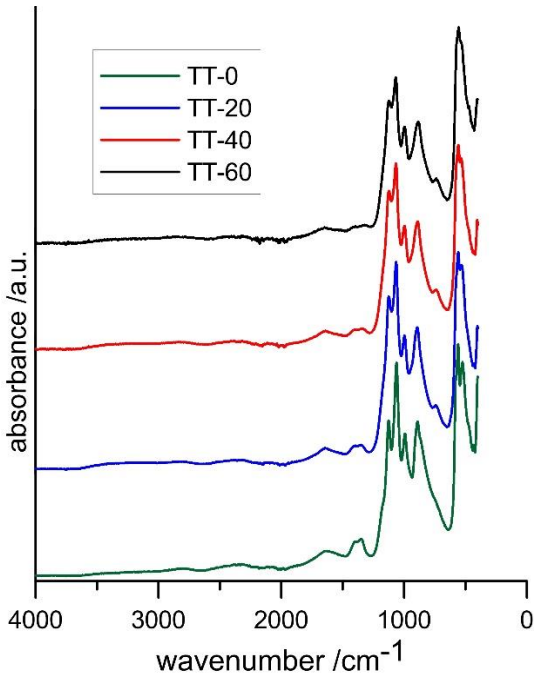

Figure 4.37 – FTIR-ATR spectra of TT samples, at increasing Sr content.

The morphologies of the TT samples resemble those of the corresponding DCPD samples before heat treatment. In particular, the SEM image of TT-0 shows the presence of plate-like crystals, with a morphology very similar to that characteristic of DCPD-0 [Boanini, Silingardi, *et al.*, 2021]. The images of samples at increasing strontium content confirm that the foreign ion promotes aggregation of the crystals, that become smaller and thicker (Figure 4.38).

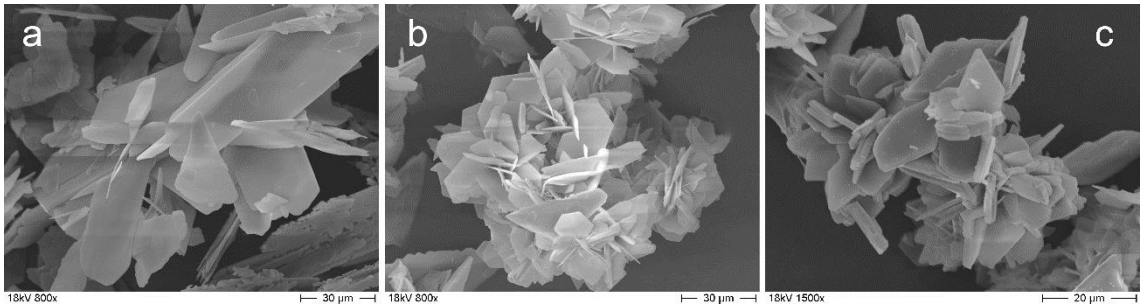

Figure 4.38 - SEM images of TT samples obtained after thermal treatment:
a) TT-0; b) TT-40; c) TT-60.

In conclusion, at variance with direct synthesis procedure, the range of strontium substitution in monetite samples synthesized through thermal treatment of DCPD samples is driven by the limited capacity of brushite structure to host strontium, which provokes a reduction of DCPD thermal stability. TT samples show structural variations due to strontium incorporation similar to those observed for DS samples, whereas they maintain a morphology resembling that of DCPD and confirm the tendency to crystal aggregation induced by Sr incorporation.

1.4.3 Calcium substitution in the structure of β-$SrHPO_4$

In addition to the α-form of $SrHPO_4$, which is isomorphous with monetite, two further polymorphs have been reported in the literature, namely β- and γ-$SrHPO_4$. The structure of this β form has not been resolved up to now. However, several methods of synthesis and different applications, including as drug carrier and as support for Pb^{2+} immobilization, have been reported [Roming, 2008; Lu, 2017]. Herein, crystal structure of β-$SrHPO_4$ has been solved and the possibility to host calcium replacement to strontium has been explored.

To this aim, the same synthesis used for the α-form has been carried out at 5 °C. In the presence of strontium as only cation; the synthesis yields β-$SrHPO_4$ as single crystalline

phase (ICDD file 12–368), as shown by the XRD pattern (Figure 4.39a). SEM image shows that pure β-$SrHPO_4$, β-100 is constituted of clusters of thin flaky crystals (Figure 4.39b).

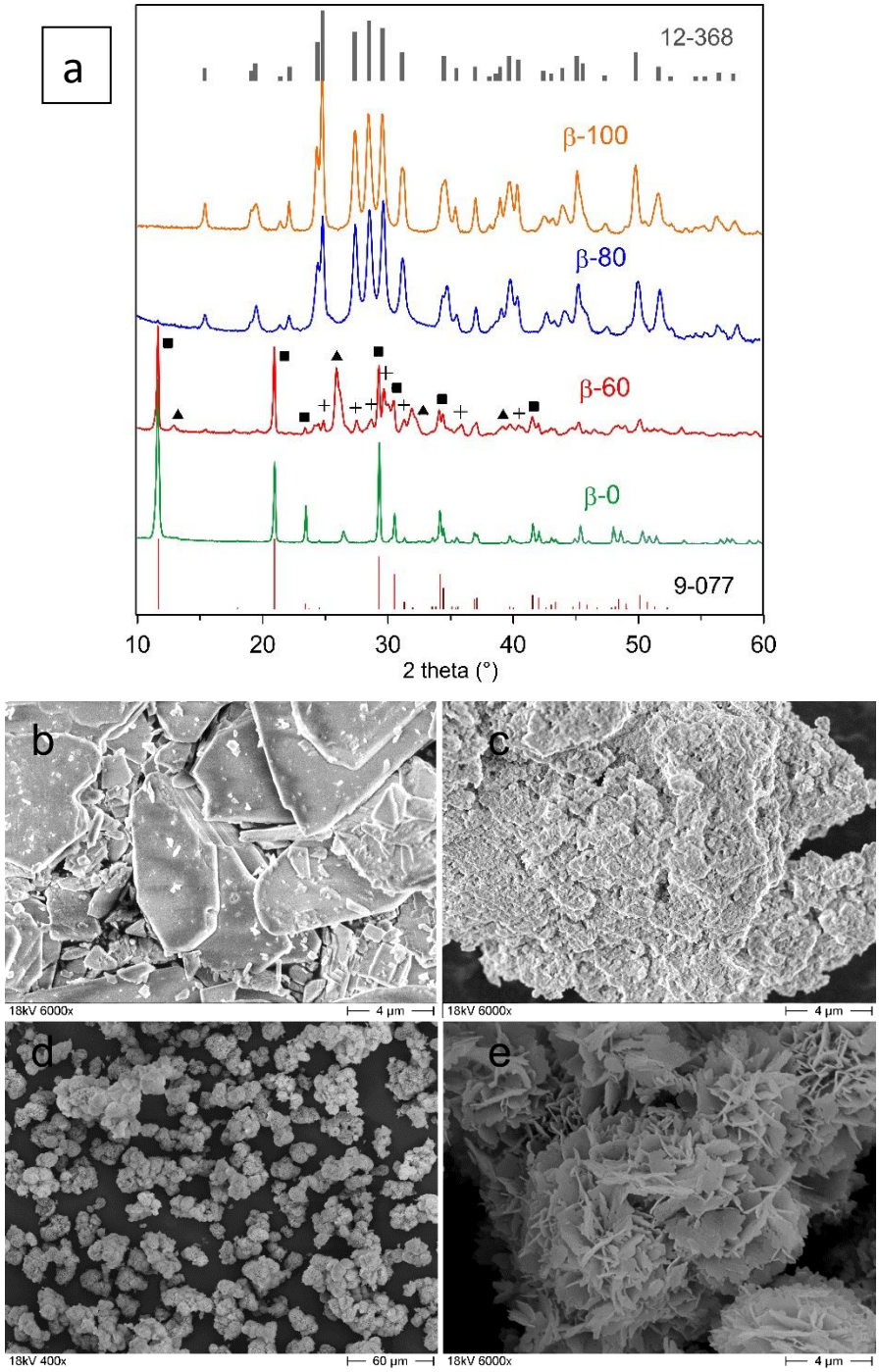

Figure 4.39 - XRD patterns (a) and SEM images of samples obtained at low temperature: (b) β-0; (c) β-80; (c, d) β-100. In (a) the reference lines of β-$SrHPO_4$ (ICDD file 12–368) and DCPD (ICDD file 9–077) are reported. Symbols in β-60 indicate the presence of (■) monetite; (+) β-$SrHPO_4$ and (▲) α-$Sr_2P_2O_7$.

At variance with what found for the α-polymorph, this structure does not seem to tolerate relatively great amount of calcium ion incorporation. In fact, the products of synthesis performed in the presence of increasing calcium concentration in solution are constituted by a single crystalline phase just up to β-80 (Sr content: 72 at%), whereas greater Ca concentrations provoke the precipitation of secondary phases (Figure 4.39a). Calcium substitution for strontium in β-80 provokes a reduction of lattice parameters (*a* = 10.197(3) Å, *b* = 7.954(4) Å, *c* = 9.303(3) Å, β = 116.95(5)°, V = 672.6(5) Å^3), and a remarkable morphological modification: it is constituted of a multitude of very small crystals (mean dimension smaller than 100 nm) clustered together in aggregates of undefined shape (Figure 4.39). Interestingly, β-0, obtained through synthesis carried out in the same experimental conditions, but in the complete absence of Sr, is constituted of DCPD as unique crystalline phase (Figure 4.39a) confirming the inhibiting effect of calcium on β-$SrHPO_4$ structure. Figure 4.39b shows that β-0 exhibits the typical plate-like morphology of DCPD [Rubini, 2019].

The ATR-IR spectra of both β-100 and β-80 exhibit a number of absorption bands in the regions characteristic of P–O and P–OH stretching and bending modes (Figure 4.40).

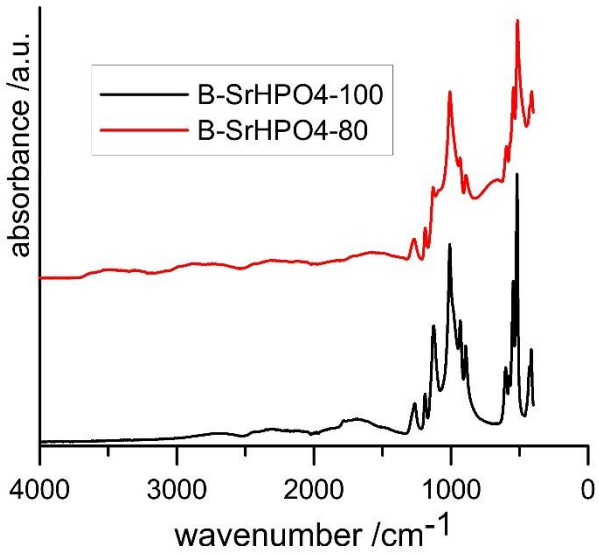

Figure 4.40 – FTIR-ATR spectra of samples obtained at low temperature.

1.4.4 Structure of β-$SrHPO_4$

Since the structure of β-$SrHPO_4$ has not been solved up to now, the pattern of β-100 sample was indexed as a monoclinic cell with parameters *a* = 10.239(2) Å, *b* = 7.9992(17) Å, *c* = 9.326 (2) Å, β = 116.770 (4)°, V = 682.0(3) Å^3, space group P21/c (n. 14), and atoms positioned from powder data. The final Rietveld plot is reported in Figure 4.41 and final atomic parameters are reported in Table 4.10 (file CSD2069793).

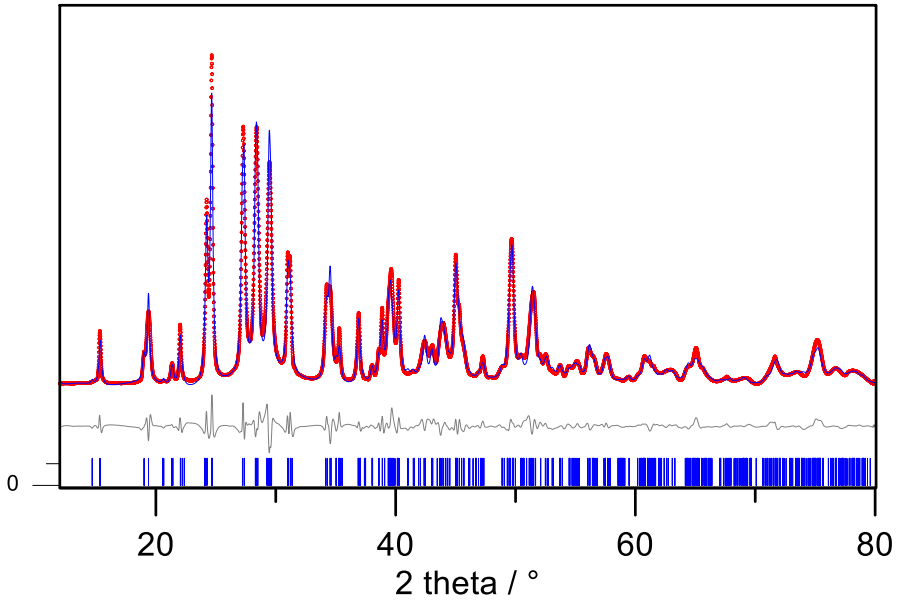

Figure 4.41 – Rietveld plot for β-SrHPO4: refinement fit (blue line) against experimental data (red dots). Differential plot (gray line) between observed and calculated intensity. Blue vertical sticks represent the angular positions of the expected *hkl* reflections [*reproduced from Boanini, Gazzano, et al., 2021*].

Table 4.10 - Crystallographic coordinates for β-$SrHPO_4$ [*reproduced from Boanini, Gazzano, et al., 2021*].

Label	Element	Site multiplicity	X	Y	Z	Occupation factor	B_{iso}
Sr1a	Sr	4	-0.7472(6)	-0.6339(9)	0.5653(6)	1	3
Sr1b	Sr	4	-0.7369(5)	-0.3670(8)	0.2019(6)	1	3
P1a	P	4	-0.9194(15)	-0.024(2)	0.3148(19)	1	3
O1a	O	4	-0.961(6)	-0.182(5)	0.398(5)	1	3
O2a	O	4	-0.827(4)	-0.105(8)	0.239(5)	1	3
O3a	O	4	-0.830(6)	0.100(8)	0.451(7)	1	3
O4a	O	4	-1.066(6)	0.055(12)	0.194(8)	1	3
P1b	P	4	-0.501(2)	-0.2455(15)	0.5668(18)	1	3
O1b	O	4	-0.650(5)	-0.345(7)	0.545(6)	1	3
O2b	O	4	-0.485(8)	-0.070(4)	0.667(5)	1	3
O3b	O	4	-0.503(10)	-0.215(7)	0.401(5)	1	3
O4b	O	4	-0.346(7)	-0.343(12)	0.676(9)	1	3

The asymmetric unit consists of two Sr atoms and two hydrogen phosphate groups. The structural arrangement, as seen along *c*-axis (Figure 4.42) consists of alternate phosphate layers, P1a and P1b, parallel to b,c plane and spaced by Sr atoms. The environment of Sr1a is an irregular polyhedron with oxygen at height vertex at distances within 2.36 ÷ 2.86 Å. Sr1b is nine-coordinated at distances in the range 2.38–2.91 Å with geometry reminiscent of a pentagonal bipyramid in which the two apexes are substituted by a phosphate edge (Figure 4.42). Coordination arrays of Sr polyhedral are parallel to b,c plane. The presence of nine-coordinated cationic site can justify the difficulty of calcium, which usually prefers smaller coordination numbers, to enter this structure in relevant amount.

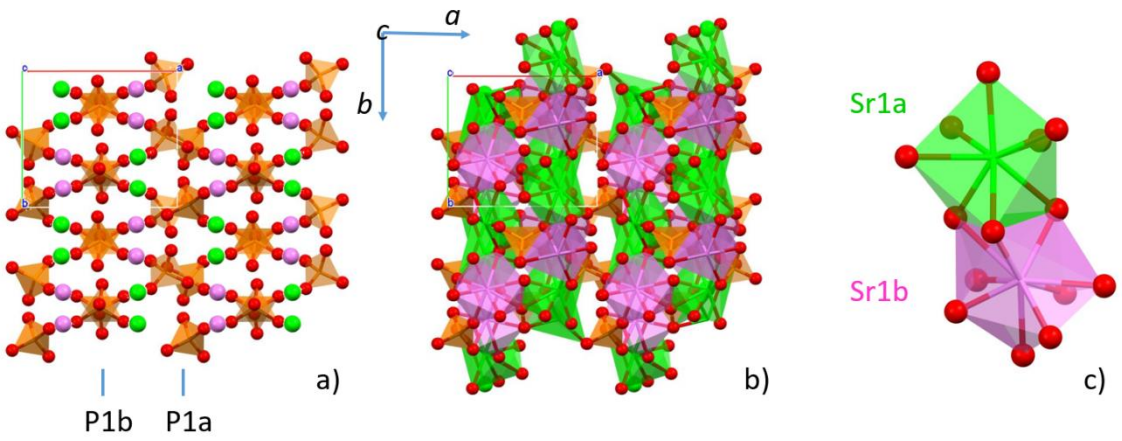

Figure 4.42 – (a) and (b) Views of β-SrHPO4 crystal structure down *c*-axis; and (c) environments of Sr atoms [*reproduced from Boanini, Gazzano, et al., 2021*].

In conclusion, powder X-ray analysis of β-$SrHPO_4$ synthesized at low temperature provided detailed information on its crystal structure, which had not been resolved up to now. This polymorph crystallizes in a monoclinic cell, space group $P2_1/c$ (n. 14), where strontium occupies two independent sites. No calcium isomorph of this structure is known. In this thesis work it has been demonstrated that calcium substitution to strontium into β-$SrHPO_4$ occurs just up to about 20%, whereas higher calcium concentrations in the synthesis solution provoke the precipitation of secondary phases [Boanini, Gazzano, *et al*., 2021].

1.5 Ionic substitution of strontium and zinc in the structure of β-TCP.

β-tricalcium phosphate (β-TCP, $Ca_3(PO_4)_2$) is one of the calcium phosphates widely applied in bone cements and implants. Its properties can be modified by functionalization with foreign ions. Herein, this thesis reports the results about the structural modifications induced on β-TCP structure by functionalization with biologically active ions, namely strontium and zinc. Strontium is known to exert a beneficial action in the treatment of diseases characterized by abnormally high bone resorption, such as osteoporosis [Bonnelye, 2008]; zinc has been shown to inhibit osteoclast proliferation [Shepherd, 2014] and to display antibacterial properties [Sutha, 2013].

1.5.1 Strontium substitution

XRD patterns of all the products of synthesis in the presence of strontium (up to a Sr^{2+} content of 80 at%) show the presence of β-TCP as a unique crystalline phase (Figure 4.43).

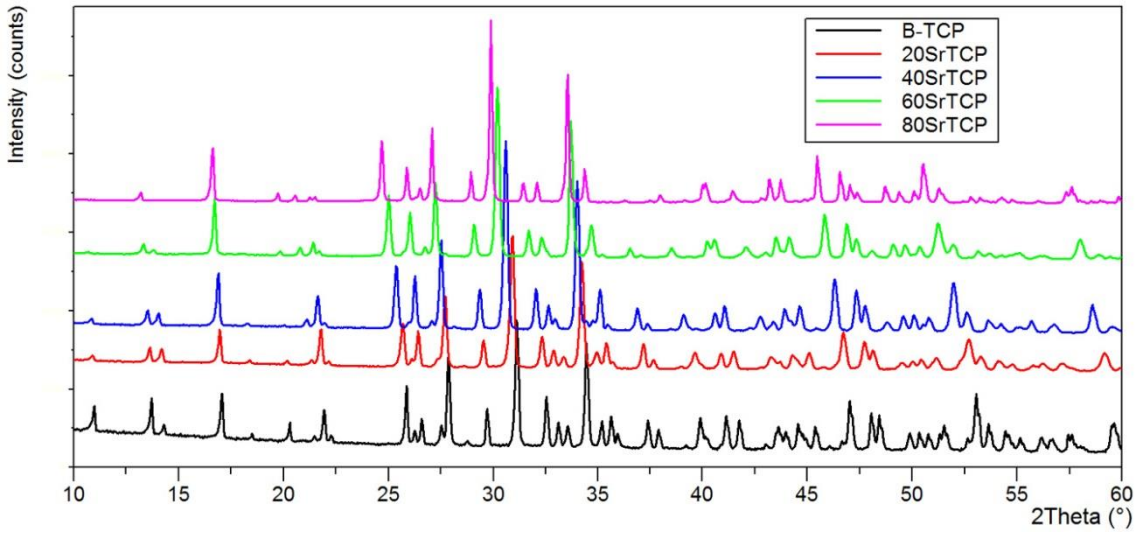

Figure 4.43 – XRD patterns of strontium-substituted samples compared with pure β-TCP. The the peaks shift toward lower angles is evident on increasing Sr.

The evident peaks shift towards lower angles on increasing the Sr content is in agreement with the substitution of the bigger cation (radius 0.118 nm) to the smaller Ca (0.100 nm).

The structural refinements were performed by the Rietveld method [Young, 1993] starting from the atomic position set of β-TCP in space group R3c (n. 161) [Yashima, 2003]. To limit the number of free variables (the asymmetric unit contains five calcium, three phosphorus and ten oxygen atoms) we used a rigid body model with constraints to maintain the same geometry of phosphate tetrahedra as in pure β-TCP. Phosphorus atom positions were kept free to move in accordance with the symmetry rules of the crystal system. Graphical plots of the refinements of samples 10SrTCP and 60SrTCP arereported in Figure 4.44 as examples.

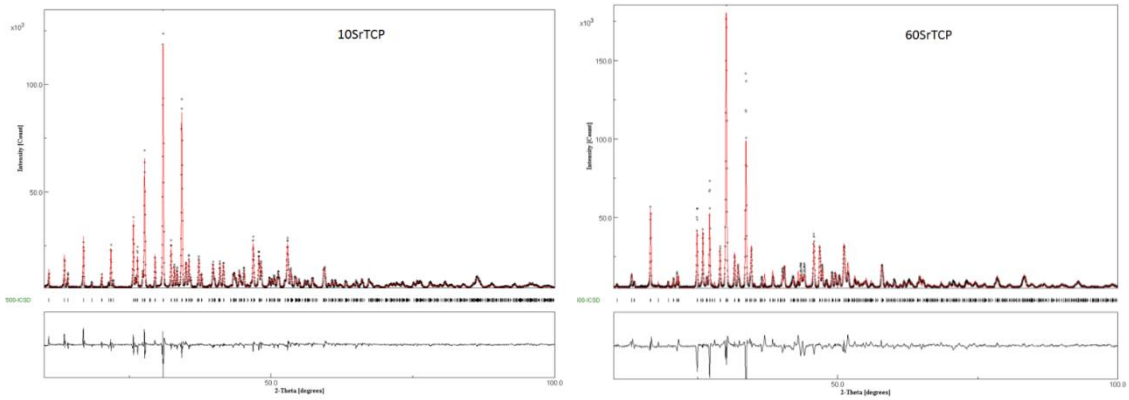

Figure 4.44 – Rietveld comparison of the observed (dots) and calculated (red) XRD patterns of 10SrTCP and 60SrTCP. At the bottom reflection markers and curve difference content [*reproduced from Boanini, 2019*].

In order to improve the fit, 80SrTCP structure was refined using a somewhat different starting model, namely the structure of β'-TCP. This structure0 (R-3m) was previously reported to occur as a thermal phase transition of β -TCP promoted by strontium [Belik, 2002]. β'-TCP structure is topologically similar to β -TCP, the main difference being the presence of a symmetry center that implies a unit cell with half *c*-axis and volume. Refinement of 80SrTCP using as a model the structure of β'-TCP indeed gives a better fitting: Figure 4.45 shows the comparison between the two final plots of Rietveld refinements for 80SrTCP obtained using the two different structural models.

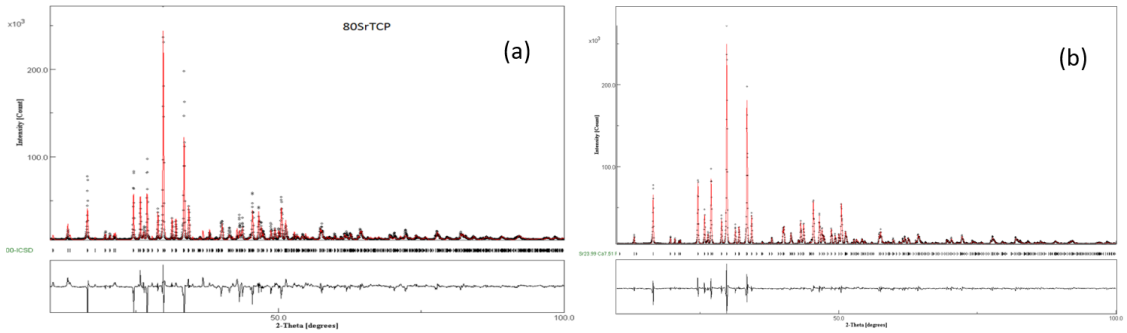

Figure 4.45 - Comparison of the observed (dots) and calculated (red) XRD patterns of 80SrTCP. Refinement carried out on (a) the β-TCP setting and (b) the β'-TCP setting. At the bottom reflection markers and difference curve content [*reproduced from Boanini, 2019*].

The relevant structural parameters obtained through the Rietveld analysis are reported in Tables 4.11 and 4.12. The variation of the unit cell parameters as a function of Sr content has a strictly linear trend and fits well with previously reported data [Bigi, 1997]. The overall strontium contents resulting from the refinements with no imposed constraints are very close to the analytical ones.

Table 4.11 - Lattice parameters of β-TCP in samples synthesized at different Sr content.

	β-TCP	**10SrTCP**	**20SrTCP**	**40SrTCP**	**60SrTCP**	**80SrTCP**
a (Å)	10.4387 (1)	10.4578(2)	10.4897(2)	10.5773(2)	10.6525(4)	10.6996(2)
c (Å)	37.3979 (6)	37.421(1)	37.599(1)	38.189(1)	38.708(2)	39.226(1)
V(Å^3)	3529	3543	3583	3700	3804	3889

[1] Parameters based on β'-TCP setting are: a=10.6996(2) Å, c=19.613(1) Å, V=1945 Å^3.

Table 4.12 - Refined structural parameters for SrTCP samples

	M [1]	**10SrTCP**	**20SrTCP**	**40SrTCP**	**60SrTCP**	**80SrTCP**
	OF Sr *atoms/cell*					
M(1)	18	0.0 *10*	0.10 *1.8*	0.34 *6.1*	0.62 *11.2*	0.73 *13.1*
M(2)	18	0.05 *0.9*	0.09 *1.6*	0.33 *6.0*	0.68 *12.2*	0.83 *15.0*
M(3)	18	0.17 *3.06*	0.40 *7.2*	0.68 *12.2*	0.67 *12.1*	0.80 *14.4*
M(4) [2]	6	0.32 *1.92*	0.40 *2.4*	0.41 *2.4*	0.41 *2.4*	0.43 *2.6*
M(5)	6	0.00 *0*	0.00 *0*	0.01 *0*	0.01 *0*	0.01 *0*
Sr at. / cell [3]		*5.88*	*13.0*	*26.7*	*37.9*	*45.1*
Sr at. % [4]		9.4	20.6	42.2	60.0	71.4
Rwp (%)		6.3	6.6	12.7	13.8	17.9

[1] multiplicity of crystal site; [2] the overall content of site 4 is 0.43; [3] total metal atoms inside unit cell are 63.2; [4] from refinement.

Results of powder fitting refinements indicate that at low degree of substitution strontium displays the highest OF in M(4) site, followed by M(3) site; as the overall substitution degree increases, the filling of sites M(1) and M(2) become important, too. It is worth mentioning that in the whole range of investigated composition (strontium up to 80 at%), site M(5) is not occupied by Sr atoms. The 'filling' of calcium sites by strontium starting from M(4) and M(3) is also due to a geometrical reason. β-TCP structure can be described as a regular assembly of two kinds of columns in which Ca atoms and phosphate tetrahedra are stacked. As shown in Figure 4.46, the unit cell view down *c*-axis allows to identify A-type columns filled with Ca(4), Ca(5) and P(1) whereas B-type columns contain Ca(1), Ca(2) Ca(3) and P(2) and P(3). A-type columns are surrounded only by B-type ones. At first strontium enters into Ca(4), causing a significant expansion of c-axis. Further strontium substitution for calcium is better accommodated in the other column to compensate the increment along the c-axis.

Moreover, the preference of strontium for sites M(4) and M(3) can be ascribed to the most favorable distances found in these sites, which can accommodate bigger ions than calcium. Mean Ca-O distances in β-TCP are: Ca(1)-O 2.505 Å, Ca(2)-O 2.487 Å, Ca(3)-O 2.601 Å, Ca(4)-O 2.936 Å, Ca(5)-O 2.263 Å. Ca-O environments exhibit the longest mean distance in site M(4) content [Boanini, 2019].

Mean M(3)-O distance is second just to M(4)-O and any further increments in Sr content can be easily accommodated here, also due to its higher storage ability than M(4): the unit cell contains less than 3 M(4) type atoms vs. 18 atoms of the M(3) type. On the other hand, location of strontium in site M(5) is strongly unfavorable since the mean M(5)-O distance is the shortest. Furthermore, the range of M-O bond values in each site should also play a role: M(4) shows the shorter contact at 2.53 Å, M(5) at 2.21 Å and all the other sites at values greater than 2.30 Å [Yashima, 2003]. These data agree with the preference of strontium for site M(4) reported previously on β-TCP samples containing small amount of strontium [Nandha Kumar, 2013; Kannan, 2010], and demonstrate that the preference is maintained also at much higher strontium content. In fact, the results obtained for the sample 80SrTCP indicate the same preference both when the refinement is performed using the structure of β-TCP [Yashima, 2003] and that of β'-TCP [Belik, 2002].

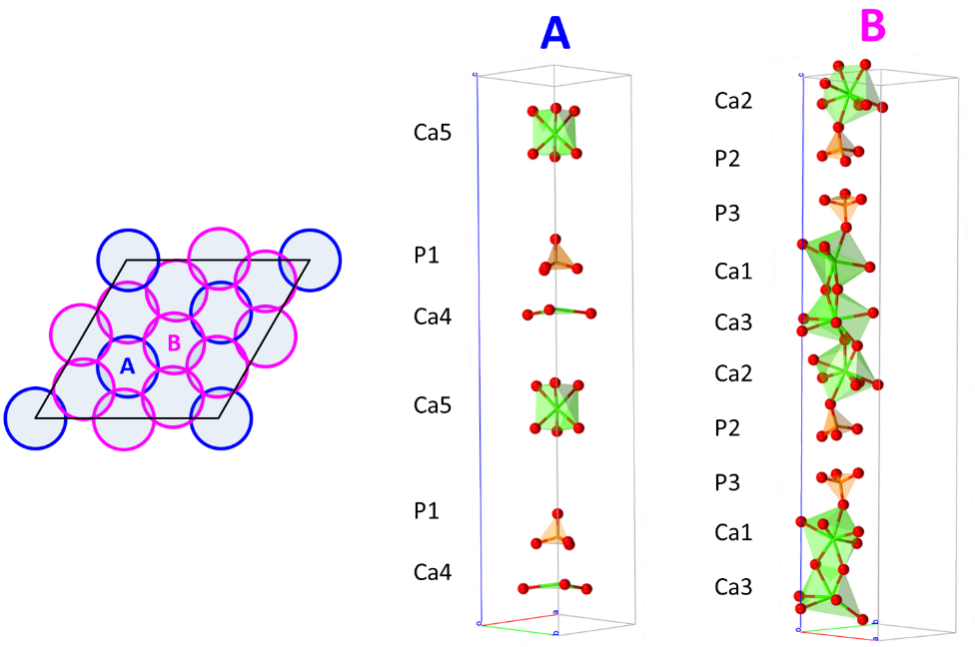

Figure 4.46 - **Left**, view of the columns in β-TCP unit cell down the *c*-axis. **Right**, a view of the atoms that characterize A- and B-type columns.

The samples prepared in the presence of strontium show the characteristic morphology of a solid-state reaction product and do not seem to be significantly affected by the presence of a low amount of Sr, whereas the products synthesized at high Sr content appear to be constituted of more dense blocks (Figure 4.47).

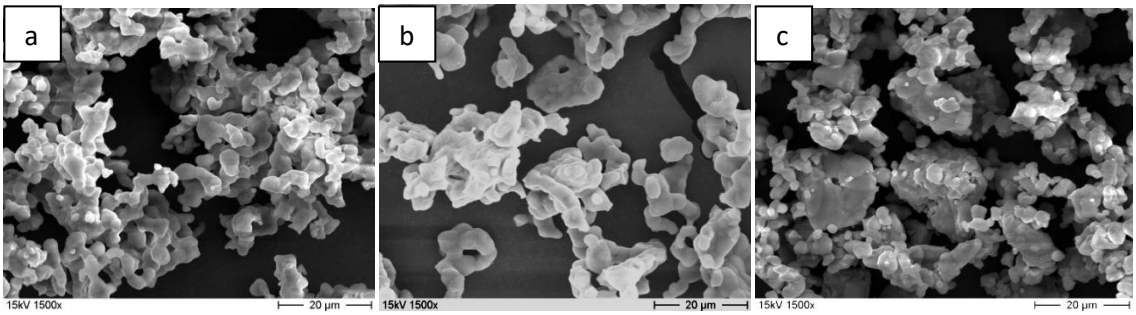

Figure 4.47 – SEM images of (a) β-TCP; (b) 20SrTCP and (c) 80SrTCP samples.

The ^{31}P isotropic chemical shift is very sensitive to local structural modifications, thus providing a reliable probe for this class of samples. The ^{31}P MAS NMR spectrum of pure β-TCP (Figure 4.48) is characterized by three main broad resonances at 4.9 (P2), 1.5 (P2) and 0.3 (P3) ppm and three shoulders at 2.6, 0.8 and -0.5 ppm assigned to P1, P3 and P1, respectively. Even for a very low substitution of Ca with Sr in the β-TCP

structure, the ^{31}P resonances change in terms of chemical shift and line width (Figure 4.48).

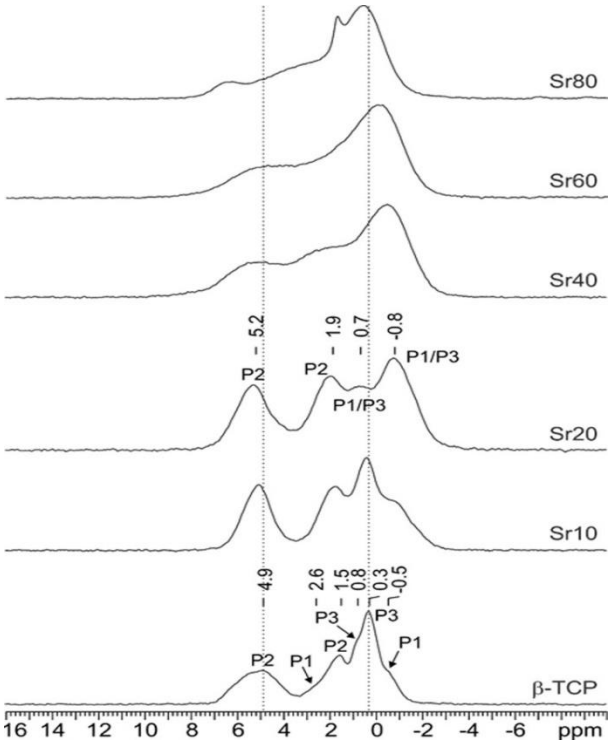

Figure 4.48 - ^{31}P (242.95 MHz) MAS spectra of β-TCP (with relevant assignment), and SrTCP samples content [*reproduced from Boanini, 2019*]

The infrared absorption spectrum of β-TCP shows a number of bands due to the vibration of the phosphate groups. Infrared and Raman studies identified the bands due to the symmetric stretching ν1 (940–980 cm^{-1}), the triple-degenerate asymmetric stretching ν3 (1000–1100 cm^{-1}), and the double and triple-degenerate bending ν2 (400–500 cm^{-1}) and ν4 (550–600 cm^{-1}) [Jillavenkatesa, 1998]. Sr substitution provokes an increasing degeneracy and a general shift of the bands towards lower wavenumbers. This is particularly evident for the ν1 band which shifts from 943 cm^{-1} in the spectrum of β-TCP to 936 cm^{-1} in the sample at the highest Sr content (Table 4.13 and Figure 4.49). In the Raman spectrum of β-TCP this band was ascribed to P(1), the band at about 968 cm^{-1} was assigned to P(3), whereas the intermediate band, not appreciable in the FTIR-ATR spectrum, was assigned to P(2) [Quillard, 2011]. P(1) and P(2) are close to Ca(4); in particular P(1) and P(2) tetrahedra share a common face and an edge, respectively, with Ca(4) site [Yashima, 2003], whereas P(3) is not in the close vicinity of Ca(4). It follows that the shift of the 943 cm^{-1} band at lower wavenumbers on increasing Sr substitution is consistent with its preferential occupancy of Ca(4) site.

Table 4.13 - ATR-FTIR bands wavenumbers (cm^{-1}) content [*reproduced from Boanini, 2019*].

	β–TCP	10SrTCP	20SrTCP	40SrTCP	60SrTCP	80SrTCP
ν3	1116 1078 1037 1000	1114 1075 1041 1002	1112 1039 1005	1109 1036 1006	1108 1053 1033 984	1112 1070 980
ν1	968 943	967 940	970 939	971 937	 936	 936
ν4	604 589 579 570 550 541	602 587 577 567 550 541	600 586 575 566 550 541	597 586 540	595 586 539	 588 567 537

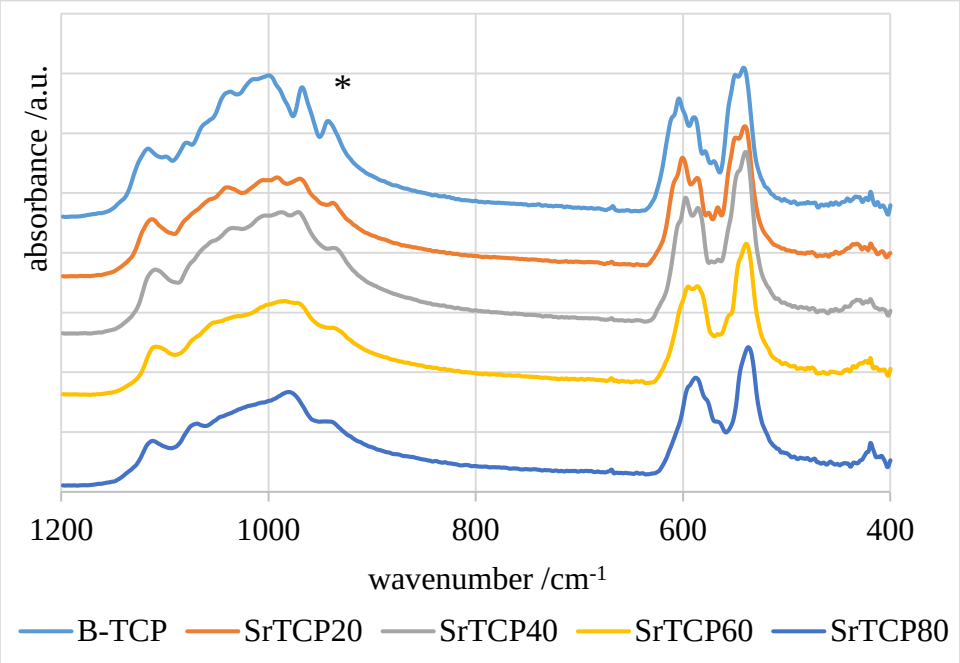

Figure 4.49 - ATR-FTIR spectra of β-TCP at different Sr content. The asterisk * indicates the ν1 band at 943 cm^{-1} in the spectrum of β-TCP.

1.5.2 Zinc substitution

The amount of Zn that can be hosted by the structure of β-TCP is noticeably lower than that of Sr. In fact, only the XRD patterns of the samples synthesized in the presence of 5 and 10 Zn at% are in agreement with the presence of a unique crystalline phase, whereas at a higher Zn concentration further peaks indicate the presence of a secondary phase (Figure 4.50).

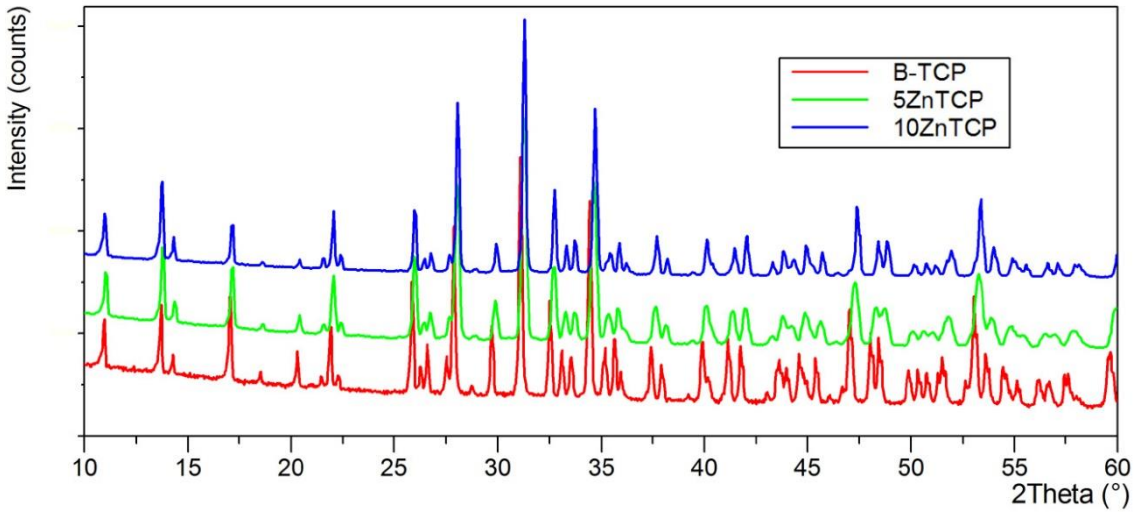

Figure 4.50 - XRD patterns of zinc-substituted samples compared with unsubstituted β-TCP.

Moreover, the Zn ion, due to its smaller ionic radius (0.075 nm) than calcium, shows also a different structural behavior in comparison to Sr ion. The results of the refinements (Figure 4.51) show that zinc is distributed over all the sites in ZnTCP at a low substitution degree (5%), but M(5) becomes the preferred site when zinc content increases (10%). The octahedral coordination geometry and short distances of M(5) are indeed particularly suitable for the little zinc ion (Table 4.14). Probably due also to the limited substitution range, ZnTCP does not present any discontinuity in cell parameters (Table 4.15).

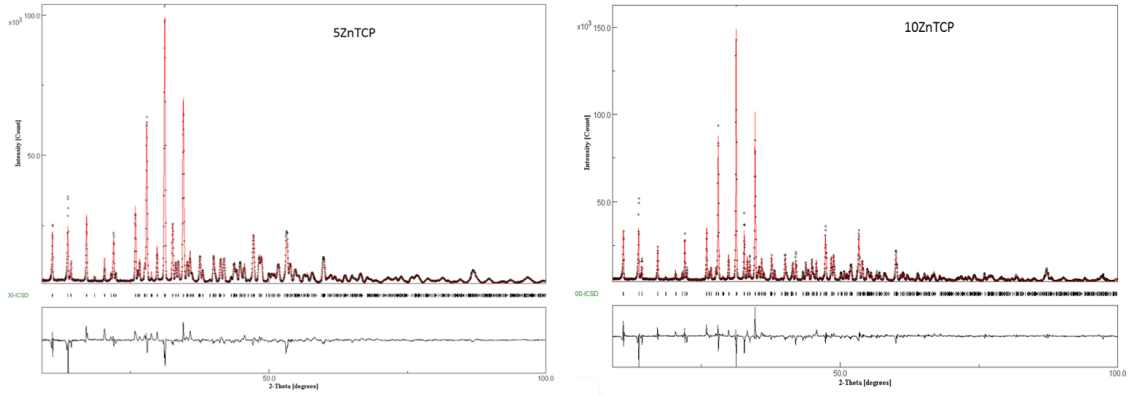

Figure 4.51 – Rietveld refinement plots showing the observed (dots) and calculated (red) XRD patterns of 5ZnTCP and 10ZnTCP. At the bottom reflection markers and curve difference.

Table 4.14 - Refined structural parameters for ZnTCP samples

	M [1]	**5ZnTCP**		**10ZnTCP**	
		OF Sr *atoms/cell*			
M(1)	18	0.05	*0.9*	0.03	*0.5*
M(2)	18	0.07	*1.3*	0.07	*1.2*
M(3)	18	0.07	*1.3*	0.08	*1.4*
M(4) [2]	6	0.05	*0.0*	0.03	*0.0*
M(5)	6	0.15	*0.9*	0.97	*5.8*
Sr at. / cell [3]		*4.4*		*8.9*	
Sr at. % [4]		7.0		14.1	
Rwp (%)		7.4		8.9	

[1] multiplicity of crystal site; [2] the overall content of site 4 is 0.43; [3] total metal atoms inside unit cell are 63.2; [4] from refinement.

Table 4.15- Lattice parameters of β-TCP in samples synthesized at different zinc content.

	β-TCP	**5ZnTCP**	**10ZnTCP**
a (Å)	10.4387 (1)	10.3820(3)	10.3364(2)
c (Å)	37.3979 (6)	37.247(1)	37.1262(9)
V(Å^3)	3529	3477	3435

The samples synthesized in the presence of Zn appear to be constituted of more dense blocks in comparison to reference β-TCP, but they retain the characteristic morphology of a solid-state reaction product (Figure 4.52).

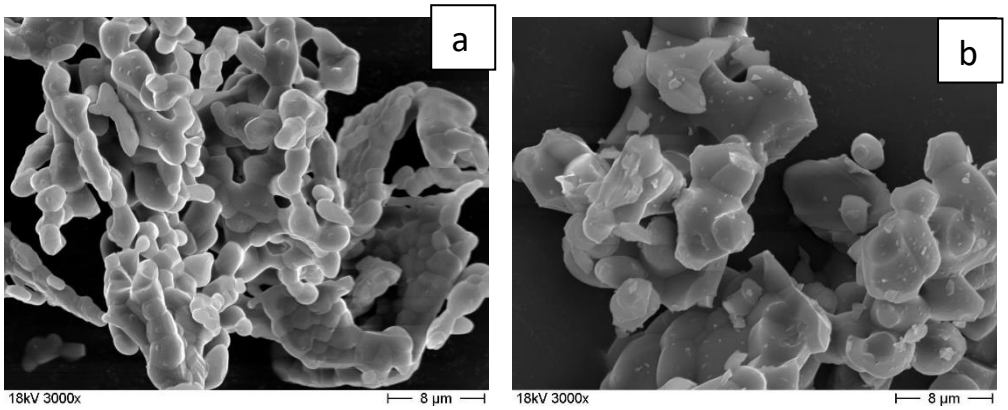

Figure 4.52 - SEM images of (a) β-TCP and (b) 10ZnTCP samples.

Even for a very low substitution of Ca with Zn in the β-TCP structure, the ^{31}P resonances change in terms of chemical shift and line width (Figures 4.53). In particular, the broadening observed in the substituted samples suggests a random substitution of the foreign ion for calcium. As previously discussed, XRD data indicate that Zn substitution takes place preferentially on the M(5) site, which is surrounded by the P2 and P3 phosphorus sites [Yashima, 2003]. The comparison among the ^{31}P MAS NMR spectrum of β-TCP and those of the ZnTCP samples confirms XRD results. In particular, ZnTCP spectra (Figure 4.53) show a low-frequency shift (about 1 ppm) and a drastic narrowing (FWHM from ~530 to ~195 Hz) of the P2 signal at 4.9 ppm. The P3 signal, at 0.3 ppm displays a minor shift toward higher frequencies, up to 0.6 ppm.

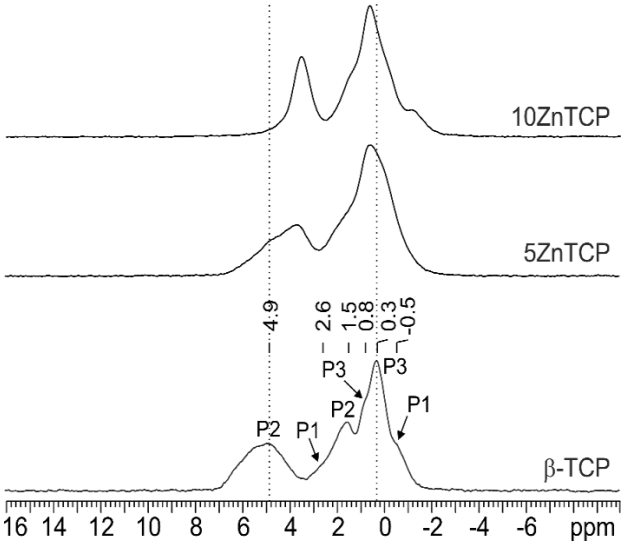

Figure 4.53 - ^{31}P (242.95 MHz) MAS spectra of β-TCP (with relevant assignment), and ZnTCP samples [*reproduced from Boanini, 2019*]

These data concerning zinc and strontium substituted TCP in the whole are in good agreement with those previously reported for β-TCP doped with aluminum, gallium and sodium, which showed that that ions bigger than calcium (Na) preferentially enter site (4), and those with shorter radius (Al, Ga) substitute calcium at site (5) [Grigg, 2014].

Incorporation of zinc into β-TCP structure induces a significantly increased degeneracy of the infrared absorption bands (Figure 4.54), in agreement with previously reported data [Bigi, 1997], which suggests an increasing structural disorder.

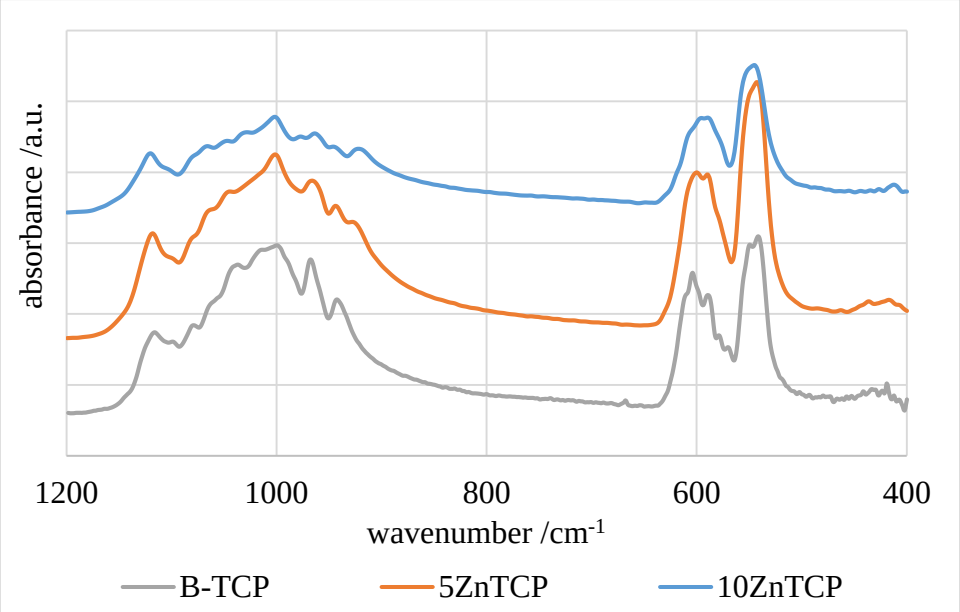

Figure 4.54 - ATR-FTIR spectra of β-TCP at different Zn content.

In conclusion, in this work β-TCP samples were prepared at increasing contents of zinc or strontium. XRD data show that Zn-TCP can be prepared as a single phase up to a zinc content of about 10 at%, whereas a much wider range of substitution, up to about 80 at%, has been obtained for strontium. The results of Rietveld refinements indicate that Zn occupies preferentially the octahedral Ca(5) site, whereas it does not show any preference for the Ca(4) site, as previously suggested [Gomes, 2011]. Zinc substitution provokes a reduction of the cell parameters, a shift of the solid-state 31P NMR resonances of the two phosphate close to Ca(5), namely P(2) and P(3), and a general disorder of β-TCP structure as shown by the broadening of the ATR-FTIR bands. In contrast, the relatively small Ca(5) site is not appreciated by strontium, which does not occupy it even at the highest concentrations. The clear preference of strontium for the Ca(4) site is further confirmed by the significant shift of the infrared symmetric stretching band due to P(1), that is the phosphate more involved into Ca(4) coordination. The preference is also maintained for a strontium content of about 80 at%, even if the high amount of strontium provokes a slight modification the β-TCP structure into the more symmetric β'-TCP [Boanini, 2019].

2. Functionalization of gelatin films.

Gelatin, and in particular gelatin films, finds a number of application in several fields. The kinds of functionalization carried out in this work are aimed to enrich the films with the peculiar properties of biologically active molecules and, at the same time, to modulate the mechanical and swelling properties of the films.

2.1 Gelatin – quercetin films.

Quercetin (3,3',4',5,7–pentahydroxy-flavone) is one of the most abundant flavonoids and displays remarkable anti-oxidant, anti-inflammatory, anti-bacterial and anti-cancer effects. In particular, it has been shown to inhibit the proliferation of different types of cancer cells [Wang, 2016]. On the other hand, its low water solubility and poor oral bioavailability limits its efficacy in dietary and pharmaceutical applications. These drawbacks have stimulated the research of possible systems for local delivery of the flavonoid [Forte, 2016; Forte, 2017; Patel, 2012].

In this work, gelatin films have been added with increasing amounts of quercetin, with the aim to modulate the properties of functionalized gelatin. Since quercetin is moderately soluble in ethanol and highly soluble in dimethyl sulfoxide (DMSO), the films were prepared following different routes, which imply the use of water, water/ethanol or DMSO, as solvents (Chapter 2 - Experimental Section – Preparation of Materials – par. 5 and 5.1).

Figure 4.55 - Photograph of films containing quercetin and obtained through different experimental procedures. EtOH and DMSO films appear transparent, whereas W films are opaque because of precipitation of quercetin particles.

The use of DMSO as solvent allowed to dissolve gelatin and quercetin in the same solution and to obtain films at different content of the flavonoid (DMSO films). At variance, the films prepared in water/ethanol (W films) were opaque and not homogeneous due to the precipitation of quercetin, so this procedure was abandoned (Figure 4.55).

Therefore, an alternative pathway has been adopted, where air-dried films prepared from gelatin aqueous solution were maintained in contact with quercetin dissolved in water/ethanol for 24 h (EtOH films).

The results of fluorescence analysis show that quercetin is homogeneously distributed in DMSO film, whereas its distribution in ETOH films seems not completely uniform (Figure 4.56): although the comparison of the image of EtOH 1 with that of EtOH 0 shows that the flavonoid is distributed all through the film, there are regions where it is more densely packed.

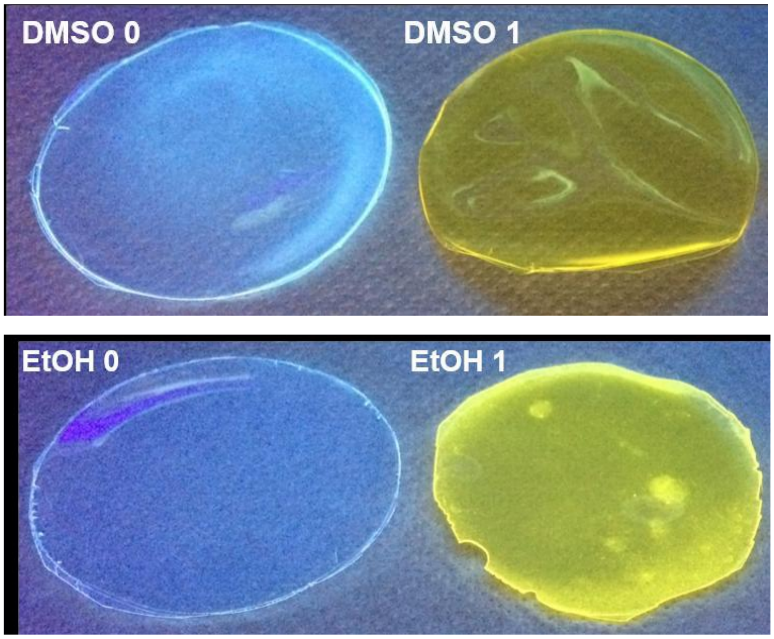

Figure 4.56 - Comparison between DMSO 0 and EtOH 0 films with DMSO 1 and EtOH 1 films observed under a 366 UV lamp *[reproduced from Rubini, 2020]*

Fluorescence microscope images confirm the particular distribution of quercetin in the films (Figure 4.57) which involves the formation of quercetin fluorescent aggregated structures of various sizes (from 20-30 μm to 80–90 μm).

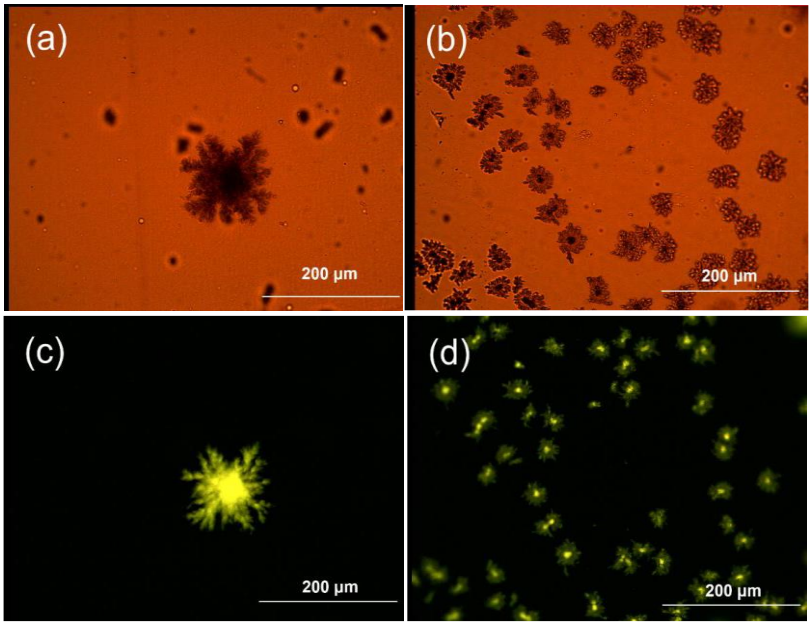

Figure 4.57 - Optical (a and b) and fluorescence (c and d) microscope images of EtOH 1 film. The images clearly show the presence of aggregated quercetin in dendrimer-like structures of different sizes *[reproduced from Rubini, 2020]*.

The results of the evaluation of absorption spectra of films dissolved in a water/ethanol mixture (Figure 4.58) show that the two film preparation methods lead to different amounts of quercetin loading (Table 4.16). DMSO films contain a quercetin amount corresponding to that present in the preparation solution, as expected, whereas EtOH samples, where quercetin was adsorbed from solution after preparation of the gelatin films, display a lower flavonoid content.

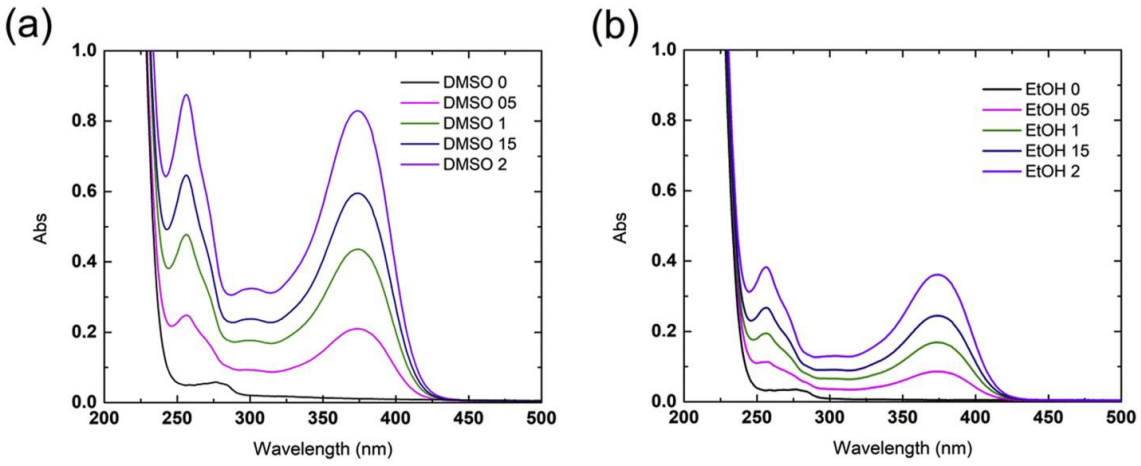

Figure 4.58 - Absorption spectra of DMSO (a) and EtOH (b) gelatin-quercetin film solutions *[reproduced from Rubini, 2020]*

Table 4.16 - Quercetin content of the functionalized films as a function of its theoretical content. Theoretical (T) and Experimental (E) quercetin content.

Sample	T (wt%)	E (wt%)	Sample	T (wt%)	E (wt%)
DMSO 05	1.0	1.0	EtOH 05	1.0	0.4
DMSO 1	2.0	2.0	EtOH 1	2.0	0.8
DMSO 15	2.9	2.9	EtOH 15	2.9	1.2
DMSO 2	3.8	3.8	EtOH 2	3.8	1.8

The results of thermogravimetric analysis confirm the greater quercetin content of DMSO than EtOH films. The TG plots of all the samples are characterized by three weight losses: the first (between about 30 and 250 °C) corresponds to water loss; the second (between about 250 and 500 °C) is due to gelatin decomposition; the third one (centered around 600–700 °C) is due to combustion of the residual components [Bigi, 2004]. Quercetin decomposition occurs around 350 °C [Borghetti, 2012], that is in the same region of gelatin decomposition. Fig. 4.59 reports the TG plots of the EtOH 2 and DMSO 2 samples compared with those of the relative controls. The comparison of the different weight losses in the range of temperature 250–500 °C indicates that quercetin content in EtOH 2 and DMSO 2 films is about 1±1 and 3±1 wt% respectively (Table 4.17), in good agreement with absorbance results.

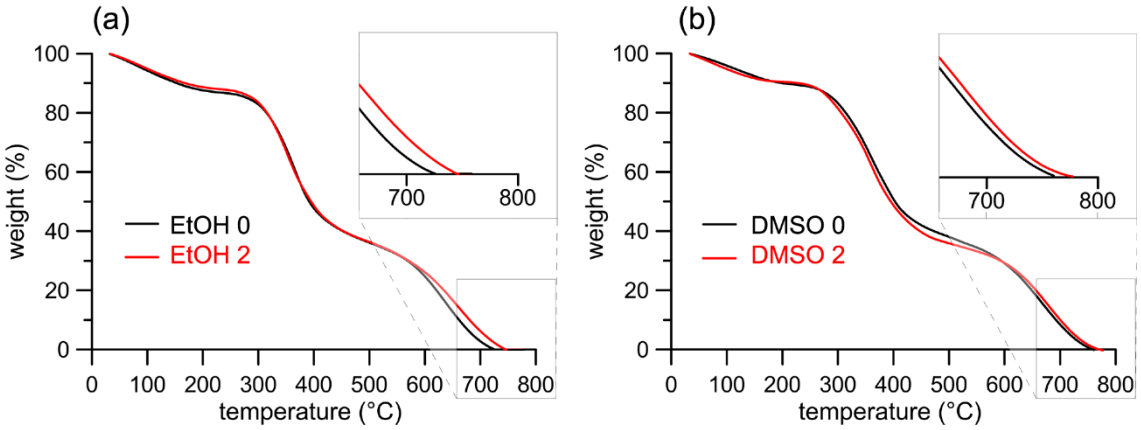

Figure 4.59 - TGA plots of (a) EtOH films and (b) DMSO films. The insets show an enlargement of the final parts of the plots *[reproduced from Rubini, 2020]*.

Table 4.17 – TGA weight loss of films during the different temperature ranges

SAMPLE	1st loss		2nd loss		3rd loss	
	wt %	T range (°C)	wt %	T range (°C)	wt %	T range (°C)
EtOH 0	13 ± 1	38-237	51 ± 1	237-501	37 ± 1	501-726
EtOH 2	12 ± 1	38-230	52 ± 1	230-497	37 ± 1	497-745
DMSO 0	10 ± 1	38-222	53 ± 1	222-515	37 ± 1	515-758
DMSO 2	9 ± 1	38-201	56 ± 1	201-518	35 ± 1	518-770

Moreover, the results of thermogravimetric analysis demonstrate that the films do not contain any residual solvent. In particular, the absence of DMSO is supported also by the results of FTIR-ATR analysis: the spectrum of DMSO is characterized by a strong band at 102 cm $^{-1}$, which is not present in the spectra of DMSO films (Figure 4.60). It is also worth noticing that the temperature corresponding to complete combustion is higher for the samples containing quercetin (745 and 726 °C respectively for EtOH 2 and EtOH 0; 770 and 758 °C for DMSO 2 and DMSO 0), suggesting a stabilizing effect of the flavonoid.

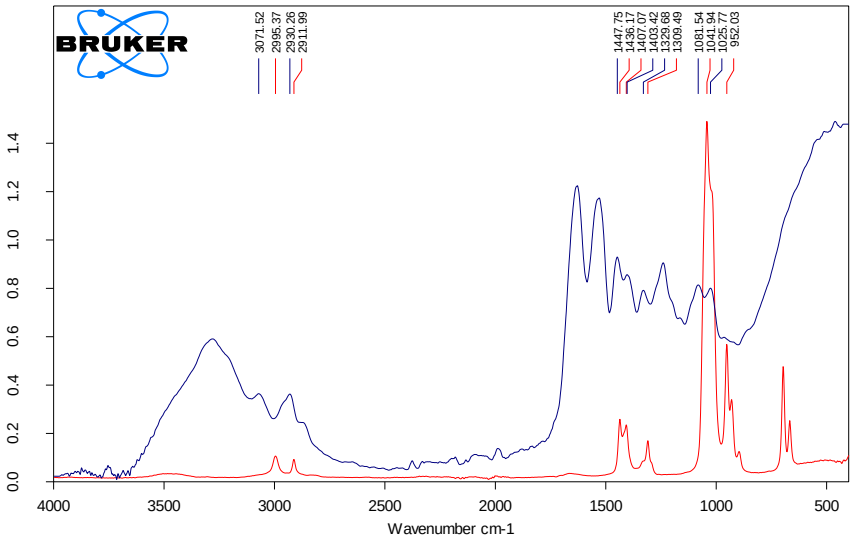

Figure 4.60 - ATR-FTIR spectra of pure DMSO solvent (red line) and DMSO 0 film (blue line).

DSC analysis provides information on the thermal stability of gelatin and on its content of triple helical structure. In fact, cooling of gelatin aqueous solutions results in a partial renaturation of collagen structure which implies a partial recovery of the triple helix

structure [Gomez-Guillen, 2011]. The DSC plot of gelatin exhibits an endothermic peak due to the transition of the recovered portions of triple helix to random coils (denaturation), with an associated denaturation enthalpy which depends on the extent of triple helix structure [Bigi, 2004].

The DSC plot of EtOH 0 shows indeed the presence of an endothermic peak centered at about 100 °C (denaturation temperature, Td) with an associated denaturation enthalpy (ΔHd) of about 28 J/g (Table 5.18). Loading of quercetin in the EtOH films does not significantly affect their thermal stability, in agreement with the values of the denaturation temperature that do not vary significantly with composition. At variance, the values of denaturation enthalpy of EtOH films containing quercetin are drastically reduced when compared with that of the unloaded sample, although it is not possible to appreciate variations as a function of quercetin content due to the broadening of the peaks (Figure 4.61, Table 4.18).

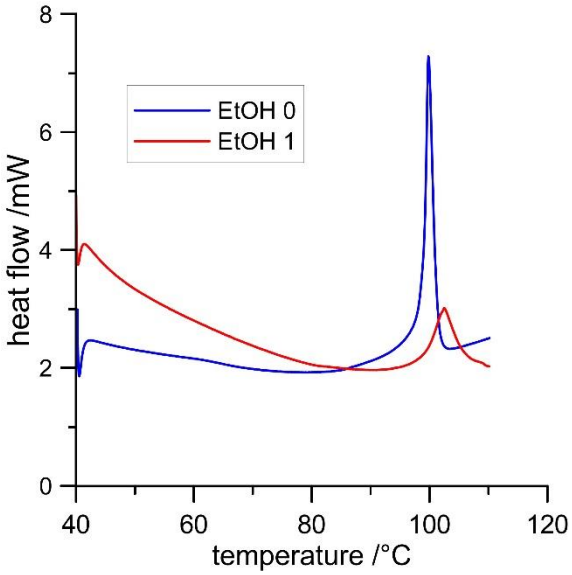

Figure 4.61 - DSC plots of EtOH 0 and EtOH 1 films

Table 4.18 - Denaturation temperatures (T_D) and enthalpies (ΔH_D) of EtOH films recorded through DSC measurements.

Sample	*T_D (°C)*	*ΔH_D (J/g)*
EtOH 0	100±1	28±1
EtOH 1	102±1	14±1
EtOH 15	98±1	18±1
EtOH 2	99±1	14±1

Reduction of the value of gelatin denaturation enthalpy is usually observed on samples treated with crosslinking chemical agents and can be ascribed to a reduction of hydrogen bonds (which break endothermically) and/or to an increase of covalent crosslinks (which break exothermically) [Bigi, 2004; Finch, 1972]. On this basis, the observed decrease of denaturation enthalpy suggests possible chemical interactions between gelatin and quercetin molecules which stabilize the films, in agreement with the observed reduction of the degree of swelling. The DSC plot of quercetin films prepared from DMSO solution did not show any endothermic peak indicating absence of triple helix structure and suggesting that gelatin does not gelify in DMSO [Kozlov, 1983].

In agreement with DSC results, the X-ray diffraction patterns of DMSO films show only a broad peak centered at about 20° of 2θ, corresponding to a periodicity of about 0.45 nm, which has been ascribed to the distance between adjacent polypeptide strands of gelatin [Okuyama, 2008]. The absence of the characteristic XRD reflections due to helical structure confirms that DMSO prevents the partial renaturation of the protein (Figure 4.62). At variance, the XRD patterns of EtOH films exhibit also a sharp peak at about 7° of 2θ corresponding to a periodicity of about 1.1 nm and related to the diameter of the triple helix [Okuyama, 2008].

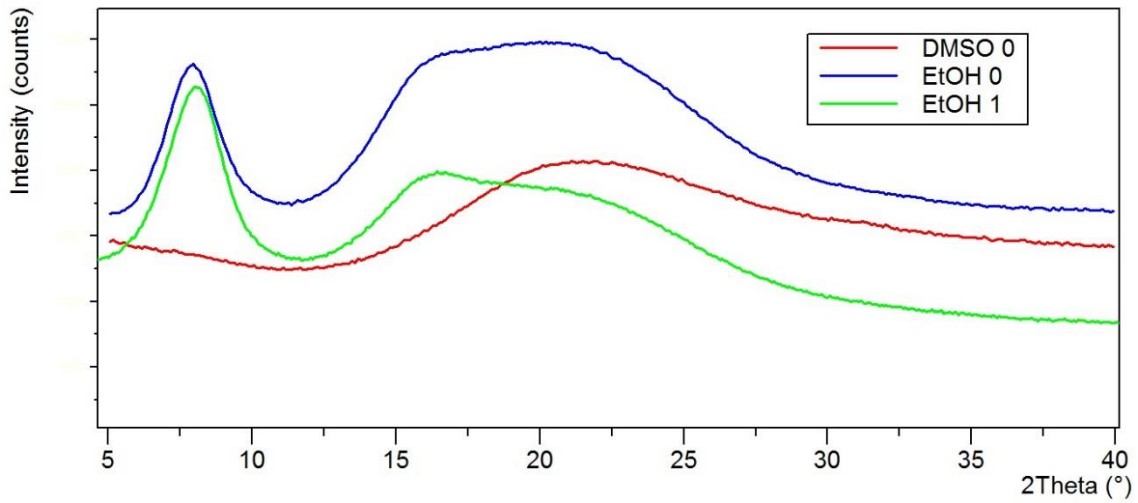

Figure 4.62 – XRD patterns of EtOH films showing the presence of the 1.1 nm reflection, which is absent in DMSO films.

The incorporation of quercetin in EtOH films resulted in reduced values of swelling in phosphate buffer (Figure 4.63): swelling of pure gelatin films is about 1700% after 48 h

immersion in PBS and decreases as a function of quercetin content down to 1000% for EtOH films at the maximum quercetin content. The degree of swelling of gelatin films prepared in DMSO is significantly lower: the maximum values reached by DMSO 0 and DMSO 2 films are about 700% and 600% respectively. However, the stability of the DMSO films in PBS is significantly reduced in comparison to that of EtOH films, so that after 48 h they are completely dissolved. Although also this series of films display a clear contribution of quercetin, the noticeable reduction of swelling induced by DMSO does not allow to appreciate a clear trend as a function of the content of the flavonoid.

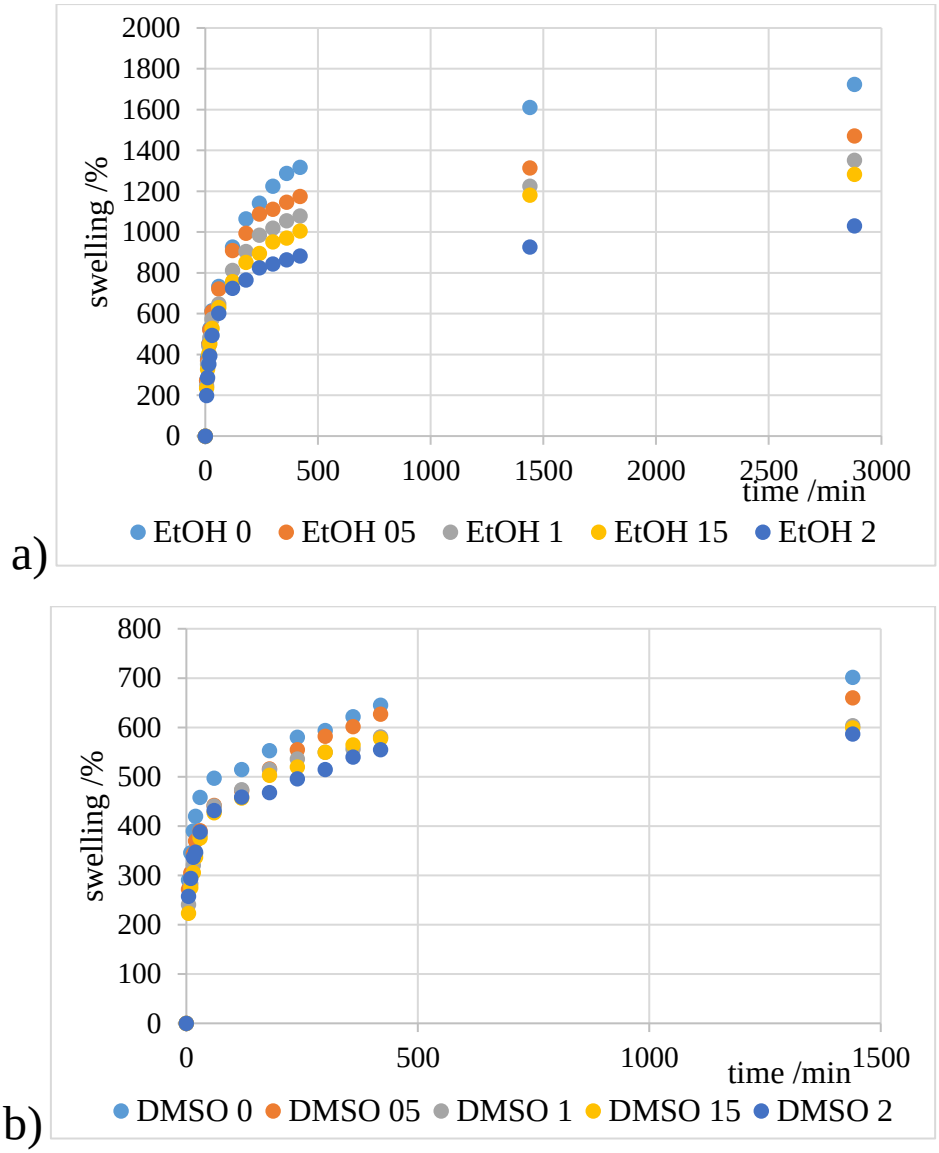

Figure 4.63 - Swelling curves of (a) EtOH films and (b) DMSO films. Standard deviations are into the size of the symbols.

At variance with swelling results, the values of contact angle and of water solubility of the different samples do not exhibit significant differences. In particular, contact angle displays mean values in the range 72°–77°, showing that all prepared films have a hydrophilic behavior and a good wettability (Table 4.19). Although DMSO films are less stable than EtOH films in PBS, they show similar water solubility, indeed FS (%) values do not vary as a function of quercetin content, as reported in Table 4.20.

Table 4.19 - Values of water contact angle (in degrees) measured on EtOH and on DMSO films. The different amounts of quercetin are indicated horizontally for allowing direct comparison.

	0	05	1	15	2
EtOH	72 ± 4	76 ± 2	73 ± 6	74 ± 3	72 ± 1
DMSO	77 ± 5	77 ± 2	72 ± 2	76 ± 3	73 ± 5

Table 4.20- Values of water solubility FS(%) measured on EtOH and on DMSO films. The different amounts of quercetin are indicated horizontally for allowing direct comparison.

	0	05	1	15	2
EtOH	59 ± 4	63 ± 10	52 ± 8	64 ± 7	59 ± 6
DMSO	59 ± 10	61 ± 8	60 ± 9	58 ± 9	53 ± 8

The absence of triple helix structure in the DMSO films can be considered responsible of their mechanical behavior, which is quite different from that of EtOH films. At variance with EtOH films, DMSO films cannot be maintained in the mixture water/ethanol for the period of time (72 h) usually utilized to reach a constant relative humidity of 75% [Boanini, 2010], and must be removed from the mixture just after 1 min because they become sticky. Moreover, under tensile stress, they undergo a remarkable elongation, and exhibit jagged stress-strain curves (Figure 4.64), which prevent a proper evaluation of their mechanical parameters.

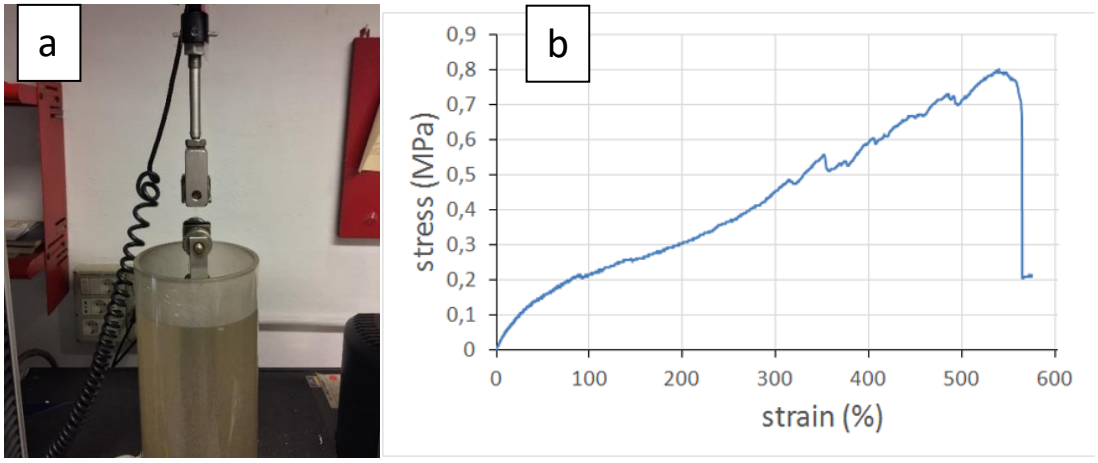

Figure 4.64- (a) The machine used for mechanical tests equipped with water/ EtOH bath and (b) Typical stress-strain curve of a DMSO film.

On the contrary, the stress strain curves of the samples of the EtOH series are similar to those characteristic of gelatin films, although characterized by different values of the mechanical parameters (Figure 4.65).

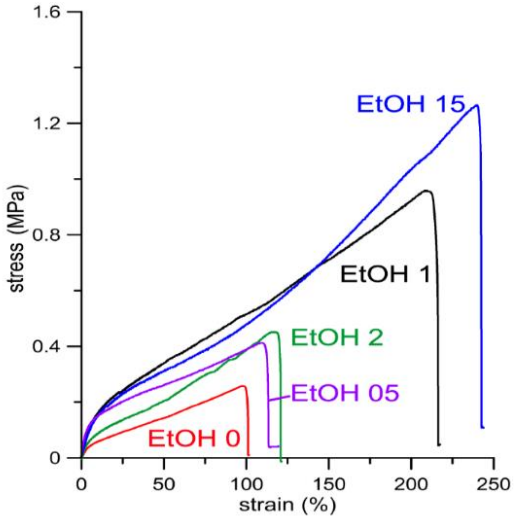

Figure 4.65 - Typical stress-strain curves of EtOH gelatin films at different quercetin content *[reproduced from Rubini, 2020]*.

Both the values of stress at break and deformation increase significantly on increasing quercetin concentration up to 1.5 g/L, whereas the value of Young's modulus does not show any significant variation (Table 4.21). On the other hand, quercetin concentration of 2 g/L, which means a flavonoid content of 1.8 wt% (Table 4.16), provokes a significant worsening of the mechanical parameters of the films, as shown in Table 5.21, most likely also due to the non homogeneous distribution of the flavonoid inside the films [Rubini, 2020].

Table 4.21 – Strain at Break, σ_b, Stress at Break, ε_b, and Young's Modulus, E, of EtOH films.

sample	E (MPa)	σ_b (MPa)	ε_b (%)
EtOH 0	1.5 ± 0.2	0.28 ± 0.05[a]	100 ± 20[a]
EtOH 05	1.3 ± 04	0.54 ± 0.08	135 ± 20[b]
EtOH 1	1.8 ± 0.6	1.1 ± 0.2[a]	202 ± 29[a]
EtOH 15	1.9 ± 0.6	1.4 ± 0.1[a]	238 ± 10[a,b]
EtOH 2	1.4 ± 0.8	0.4 ± 0.2[a]	109 ± 30[a]

σ_b : [a] EtOH 0 vs EtOH 05, EtOH 1, EtOH 15; EtOH 1 vs EtOH 05; EtOH 15 vs EtOH 05; EtOH 2 vs EtOH 1, EtOH 15 ($p<0.001$). b EtOH 15 vs EtOH 1 ($p<0.05$)
ε_b : : [a] EtOH 0 vs EtOH 1, EtOH 15; EtOH 1 vs EtOH 05; EtOH 15 vs EtOH 05; EtOH 2 vs EtOH 1, EtOH 15 ($p<0.001$). [b] : EtOH 05 vs EtOH 0; EtOH 15 vs EtOH 1 ($p<0.05$)

Quercetin release in PBS from some selected functionalized films was determined from absorbance values at the quercetin maximum (375 nm) as a function of time. The release initially increases with time, but reaches a steady state in a few hours (Figure 4.66).

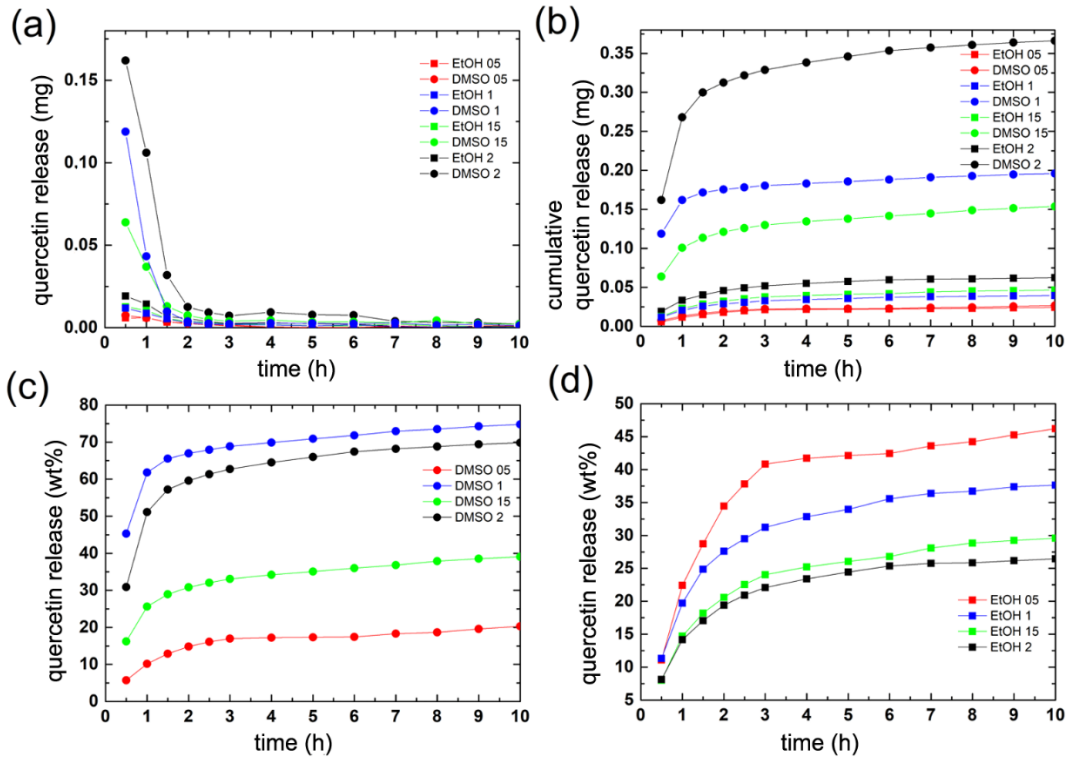

Figure 4.66 - Quercetin release for each refresh (a), and cumulative release (b) expressed in mg. (c, d) cumulative release expressed as % of the initial content from DMSO (c) and EtOH (d). *[reproduced from Rubini, 2020]*.

The amount of quercetin released by EtOH films is significantly lower than that liberated by DMSO films (maximum value of release: about 45 and 70% of the initial content from EtOH and DMSO samples, respectively). Moreover, the percentage of quercetin release from DMSO films generally increases with quercetin content (with the exception of DMSO 1 sample), whereas EtOH samples display an opposite trend. The decrease of quercetin release from EtOH films on increasing their pristine content is in agreement with their swelling behavior and confirms the stabilizing role of the flavonoid, as suggested by the results of denaturation enthalpy [Rubini, 2020].

Quercetin can quench reactive oxygen species (ROS) displaying antioxidant activity [Enoki, 2014]. In order to verify if quercetin if functionalized gelatin films display antioxidant properties we measured the radical scavenging activity (RSA) of the different samples by means of the 1,1-diphenyl-2-picryl-hydrazyl (DPPH·) assay (Chapter 2 - Experimental Section – Characterization of Materials– par. 14.1). DPPH· exhibits a characteristic absorption band at 515 nm. The intensity of this band can be reduced by the scavenging action of the antioxidant material, which donates hydrogen to DPPH· to form the corresponding hydrazine. The test was carried out on different amounts of samples in order to get different concentration of quercetin. The results show that RSA increases as a function of quercetin concentration. In particular, pure quercetin exhibits RSA values up to about 35% as its concentration increases up to 50 μM. All the examined samples display RSA values similar to those recorded for pure quercetin, indicating that the antioxidant properties is maintained in both series of functionalized films (Figure 4.67). No statistically significant differences were measured in RSA values comparing the pure quercetin, set as reference control, and the tested samples at the same quercetin content, irrespective of the solvent used for preparation.

The two different methods of preparation developed in this work provide functionalized films characterized by different properties. In particular, DMSO films are less stable in aqueous solution and display a very high extensibility, most likely because they lack triple helix structure. Differently, the increase of quercetin content in EtOH films provokes a variation of chemico-physical properties, in agreement with the presence of chemical interaction between gelatin and the flavonoid. Both quercetin containing DMSO and EtOH films show a sustained flavonoid release in PBS, as well as RSA

values indicative of remarkable anti-oxidant properties, suggesting possible applications as local delivery systems of the functionalizing agent [Rubini, 2020].

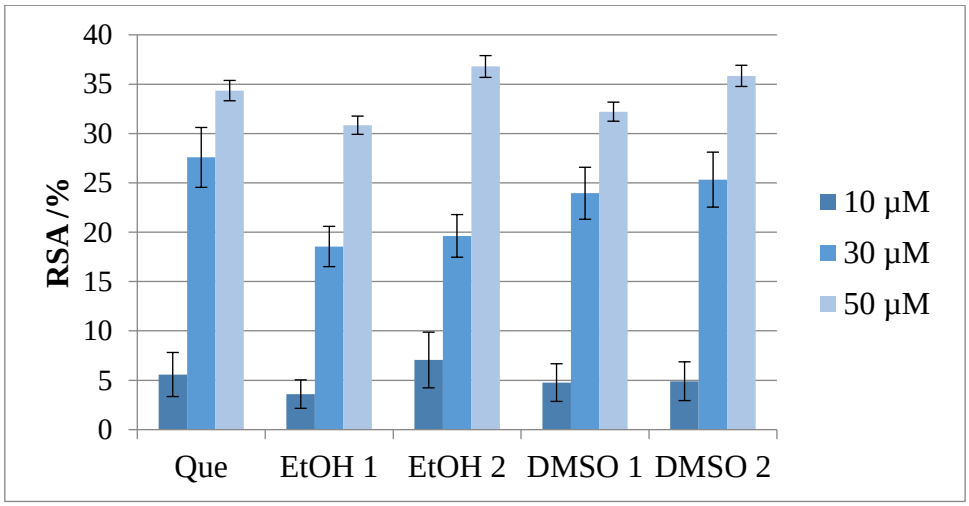

Figure 4.67 - Antiradical activity, expressed as % RSA, of the different samples and pure quercetin toward DPPH·. Bars represent the mean ± SD of two independent measurements.

2.2 Gelatin – curcumin films.

Curcumin—(1E,6E)-1,7-bis(4-hydroxy-3-methoxyphenyl)-1,6-heptadiene-3,5-dione—is a natural polyphenol extracted from the rhizomatous plant Curcuma Longa(Turmeric) of the Ginger family [Priyadarsini, 2014]. In solution it exhibits a keto-enol tautomerism and shows polymorphism in the solid state, where it exists just as the keto-enol tautomer [Dai, 2020]. Its numerous biological activities includes antioxidant, anticancer, anti-inflammatory and antimicrobial properties [Hewlings, 2017; Wanninger, 2015]. However due to its hydrophobicity, it displays a very poor solubility, which, together with rapid metabolism and systemic elimination, results in poor bioavailability in physiologic conditions [Hewlings, 2017].

In this Chapter 4 - par. 2.1, it was demonstrated that the use of DMSO as a solvent hinders the partial regain of the triple helix structure characteristic of collagen and prevents gelatin gelification, whereas water/ethanol as a solvent for gelatin yields opaque and non-homogeneous films [Rubini, 2020]. Therefore, in this work gelatin films were firstly prepared from an aqueous solution, then submitted to a second step of loading of curcumin from a water/ethanol solution. In order to improve the properties of the films, gelatin has also been submitted to a crosslinking process through the use of

glutaraldehyde as chemical crosslinking agent that was introduced as last step, after curcumin adsorption.

G-0 films are transparent and colorless, whereas crosslinking with GTA provokes the films to get slightly colored (Figure 4.68). Curcumin imbues a yellow color to the films, which becomes more intense when passing from G-02 to G-1. A further increase of the color intensity occurs after crosslinking with GTA (Figure 4.69).

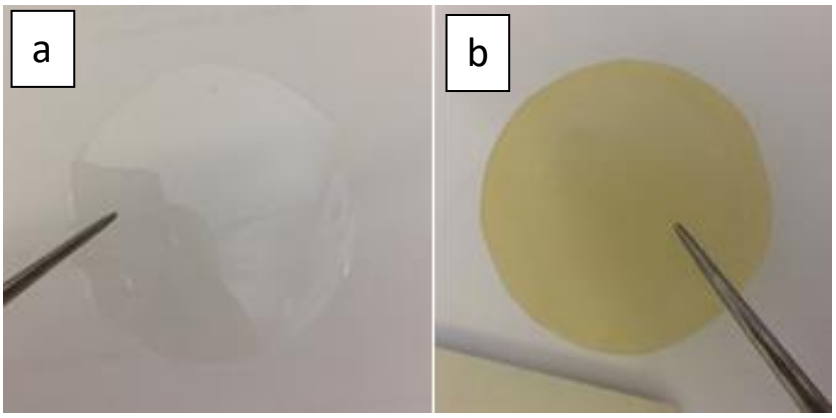

Figure 4.68 – Photographs of (a) G-0 and (b) GTA-0 films.

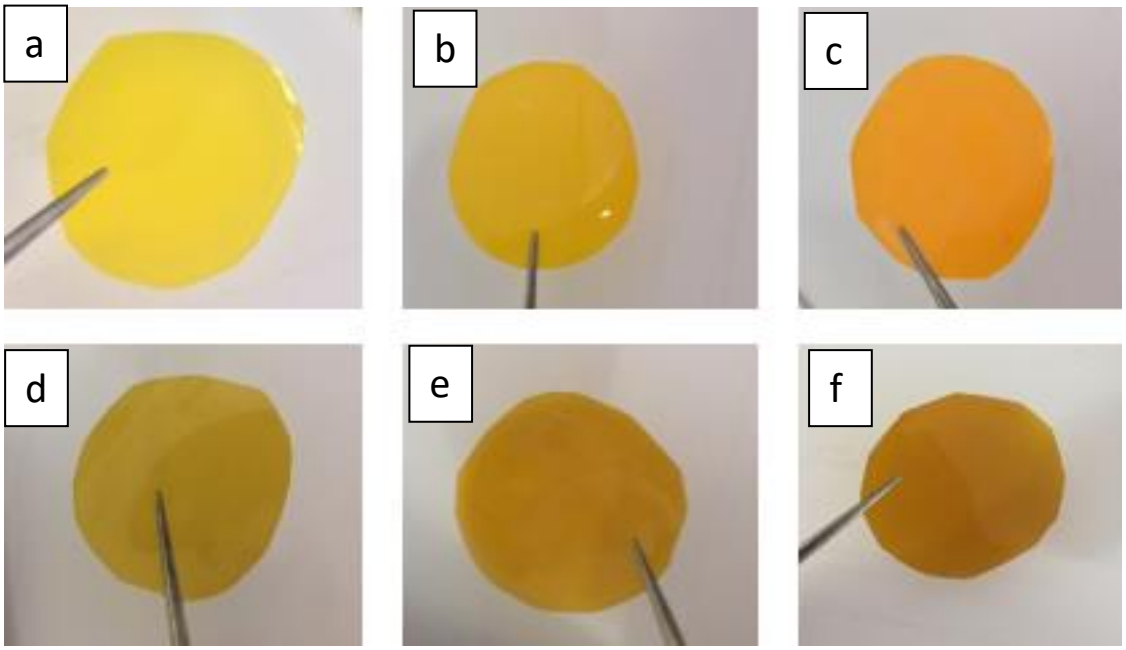

Figure 4.69 - Photographs of films at different curcumin content: (a) G-02; (b) G-05; (c) G-1; (d) GTA-02; (e) GTA-05; (f) GTA-1.

In spectrophotometric analysis curcumin exhibits a strong absorption band in the visible region, which in water/ethanol solutions falls around 430 nm [Mondal, 2016] and allows determination of curcumin quantitative content. In fact, the absorption spectra of films dissolved in a water/ethanol mixture clearly show the increase of the intensity of the absorption band in the visible region as a function of curcumin concentration (Figure 4.70). Curcumin content in GTA samples was not measured since the films are not soluble after crosslinking.

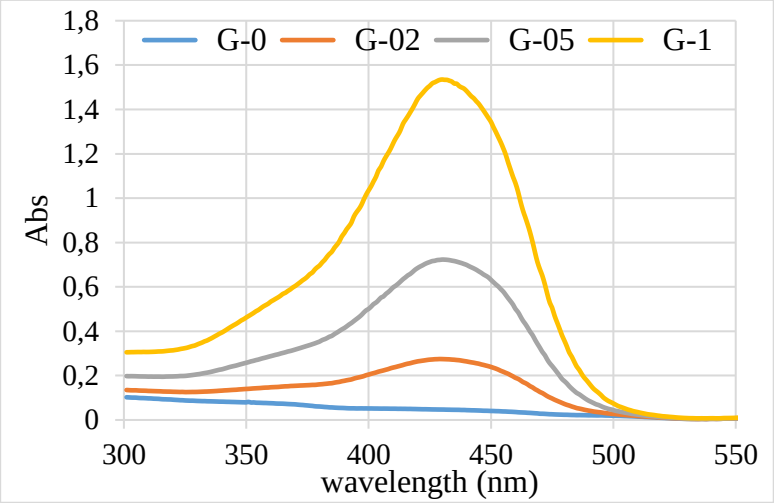

Figure 4.70 - Absorption spectra of gelatin-curcumin film solutions in water/ethanol.

Curcumin content determined from evaluation of the absorption spectra increases with its concentration in solution up to about 1.2 wt% (Table 4.22). Since GTA treatment was performed after curcumin adsorption, it is reasonable to assume that GTA samples contain the same amounts of curcumin as G samples.

Table 4.22 – Amount of curcumin content in functionalized films.

Sample	Curcumin content (wt %)
G-0	---
G-02	0.20 ± 0.02
G-05	0.55 ± 0.05
G-1	1.20 ± 0.10

The DSC plot of G-0 films exhibits an endothermic peak centered at 97 °C (denaturation temperature, T_d), with a denaturation enthalpy (ΔH_d) of 23 J/g. The

endothermic transition (denaturation) is due to disruption of the portions of triple helix to random coils. In particular, T_d and ΔH_d are associated with thermal stability and extent of the triple helix structure, respectively [Bigi, 2004]. The endothermic peak shows a modest, but appreciable, shift to higher temperatures in functionalized G films, in agreement with an increase of gelatin stability, which suggests possible chemical interactions between gelatin and curcumin (Figure 4.71, Table 4.23).

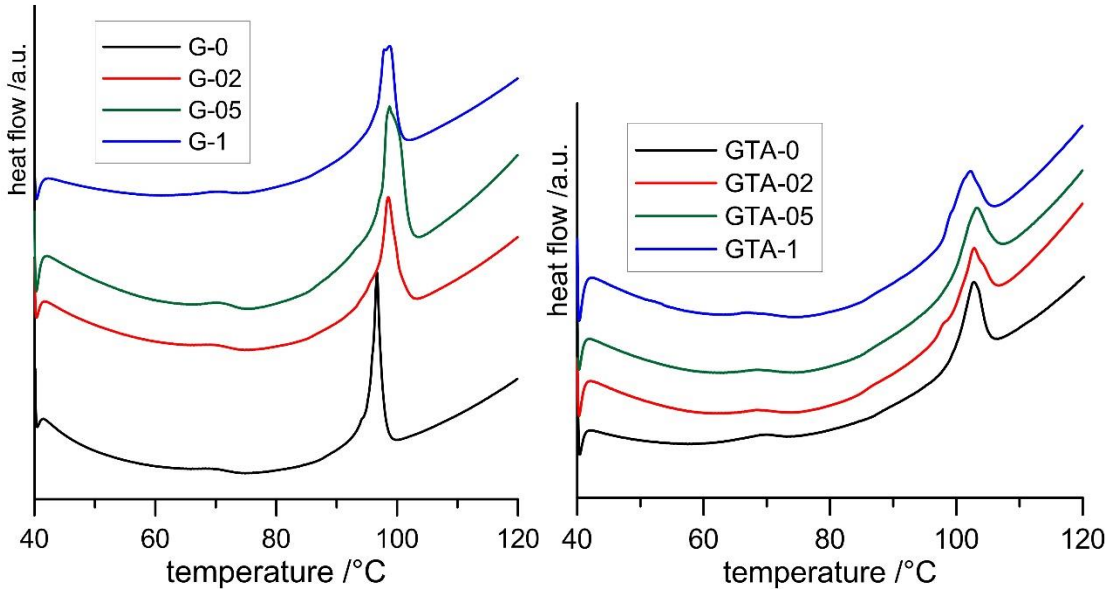

Figure 4.71 – DSC plots of gelatin films functionalized with curcumin.

Table 4.23 – DSC results for gelatin films functionalized with curcumin.

Sample	T_d (°C)	ΔH_d (J/g)	Sample	T_d (°C)	ΔH_d (J/g)
G-0	97	23	GTA-0	103	13
G-02	98	23	GTA-02	103	11
G-05	99	23	GTA-05	103	11
G-1	99	24	GTA-1	102	11

The X-ray diffraction patterns of un-crosslinked films do not show significant modifications as a function of curcumin content and always exhibit two peaks (Figure 4.72): a sharp one at about 7.5° and a broad one at about 20°, which are due to the characteristic structure of gelatin [Okuyama, 2008]. The low angle peak at about 7.5 °/2θ, which is related to the diameter of the triple helix portions of gelatin, is absent in the XRD pattern of GTA-0, suggesting that crosslinking with glutaraldehyde blocks the random coil conformation of gelatin and inhibits the partial regain of triple helix structure occurring during cooling (Figure 4.72). On the other hand, the relative

intensity of this peak increases from GTA-02 to GTA-1, indicating that curcumin counteracts the negative effect of GTA on the partial renaturation of the collagen structure, most likely by reducing the number of available sites for covalent interaction of gelatin with glutaraldehyde.

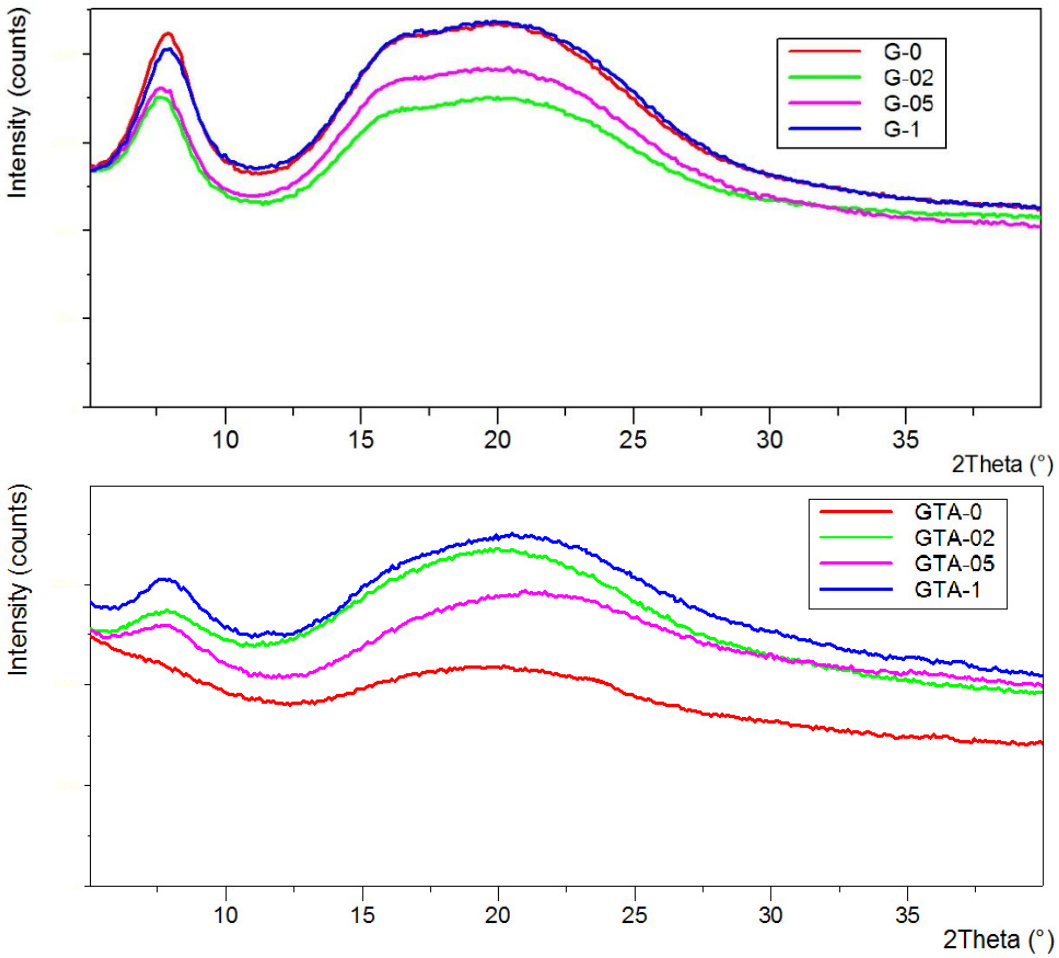

Figure 4.72 – XRD patterns of the films functionalized with curcumin.

Swelling behaviour of gelatin is modified by the presence of curcumin, In fact, swelling of pristine gelatin films, GEL-0, amounts to about 1700% after 48 h in PBS and further prolongation of immersion time results in complete dissolution of the films (Figure 4.73). The same trend is observed for G-02, although the presence of curcumin decreases the maximum value of swelling before dissolution down to around 1400%. A further increase of curcumin content not only provokes a further decrease of swelling degree (Figure 4.73) but stabilizes the films which maintain their compactness even after a week in PBS. The reduction of swelling in functionalized samples suggests the

occurrence of chemical interactions between the functional groups of curcumin and those of gelatin [Strauss, 2004].

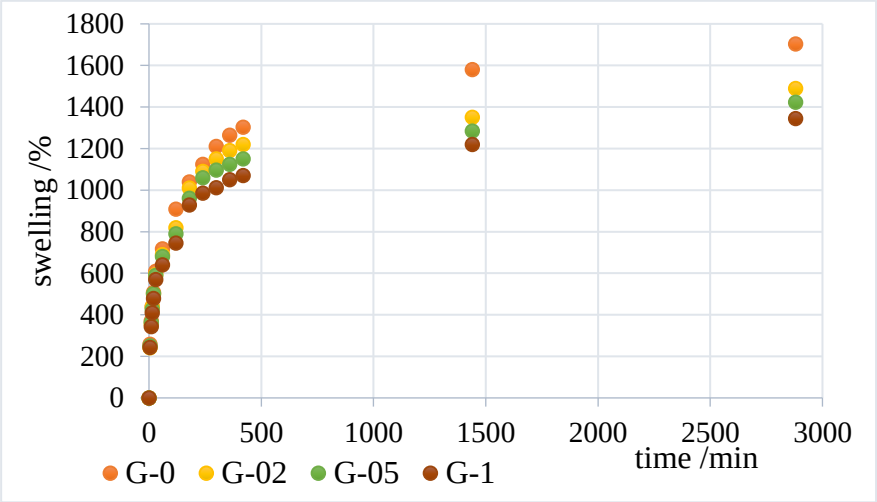

Figure 4.73 - Swelling curves of gelatin films functionalized with curcumin. Standard deviations are in the size of the symbols.

A much greater effect on swelling is observed after crosslinking with glutaraldehyde. In fact, swelling of films crosslinked with GTA reaches a plateau in 24 h, when it assumes remarkably reduced values in comparison with those observed before crosslinking (Figure 4.74). The influence of GTA far exceeds that of curcumin so that the values measured for samples at increasing polyphenol content tend to decrease, but are not significantly different.

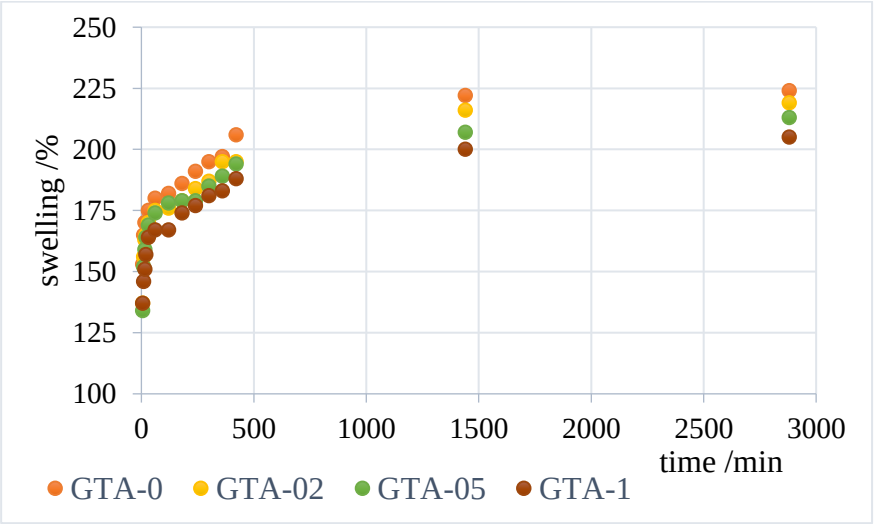

Figure 4.74 - Swelling curves of gelatin films functionalized with curcumin and crosslinked with GTA. Standard deviations are in the size of the symbols.

GTA exerts a great influence also on water solubility, which is evident just by having a look to the samples during the tests (Figure 4.75).

Figure 4.75 – Photographs of the samples after heat treatment.

The value of FS (%) of pristine gelatin films decreases down to about one-fifth after crosslinking (Table 4.24). Moreover, the values of water solubility of crosslinked functionalized samples do not show significant difference as a function of curcumin content, and just the value of GTA-1 is significantly different from that of GTA-0. On the contrary, the influence of the polyphenol is clearly appreciable in non-crosslinked films, which exhibit significantly decreasing FS values when passing from G-0 to G-1.

Table 4.24 – Water solubility results for curcumin-functionalized gelatin films.

Sample	FS (%)
G-0	94 ± 5
G-02	89 ± 4
G-05	86 ± 5
G-1	46 ± 3 [a]
GTA-0	22 ± 1
GTA-02	20.3 ± 0.4
GTA-05	21.3 ± 0.6
GTA-1	19 ± 1 [a]

[a] G-1 vs G-0, G-02, G-05 ($p < 0.05$); GTA-1 vs GTA-0 ($p < 0.05$)

Functionalization with curcumin influences also the mechanical properties of gelatin films, as shown by the stress-strain curves of gelatin films at increasing polyphenol content (Figure 4.76) and by the relative main mechanical parameters reported in Table 4.25. In particular, the deformation at break, ε_b, decreases, whereas the values of Young's modulus, E, increase on increasing curcumin content, suggesting that curcumin interactions with gelatin provokes a stiffening of the films.

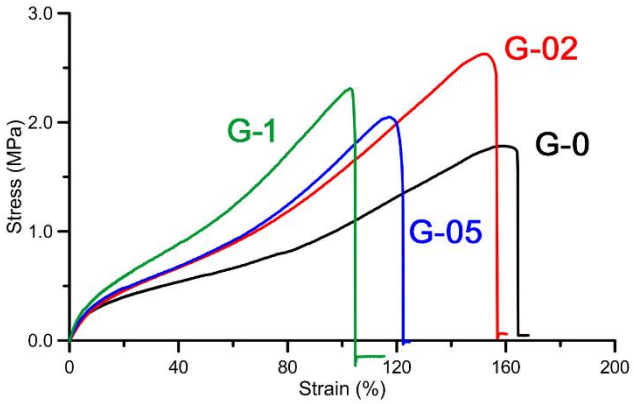

Figure 4.76 – Stress–strain curves of gelatin films at different curcumin content *[reproduced from Rubini, 2021]*.

Table 4.25 – Strain at Break, σ_b, Stress at Break, ε_b, and Young's Modulus, E, of G films.

Sample	σ_b (MPa)	ε_b (%)	E (MPa)
G-0	1.9 ± 0.9	165 ± 35	6.2 ± 0.9
G-02	2.6 ± 0.9	155 ± 10	7.0 ± 1.9
G-05	2.2 ± 1.2	125 ± 9 [a,b]	7.6 ± 1.1
G-1	2.3 ± 0.5	105 ± 8 [a]	8.9 ± 0.8 [a]

ε_b: [a] G-1 vs G-0, G-02, G-05; G-05 vs G-02 ($p<0.001$). [b] G-05 vs G-0 ($p<0.05$)
E: [a] G-1 vs G-0 ($p<0.001$)

The main effect of GTA crosslinking on un-functionalized films is a significant modification of the stress–strain curve (Figure 4.77), which involves a dramatic reduction of the value of deformation at break (Table 4.26). The presence of curcumin in GTA samples interferes with the action of the crosslinking agent in agreement with XRD data, so that the values of ε_b show a modest, but significant, increase on increasing polyphenol content, while the values of E decrease [Rubini, 2021].

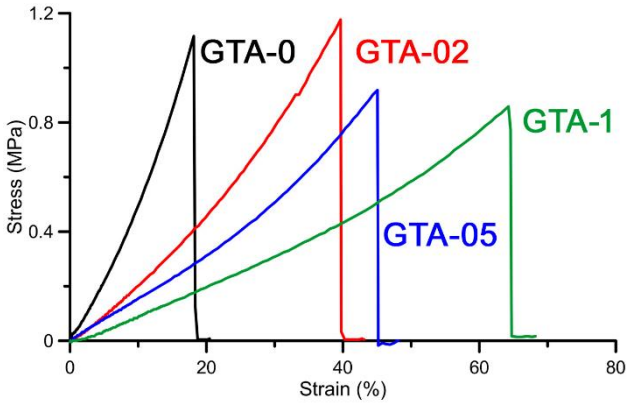

Figure 4.77 – Stress–strain curves of gelatin films at different curcumin content and crosslinked with GTA *[reproduced from Rubini, 2021]*.

Table 4.26 – Strain at Break, σ_b, Stress at Break, ε_b, and Young's Modulus, E, of GTA films.

Sample	σ_b (MPa)	ε_b (%)	E (MPa)
GTA-0	1.1 ± 0.5	18 ± 5	6.5 ± 0.9
GTA-02	1.2 ± 0.5	40 ± 10 [a]	2.1 ± 0.8 [a]
GTA-05	0.9 ± 0.6	45 ± 12 [a]	1.7 ± 0.3 [a]
GTA-1	0.9 ± 0.5	64 ± 18 [a,b]	1.1 ± 0.8 [a]

ε_b: [a] GTA-1, GTA-05, GTA-02 vs GTA-0 ($p<0.001$); [b] GTA-1 vs GTA-02 ($p<0.05$)
E: [a] GTA-1, GTA-05, GTA-02 vs GTA-0 ($p<0.001$)

Curcumin release from the different samples was determined from analysis of the UV-vis absorption spectra. In particular, release was measured in different solvents: water/ethanol, physiological solution and PBS solution.

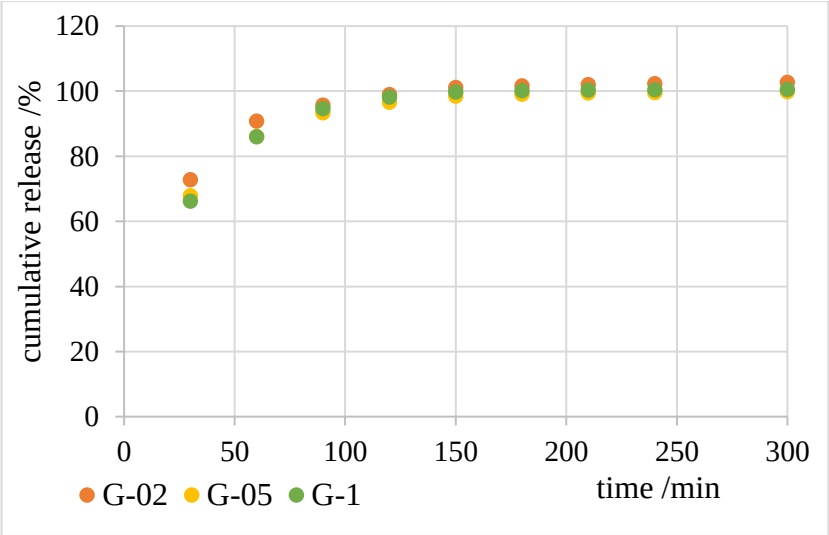

Figure 4.78 - Curcumin release, expressed as a percentage of the initial content, from G films incubated in water/ethanol solution. Standard deviations are in the size of the symbols.

Due to the relatively high solubility of curcumin in water/ethanol, its release in this solution is fast and almost quantitative: it reaches a plateau in just a couple of hours. The release increases as curcumin initial content increases, and corresponds to complete removal of the polyphenol from the different samples (Figure 4.78).

At variance, release in physiological solution increases with time up to 0.08 g/g% during the first hours, and reaches values of about 0.10 g/g% in 24 h. In this case, the released amount of curcumin from the different samples does not vary significantly, but it corresponds to different percentages of the polyphenol initial content: up to about 52%, 22% and 12% for G-02, G-05 and G-1 respectively (Figure 4.79).

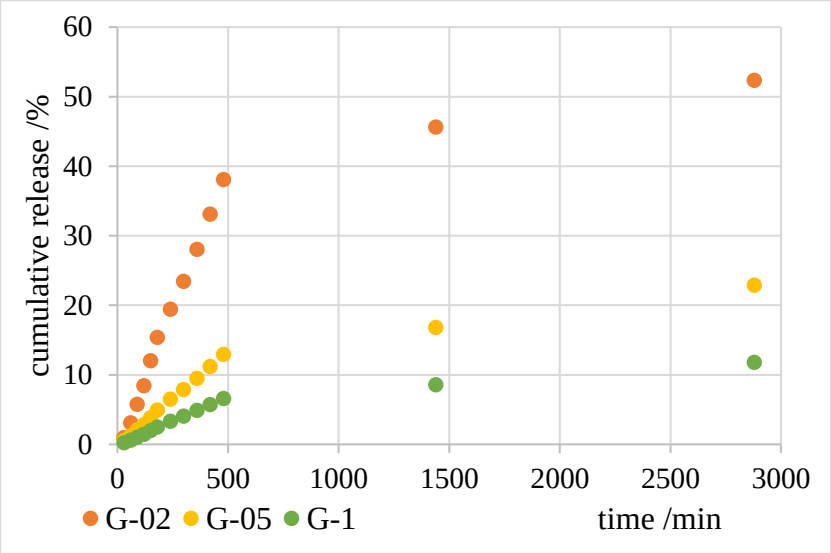

Figure 4.79 - Curcumin release, expressed as a percentage of the initial content, from G films incubated in physiological solution. Standard deviations are in the size of the symbols.

Much smaller values of curcumin release were measured in PBS solution, most likely because the ionic strength of PBS reduces gelatin swelling in comparison to physiological solution. Cumulative release increases with time to reach a steady state in 15–24 h, and indeed it corresponds to small percentages of the initial content of curcumin: about 5.5%,3.4% and 2.6% for G-02, G-05 and G-1 respectively (Figure 4.80).

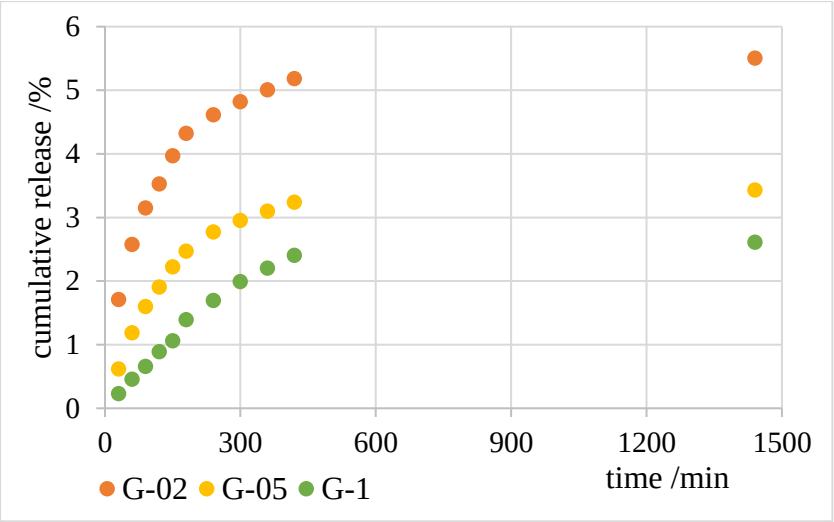

Figure 4.80 - Curcumin cumulative release, expressed as a percentage of the initial content, from G films incubated in PBS solution. Standard deviations are in the size of the symbols.

As expected, GTA crosslinking dramatically reduces curcumin release. The amount of polyphenol released after 24 h in H2O/EtOH is less than 7 wt%, while in physiological solution, as well as in PBS, it reaches about 3 wt% (Figure 4.81).

a)

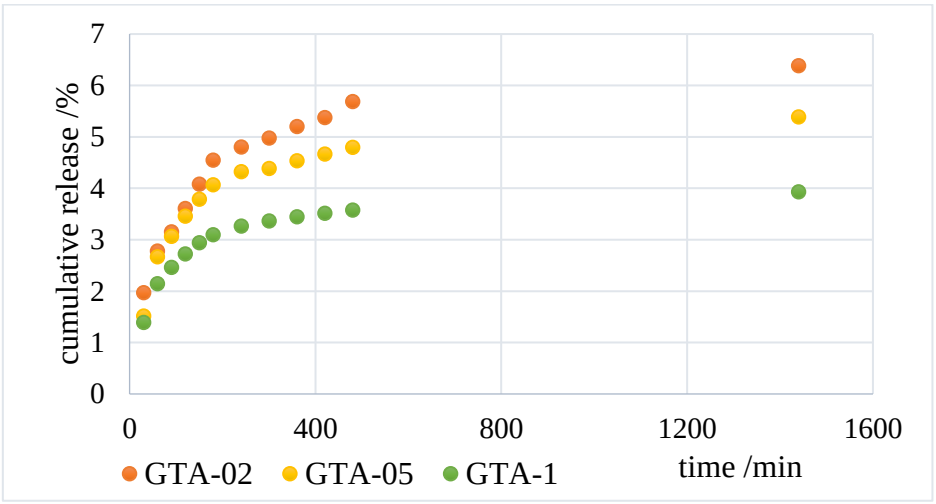

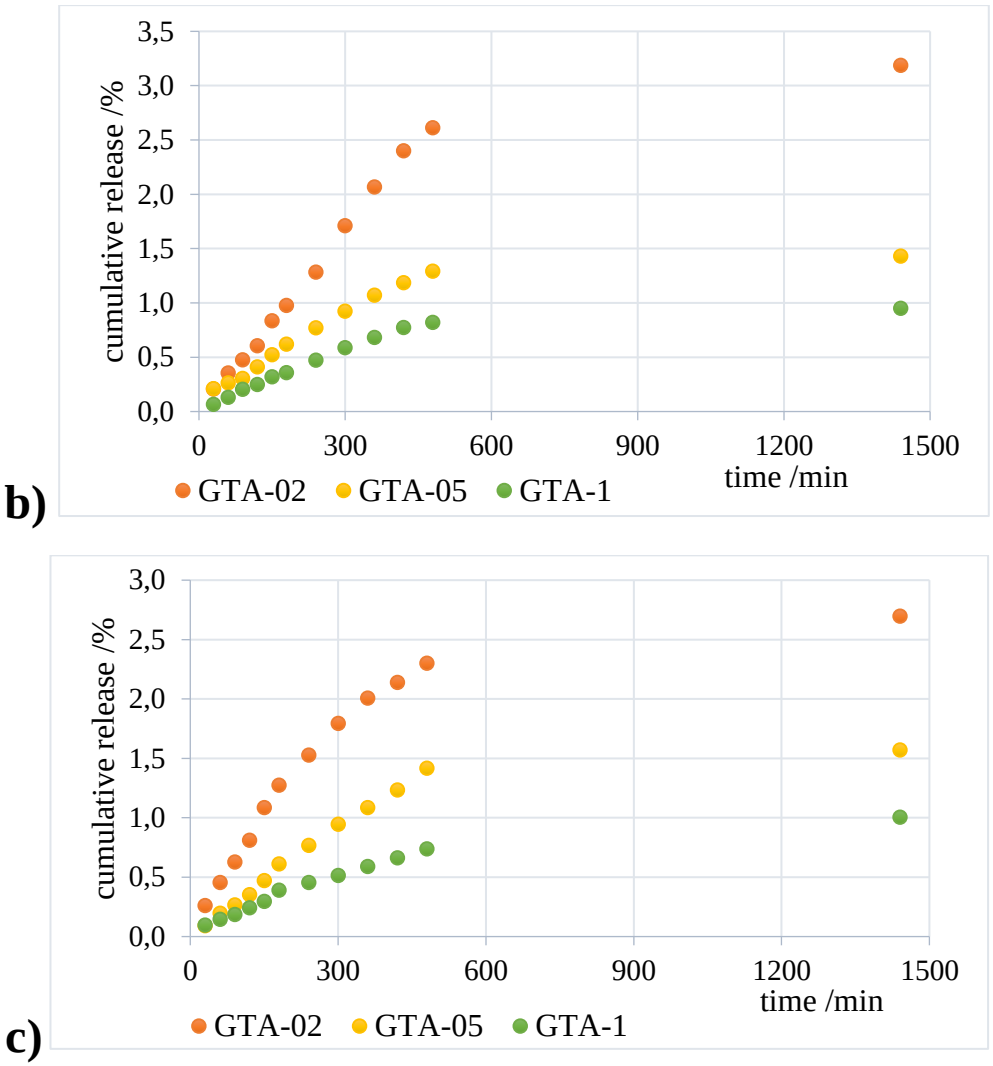

Figure 4.81 - Curcumin cumulative release, expressed as a percentage of the initial content, from GTA films incubated in (a) water/ethanol; (b) physiological solution; (c) PBS. Standard deviations are in the size of the symbols.

The ability of curcumin to quench reactive oxygen species is the reason for its antioxidant and anti-inflammatory properties. The test based on 1,1-diphenyl-2-picryl-hydrazyl (DPPH·) assay [Ak, 2008] was carried out on different amounts of specimens so as to get different curcumin contents. The values of radical scavenging activity (RSA) are compared with those obtained for pure curcumin (Figure 4.82). Pure curcumin exhibits RSA values increasing from about 25% to about 78% as its concentration increases from 10 to 50 mM. All the examined samples display RSA values not significantly different from those recorded for pure curcumin, indicating that the antioxidant properties are maintained in functionalized films.

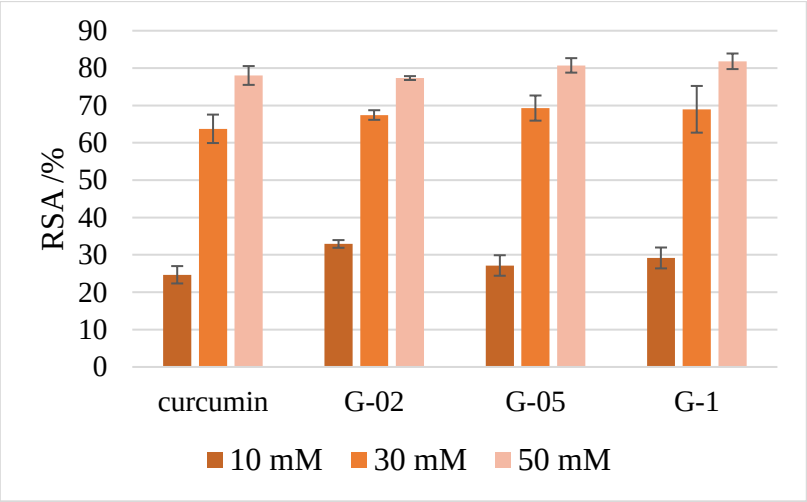

Figure 4.82 - Antiradical activity, expressed as % RSA, of the different samples and pure curcumin toward DPPH·. Bars represent the mean ± SD of two independent measurements.

In conclusion, the amounts of curcumin loaded on gelatin films in this work provide the films with modulated properties (swelling, water solubility, denaturation enthalpy, mechanical properties). Moreover, the films show remarkable antioxidant properties and exhibit sustained polyphenol release. Crosslinking with glutaraldehyde causes further modulations of the main properties of the films. Overall, the results indicate that gelatin films can be considered good candidates as delivery systems for curcumin [Rubini, 2021].

RESULTS AND DISCUSSION – References

- Ak T, Gulcin I. Antioxidant and radical scavenging properties of curcumin. Chem. Biol. Interact. 2008;174:27–37
- Belik AA, Izumi F, Stefanovich SY, Malakho AP, Lazoryak BI, Leonidov IA, Leonidova, ON, Davydov SA. Polar and centrosymmetric phases in solid solutions $Ca_{3-x}Sr_x(PO_4)_2$ ($0 \leq x \leq 16/7$). Chem. Mater. 2002;14:3197–3205
- Bigi A, Boanini E. Functionalized biomimetic calcium phosphates for bone tissue repair. J. Appl. Biomater. Funct. Mater. 2017;15:e313–e325
- Bigi A, Boanini E, Bracci B, Falini G, Rubini K. Interaction of acidic poly-amino acids with octacalcium phosphate. J. Inorg. Biochem. 2003;95:291–296
- Bigi A, Foresti E, Gandolfi M, Gazzano M, Roveri N. Isomorphous substitutions in β-tricalcium phosphate: The different effects of zinc and strontium. J. Inorg. Biochem. 1997;66:259 265
- Bigi A, Panzavolta S, Rubini K. Relationship between triple helix content and mechanical properties of gelatin films. Biomaterials 2004;25:5675–5680
- Boanini E, Gazzano M, Nervi C, Chierotti MR, Rubini K, Gobetto R, Bigi A. Strontium and zinc substitution in β-tricalcium phosphate: an X-ray diffraction, solid state NMR and ATR-FTIR study. J. Funct. Biomater. 2019;10:20
- Boanini E, Gazzano M, Rubini K, Mazzeo PP, Bigi A. Structural interplay between strontium and calcium in α-CaHPO4 and β-SrHPO4. Ceram. Int. 2021;47:24412–24420
- Boanini E, Rubini K, Panzavolta S, Bigi, A. Chemico-physical characterization of gelatin films modified with oxidized alginate. Acta Biomater. 2010;6:383–388
- Boanini E, Silingardi F, Gazzano M, Bigi A. Synthesis and hydrolysis of brushite (DCPD): the role of ionic substitution. Cryst. Growth Des. 2021;21:1689–1697
- Boanini E, Torricelli P, Cassani MC, Rubini K, Fini M, Pagani S, Bigi A. Platinum nanoparticles supported on functionalized hydroxyapatite: anti-oxidant properties and bone cells response. Ceram. Int. 2020;46:19574–19582
- Bonnelye E, Chabadel A, Saltel, F, Jurdic P. Dual effect of strontium ranelate: stimulation of osteoblast differentiation and inhibition of osteoclast formation and resorption in vitro. Bone 2008;42:129–138
- Borghetti GS, Carini JP, Honorato SB, Ayala AP, Moreira JCF, Bassani VL. Physicochemical properties and thermal stability of quercetin hydrates in the solid state. Thermochim. Acta 2012;539:109–114
- Boudjada A, Masse R, Guttel JC. Structure cristalline de l'orthophosphate monoacide de strontium: *$SrHPO_4$* α: forme triclinique. Acta Crystallogr. B 1978;34: 2692–2695

- Catti M, Ferraris G, Filhol A. Hydrogen bonding in the crystalline state. $CaHPO_4$ (Monetite), P-1 or P1? A novel neutron diffraction study. Acta Cryst. 1977;B33:1223-1229
- Cirillo M, Martelli G, Boanini E, Rubini K, Di Filippo M, Torricelli P, Pagani S, Fini M, Bigi A, Giacomini D. Strontium substituted hydroxyapatite with β-lactam integrin agonists to enhance mesenchymal cells adhesion and to promote bone regeneration. Colloids Surf. B: Biointerfaces 2021;200:111580
- Dai Y, Terskikh V, Brinmkmann A, Wu G. Solid-State ^{1}H, ^{13}C, and ^{17}O NMR characterization of the two uncommon polymorphs of curcumin. Cryst. Growth Des. 2020;20,:7484–7491
- Dasari S, Tchounwou PB. Cisplatin in cancer therapy: molecular mechanisms of action. Eur. J. Pharmacol. 2014;740:364–378
- Deacon GB, Phillips RJ. Relationships between the carbon-oxygen stretching frequencies of carboxylato complexes and the type of carboxylate coordination. Coord. Chem. Rev. 1980;33:227–250
- Dorozhkin SV. Calcium orthophosphates ($CaPO_4$): Occurrence and properties. Prog. Biomater. 2016;5:9–70
- Elliott JC. Structure and chemistry of the apatites and other calcium orthophosphates. Elsevier: Amsterdam, 1994
- Enoki Y, Sato T, Tanaka S, Iwata T, Usui M, Takeda S, Kokabu S, Matsumoto M, Okubo M, Nakashima K, Yamato M, Okano T, Fukuda T, Chida D, Imai Y, Yasuda H, Nishihara T, Akita M, Oda H, Okazaki Y, Suda T, Yoda T. Netrin-4 derived from murine vascular endothelial cells inhibits osteoclast differentiation in vitro and prevents bone loss in vivo. FEBS Lett. 2014;588:2262–2269.
- Finch A, Ledward DA. Shrinkage of collagen fibers: A differential scanning calorimetric study. Biochim. Biophys. Acta 1972;278:433–439
- Forte L, Torricelli P, Boanini E, Gazzano M, Rubini K, Fini M, Bigi A. Antioxidant and bone repair properties of quercetin-functionalized hydroxyapatite: An in vitro osteoblast–osteoclast–endothelial cell co-culture study. Acta Biomater. 2016;32:298–308
- Forte L, Torricelli P, Boanini E, Rubini K, Fini M, Bigi A. Quercetin and alendronate multi-functionalized materials as tools to hinder oxidative stress damage. J. Biomed. Mater. Res. Part A 2017;105A:3293–3303
- Fowler BO, Markovic M, Brown WE. Octacalcium phosphate. 3. Infrared and raman vibrational spectra. Chem. Mater. 1993;5:1417–1423
- Galletti P, Soldati R, Pori M, Durso M, Tolomelli A, Gentilucci L, Dattoli SD, Baiula M, Spampinato S, Giacomini D. Targeting integrins αvβ3 and α5β1 with new β-lactam derivatives. Eur. J. Med. Chem. 2014;83:284–293
- Gomes S, Nedelec JM, Jallot E, Sheptyakov D, Renaudin G. Unexpected mechanism of Zn^{2+} insertion in calcium phosphate bioceramics. Chem. Mater. 2011;23:3072–3085.

- Gomez-Guillen MC, Gimenez B, Lopez-Caballero ME, Montero MP. Functional and bioactive properties of collagen and gelatin from alternative sources: A review. Food Hydrocoll. 2011;25:1813–1827
- Grigg AT, Mee M, Mallinson PM, Fong S.K, Gan Z, Dupree R, Holland D. Cation substitution in β-tricalcium phosphate investigated using multi-nuclear, solid-state NMR. J. Solid. State Chem. 2014;212:227–236
- Hewlings SJ, Kalman DS. Curcumin: A review of its' effects on human health. Foods 2017;6:92
- Hosaka H, Haruki R, Yamada K, Böttcher C, Komatsu T. Hemoglobin–albumin cluster incorporating a Pt nanoparticle: artificial O2 carrier with antioxidant activities. PloS One 2014;9:e1105419
- Jillavenkatesa A, Condrate RA. The infrared and Raman spectra of α- and β-tricalcium phosphate ($Ca_3(PO_4)_2$). Spectrosc. Lett. 1998;31:1619–1634
- Kannan S, Goetz-Neunhoeffer F, Neubauer J, Pina S, Torres PMC, Ferreira JMF. Synthesis and structural characterization of strontium and magnesium co-substituted β-tricalcium phosphate. Acta Biomater. 2010;6:571–576
- Kozlov PV, Burdigina GI. The structure and properties of solid gelatin and the principles of their modification. Polymer 1983;24:651–666
- Landin M, Rowe RC, York P. Structural changes during the dehydration of dicalcium phosphate dihydrate. Eur. J. Pharm. Sci. 1994;2:245–252
- Lu Z, Chu W, Tan R, Tang S, Xu F, Song W, Zhao J. Facile synthesis of β-$SrHPO_4$ with wide applications in the effective removal of Pb^{2+} and methyl blue. J. Chem. Eng. Data 2017;62: 3501–3511
- Martelli G, Bloise N, Merlettini A, Bruni G, Visai L, Focarete ML, Giacomini D. Combining biologically active β-lactams integrin agonists with poly(l-lactic acid) nanofibers: enhancement of human mesenchymal stem cell adhesion. Biomacromolecules 2020;21:1157–1170
- Mohammadi H, Abedi A, Akbarzadeh A, Mokhtari MJ, Shahmabadi HE, Mehrabi MR, Javadian S, Chiani M. Evaluation of synthesized platinum nanoparticles on the MCF-7 and HepG-2 cancer cell lines. Int. Nano Lett. 2013;3:28
- Mondal S, Ghosh S, Moulik SP. Stability of curcumin in different solvent and solution media: UV–visible and steady-state/ fluorescence spectral study. J. Photochem. Photobiol. B Biol. 2016;158:212–218
- Nandha Kumar P, Boovarasan M, Singh RK, Kannan S. Synthesis, structural analysis and fabrication of coatings of the Cu^{2+} and Sr^{2+} co-substitutions in β-$Ca_3(PO_4)_2$. RSC Adv. 2013;3:22469–22479
- Okuyama K. Revisiting the molecular structure of collagen. Connective Tissue Res. 2008;49:299–310

- Patel AR, Heussen PCM, Hazekamp J, Drost E, Velikov KP. Quercetin loaded biopolymeric colloidal particles prepared by simultaneous precipitation of quercetin with hydrophobic protein in aqueous medium. Food Chem. 2012;133:423–429
- Priyadarsini KI. The chemistry of curcumin: From extraction to therapeutic agent. Molecules 2014;19:20091–20112
- Puja P, Kumar P. A perspective on biogenic synthesis of platinum nanoparticles and their biomedical applications. Spectrochim. Acta, Part A 2019;211:94–99
- Quillard S, Paris M, Deniard P, Gildenhaar R, Berger G, Obadia L, Bouler JM. Structural and spectroscopic characterization of a series of potassium and/or sodium-substituted β-tricalcium phosphate. Acta Biomater. 2011;7:1844–1852
- Rivas BL, Pooley SA, Pereira ED, Cid R, Luna M, Jara MA, Geckeler KE. Water-soluble amine and imine polymers with the ability to bind metal ions in conjunction with membrane filtration. J. Appl. Polym. Sci. 2005;96:222–231
- Roming M, Feldmann C. Selective synthesis of α- and β-$SrHPO_4$ nanoparticles. J. Mater. Sci. 2008;43:5504–5507
- Roy M, Fielding GA, Bandyopadhyay A, Bose S. Effects of zinc and strontium substitution in tricalcium phosphate on osteoclast differentiation and resorption. Biomater. Sci. 2013;1: 74–82
- Rubini K, Boanini E, Bigi A. Role of aspartic and polyaspartic acid on the synthesis and hydrolysis of brushite. J. Funct. Biomater. 2019;10:11
- Rubini K, Boanini E, Menichetti A, Bonvicini F, Gentilomi GA, Montalti M, Bigi A. Quercetin loaded gelatin films with modulated release and tailored anti-oxidant, mechanical and swelling properties. Food Hydrocoll. 2020;109:106089
- Rubini K, Boanini E, Parmeggiani S, Bigi A. Curcumin-functionalized gelatin films: antioxidant materials with modulated physico-chemical properties. Polymers 2021;13:1824
- Salamanna F, Giavaresi G, Parrilli A, Torricelli P, Boanini E, Bigi A, Fini M. Antiresorptive properties of strontium substituted and alendronate functionalized hydroxyapatite nanocrystals in an ovariectomized rat spinal arthrodesis model. Mater. Sci. Eng. C-Mater. Biol. Appl. 2019;95:355–362
- Shamrai VF, Karpikhin AE, Fedotov AY, Sirotinkin VP, Barinov SM, Komlev VS. Structural changes during the hydrolysis of dicalcium phosphate dihydrate to octacalcium phosphate and hydroxyapatite. Inorg. Mater. 2015;51:355–361
- Shepherd DV, Kauppinen K, Brooks RA, Best SM. An in vitro study into the effect of zinc substituted hydroxyapatite on osteoclast number and activity. J. Biomed. Mater. Res. Part A 2014;102:4136–4141
- Sikiric M, Babic-Ivancic V, Milat O, Sarig S, Füredi-Milhofer H. Factors influencing additive interactions with calcium hydrogenphosphate dihydrate crystals. Langmuir 2000;16:9261–9266

- Snyder LR. Classification of the solvent properties of common liquids. J. Chromatogr. 1974;92: 223–230
- Strauss G, Gibson SM. Plant phenolics as cross-linkers of gelatin gels and gelatin based coacervates for use as food ingredients. Food Hydrocoll. 2004;18:81–89
- Sutha S, Karunakaran G, Rajendran V. Enhancement of antimicrobial and long-term biostability of the zinc-incorporated hydroxyapatite coated 316 L stainless steel implant for biomedical application. Ceram. Int. 2013;39:5205–5212.
- Tas AC, Bhaduri SB. Chemical processing of $CaHPO_4{\cdot}2H_2O$: Its conversion to hydroxyapatite. J. Am. Ceram. Soc. 2004;87:2195–2200
- Tortet L, Gavarri JR, Nihoul G, Dianoux AJ. Study of protonic mobility in $CaHPO_4{\cdot}2H_2O$ (brushite) and $CaHPO_4$ (monetite) by infrared spectroscopy and neutron scattering. J. Solid State Chem. 1997;132:6–16
- Wang W, Sun C, Mao L, Ma P, Liu F, Yang J, Gao Y. The biological activities, chemical stability, metabolism and delivery systems of quercetin: A review. Trends Food Sci. Technol. 2016;56:21–38.
- Wanninger S, Lorenz V, Subhanb A, Edelmann FT. Metal complexes of curcumin—Synthetic strategies, structures and medicinal applications. Chem. Soc. Rev. 2015;44:4986–5002
- Wei Q, Pohl TLM, Seckinger A, Spatz JP, Cavalcanti-Adam EA. Regulation of integrin and growth factor signaling in biomaterials for osteodifferentiation. Beilstein J. Org. Chem. 2015;11:773–783
- Xu J, Butler IS, Gilson DFR. FT-Raman and high-pressure infrared spectroscopic studies of $CaHPO_4{\cdot}2H_2O$ and $CaHPO_4$. Spectrochim. Acta 1999;A55:2801–2809
- Yashima M, Sakai A, Kamiyama T, Hoshikawa A. Crystal structure analysis of β-tricalcium phosphate $Ca_3(PO_4)_2$ by neutron powder diffraction. J. Solid State Chem. 2003;175:272–277
- Young RA. The Rietveld method. Oxford University Press: Oxford, UK, 1993
- Zhang L, Laug L, Műnchgesang W, Pippel E, Gősele U, Brandsch M, Knez M. Reducing stress on cells with apoferritin-encapsulated platinum nanoparticles. Nano Lett. 2010;10:219–223
- Zhang ZL, Chen XR, Bian S, Huang J, Zhang TL, Wang K. Identification of dicalcium phosphate dihydrate deposited during osteoblast mineralization in vitro. J. Inorg. Biochem. 2014;131:109–114

Chapter 5
CONCLUSIONS

During this PhD thesis a variety of functionalized and multi-functionalized materials were developed and characterized. The substrates submitted to functionalization include several calcium phosphates of biological interest, namely hydroxyapatite, brushite, monetite and β-tricalcium phosphate, as well as gelatin films. Polyelectrolytes, amino acids and polyaminoacids, metallic nanoparticles and ions, as well as polyphenols, were tested as functionalizing agents.

The results indicate that the properties of the selected substrates can be enriched and modulated through functionalization.

In particular, the role of strontium on the structure and morphology of monetite and β-tricalcium phosphate was clarified. Strontium can substitute for calcium in the structure of DCPA in the whole range of composition up to 100 at% Sr, which yield α-$SrHPO_4$, isomorphous with monetite. The expansion of the cell parameters, in agreement with the bigger ionic radius of strontium than calcium, vary linearly with composition. Solid solutions of intermediate composition exhibit a reduction of the length of the perfect crystalline domains and of the sharpness of the infrared absorption bands, suggesting a reduction of crystallinity in comparison to those of the two end members. The big crystals of monetite display a layered morphology, which vary with composition so that α-$SrHPO_4$ is constituted by much smaller rod-like crystals. Similar structural modifications were observed for the samples prepared through thermal treatment of Sr-substituted DCPD, although this synthesis method allowed to reach a degree of strontium incorporation into monetite structure limited to about 38 at%, because the structure of brushite cannot host greater strontium contents. In this case, the products of thermal treatment maintained the characteristic morphology of the DCPD samples.

This study provided also new structural information on β-$SrHAPO_4$, which was obtained when the direct synthesis was carried out at relatively low temperature. The thin flaky-like crystals of β-$SrHAPO_4$ are aggregated in clusters and exhibit a monoclinic structure (space group $P2_1/c$), where strontium occupies two independent sites. Calcium can enter into this structure and substitute strontium just up to about 20 at%, before provoking the precipitation of secondary phases.

Strontium was shown to have an important influence also on the structure of β-TCP, with a behavior quite different from that exhibited by the smaller zinc ion. In fact, Zn can be incorporated into β-TCP structure just up to about 10 at% and it occupies preferentially the octahedral Ca(5) site, whereas it does not show any preference for the Ca(4) site. The main consequences of Zn substitution are a reduction of the dimensions of the unit cell, a shift of the solid-state 31P NMR resonances of the two phosphate close to Ca(5), namely P(2) and P(3), and a general disorder of β-TCP structure as shown by the broadening of the ATR-FTIR bands.

At variance, Sr can substitute for Ca in the structure of β-TCP up to about 80 at%, but it never occupies the relatively small Ca(5) site. In contrast, it exhibits a clear preference for Ca(4), where at the highest concentration its presence causes a slight modification the β-TCP structure into the more symmetric β'-TCP.

Strontium-substituted hydroxyapatite was utilized to prepare multifunctional materials through loading β-lactam integrin antagonists. The amount of β-lactam compounds onto Sr-hydroxyapatite could be modulated through variation in the polarity of the loading solution up to about 24 wt% and 8.4 wt% for compounds **1** and **2** (please see Chapter 2, par.1.4), respectively. Studies on the release of β-lactams from the functionalized SrHA in aqueous medium showed that after an initial burst, the release of both compounds reached a steady state, maintaining a significant local concentration over time.

Hydroxyapatite was successfully utilized also as support for Pt nanoparticles (PtNPs). To this aim, HA nanocrystals were functionalized with PEI, which was shown to enhance PtNPs loading thanks to the polyelectrolyte interaction with the metallic ion, Pt(II). Chemical reduction of Pt(II) adsorbed on HAPEI provided multifunctionalized apatite loaded with Pt nanoparticles. Moreover, increase of PtNPs dimensions, from 1 nm to 20-30 nm was obtained through thermal treatment of the multifunctionalized materials. These composites showed similar values of H_2O_2 decomposing activity independently from the dimensions of the metallic nanoparticles, confirming their good anti-oxidant properties.

The studies on functionalized calcium phosphates performed during this PhD thesis included also the interaction of acidic amino and polyaminoacids, namely ASP and PASP, with brushite. The results indicate that PASP inhibits the crystallization of DCPD, which is completely hindered when the concentration of the polyelectrolyte exceeds 1 mM in monomeric units. Functionalization occurs up to about 2.3 wt% and

provokes aggregation of the DCPD crystals, most likely through interaction of the polyaminoacid with the (0k0) faces. On the contrary, ASP is not adsorbed at all on DCPD and the products of syntheses when submitted to hydrolysis in physiological solution exhibit the same extent of conversion into the more stable phases, OCP and/or HA, as that observed for pure DCPD. At variance, the results showed that PASP adsorbed on DCPD crystals provokes a delay of the conversion reaction. When dissolved in the hydrolysis solution, both ASP and PASP delay the phase transition, but PASP exerts a stronger inhibition than ASP.

A further part of activity was devoted to the functionalization and characterization of gelatin films. Quercetin, a flavonoid widely diffused in fruit and vegetables, and curcumin, a natural polyphenol extracted from the rhizomatous plant *Curcuma Longa*, were chosen for their good pharmacological qualities, such as anti-oxidant and anti-inflammatory properties. Quercetin and curcumin were loaded on gelatin films with the aim to develop materials with tailored anti-oxidant, mechanical and stability properties.

Loading of quercetin was performed using two different solvents, H_2O/EtOH and DMSO. The amount of flavonoid adsorbed on the films reached values up to about 3.8 and 1.8 wt% in DMSO and EtOH films, respectively. DMSO prevents the partial regain of collagen triple helix structure during gelling of gelatin sols and results in remarkable extensibility of the films. At variance, the triple helix structure is present in EtOH films, which exhibit a reduction of swelling and an increase of the mechanical parameters on increasing quercetin content. Moreover, the observed reduction of denaturation enthalpy indicate the presence of chemical interactions between gelatin and the flavonoid, which can justify their lower quercetin release in PBS in comparison to DMSO films. However, the flavonoid release is sustained for both series of films and occurs through anchorage to gelatin nanoparticles.

Also in the case of curcumin functionalized films, the release of the polyphenol is sustained both in physiological solution and, even more, in PBS. In this case, the amount of curcumin loaded on gelatin films reach a maximum value of 1.2 wt%, causing a reduction in the swelling degree, water solubility, and extensibility of the films. Further significant reduction of swelling, water solubility and curcumin release, increase of thermal stability, as well as variations of mechanical parameters were observed after crosslinking with glutaraldehyde. Both quercetin- and curcumin-

functionalized films exhibit RSA levels comparable to those of the pure polyphenols, in agreement with remarkable anti-oxidant properties.

The materials developed during this PhD thesis display a variety of properties which can be usefully exploited in several application. In particular, the biological tests performed on some of these materials are very encouraging. Functionalization of hydroxyapatite nanocrystals with Pt nanoparticles provided materials able to stimulate osteoblast alkaline phosphates activity and collagen production. Moreover, they were found to display anti-oxidant properties that contribute to counteract oxidative stress damage and cell senescence [Boanini E, Torricelli P, Cassani MC, Rubini K, Fini M, Pagani S, Bigi A. Platinum nanoparticles supported on functionalized hydroxyapatite: anti-oxidant properties and bone cells response. Ceram. Int. 2020;46:19574–19582].

SrHA loaded with β-lactams were demonstrated to enhance adhesion and viability of human mesenchymal stem cells. Furthermore, the inhibiting influence of Sr-hydroxyapatite on osteoclast viability and activity was enhanced by the presence of the β-lactams, whereas Sr contributed to support osteogenic differentiation of mesenchymal cells, suggesting a potential local employment of these multi-functionalized materials to promote osteointegration and counteract abnormal bone loss [Cirillo M, Martelli G, Boanini E, Rubini K, Di Filippo M, Torricelli P, Pagani S, Fini M, Bigi A, Giacomini D. Strontium substituted hydroxyapatite with β-lactam integrin agonists to enhance mesenchymal cells adhesion and to promote bone regeneration. Colloids Surf. B: Biointerfaces 2021;200:111580].

Index page

Summary 1

Chapter 1 - INTRODUCTION

1. Biomaterials 3

2. Calcium Phosphates 5

2.1 Hydroxyapatite 8

2.2 Monetite 11

2.3 Brushite 12

2.4 Beta-Tricalcium Phosphate 13

3. Gelatin 15

4. Functionalization 17

4.1 Metals 17

4.1.1 Platinum 17

4.1.2 Strontium 18

4.1.3 Zinc 19

4.2 Organic molecules 20

4.2.1 β-Lactams 20

4.2.2 Aspartic and poly-aspartic acid 20

4.2.3 Polyphenols 21

INTRODUCTION – References 25

Chapter 2 -EXPERIMENTAL SECTION – *Preparation of Materials*

1. Hydroxyapatite (HA) 30

1.1 Hydroxyapatite – Polyetyhlenimine (HAPEI) 30

1.2 Hydroxyapatite - Platinum 30

1.3 Strontium Hydroxyapatite (SrHA) 31

1.4 Strontium Hydroxyapatite – β-Lactams 31

2. Brushite (DCPD) 33

2.1 Brushite - polyaspartate (DCPD-PASP) 33

2.2 Brushite –aspartic acid (DCPD-ASP) 33

2.3 Hydrolysis of DCPD – role of ASP and PASP 33

2.4 Strontium Brushite (SrDCPD)	34
3. Monetite (DCPA)	34
3.1 Strontium Monetite (SrDCPA)	34
3.2 β-$SrHPO_4$	35
4. β-TriCalcium Phosphate (β-TCP)	35
4.1 Strontium β-TCP	35
4.2 Zinc β-TCP	36
5. Gelatin films	36
5.1 Gelatin-quercetin films	36
5.2 Gelatin-curcumin films	37
EXPERIMENTAL SECTION- *Preparation of Materials* -References	38

Chapter 3-EXPERIMENTAL SECTION–*Characterization of Materials*

1. Powder X-ray diffraction	39
1.1 Rietveld refinement	39
1.2 Scherrer analysis	40
1.3 Structure solution	41
2. Fourier Transform Infra-Red Spectroscopy	41
3. Solid state Nuclear Magnetic Resonance	41
4. Elemental Analyses	42
4.1 Atomic absorption spectroscopy (AAS)	42
4.2 Ion chromatography	42
4.3 Analysis of light elements	42
5. Thermal Analyses	42
5.1 Thermogravimetric Analysis	42
5.2 Differentaial Scanning Calorimetry	43
6. Electron Microscopy	43
6.1 Scanning electron microscopy	43
6.2 Transmission electron microscopy	43
6.3 Fluorescence microscopy	43
7. Surface Area Analysis	43
8. Zeta Potential Measurement	44

9. Uv-Vis Spectroscopy	44
9.1 Release of β-Lactams	44
9.2 Quercetin content and release	44
9.3 Curcumin content and release	45
10. Swelling tests	45
11. Water solubility	45
12. Static contact angle	46
13. Mechanical tests	46
14. Assays for scavenging activities	46
14.1 Radical scavenging activity	46
14.2 Hydrogen peroxide scavenging activity	47
EXPERIMENTAL SECTION- *Characterization of Materials* - References	48

Chapter 4 - RESULTS AND DISCUSSION

1. Functionalization of calcium phosphates	49
1.1 Hydroxyapatite crystals enriched with platinum nanoparticles	49
1.2 Strontium substituted hydroxyapatite functionalized with β-lactams	55
1.3 Functionalization of brushite with aspartic and poly-aspartic acids	62
1.3.1 Synthesis of DCPD-ASP	63
1.3.2 Synthesis of DCPD-PASP	65
1.3.3 Hydrolisis	72
1.4 Ionic substitution of strontium in the structure of monetite	76
1.4.1 Direct synthesis	76
1.4.2 Heat treatment	82
1.4.3 Calcium substitution in the structure of β-$SrHPO_4$	86
1.4.4 Structure of β-$SrHPO_4$	88
1.5 Ionic substitution of strontium and zinc in the structure of β-TCP	91
1.5.1 Strontium substitution	91
1.5.2 Zinc substitution	97
2. Functionalization of gelatin films	102
2.1 Gelatin – quercetin films	102
2.2 Gelatin – curcumin films	114

RESULTS AND DISCUSSION – References 127

Chapter 5 - CONCLUSIONS 132